Characteristics of warm season supercell thunderstorms over the Gauteng and Mpumalanga Provinces of South Africa

by

Christina Gabriele Liesker

Submitted in partial fulfilment of the requirement for the degree

Master of Science (Meteorology)

In the Faculty of Natural & Agricultural Sciences

University of Pretoria

Pretoria

(November 2021)

DECLARATION

I, Christina Gabriele Liesker declare that the dissertation, which I hereby submit for the degree Master of Science (Meteorology) at the University of Pretoria, is my own work and has not previously been submitted by me for a degree at this or any other tertiary institution.

SIGNATURE: 

DATE: 4 February 2022

Characteristics of warm season supercell thunderstorms over the Gauteng and Mpumalanga Provinces of South Africa

Student: Christina Gabriele Liesker

Supervisor: Prof. Liesl L. Dyson

Co-supervisor: Erik H. Becker

Department: Geography, Geoinformatics and Meteorology

Faculty: Natural & Agricultural Sciences

University: University of Pretoria

Degree: Master of Science (Meteorology)

ABSTRACT

A supercell thunderstorm, notorious for producing large hail, damaging winds, tornadoes, and flooding, often results in damage to property, injuries, and loss of life. Supercells were previously considered rare in South Africa, but in more recent years, evidence has shown this not to be the case. With the installation of the South African Weather Service Doppler radar network in 2010, several cases have since been detected. However, no radar-derived database exists and research on supercells, including their occurrence and characteristics, is limited over South Africa. The aim of this research is to investigate the characteristics of supercells over the Gauteng and Mpumalanga provinces of South Africa during the warm seasons (September to February) of 2010 to 2020. To achieve this a radar-derived database was created, using all available radar data from the Irene and Ermelo radar, with as many supercells identified as possible. These supercells were analysed to investigate their temporal, spatial, track and lifespan characteristics. A database comprising 115 left-moving and 6 right-moving events over 67 event days was established. On a given event day an average of 2 supercells were found to occur with their activity peaking in the afternoon between 13:00 and 14:00 UTC. On average 13 supercell events and 7 event days (containing at least 1 supercell) occurred per season and their frequency peaked between October and November. The peak in the monthly distribution occurred earlier over Gauteng in October and November, but over Mpumalanga the peak

was later during December. Supercell activity occurred over the southern Highveld in September, spreading northwards by October and then to the south-east, while decreasing in the west, in December. The spatial distribution (initiation, track, and demise) showed hotspots in activity in places over southern Gauteng as well as the south-eastern parts of Mpumalanga. Supercells were predominantly short-lived (lasting ≤ 2 hours), with only 12 moderate-lived left-moving events (lasting > 2 hours but < 4 hours). On average the left-moving events lasted 1 hour 12 minutes, tracking an average distance of 49 km, while on average right-moving events lasted 49 minutes and tracked 27 km. The left-moving supercells had an average track from the south-west to north-east, however, their track shifted from west south-westerly earlier in the season to southerly in January. All right-moving supercell events had a track from the north-west to south-east. The short-term radar-based climatology of supercell characteristics that were identified in this research, will allow for a better understanding and thus potentially improving forecasting, nowcasting and warning for these thunderstorms over the Gauteng and Mpumalanga provinces of South Africa. A further investigation into the environment and topography over the area is required, to fully understand why these characteristics were observed. The radar-derived supercell database is a first for South Africa and thus provides a foundation on which numerous other studies can be conducted.

ACKNOWLEDGEMENTS

I would like to acknowledge and thank the following people and organisations who greatly contributed to this research

- Professor Liesl Dyson, my supervisor, for all her guidance, support, expert advice, and patience. Her constant encouragement helped me to stay focused and remain positive throughout this process. I really appreciate the time she put in to assist me and of course all the cups of coffee.
- Erik Becker, my co-supervisor, for all his inputs, expert advice, and support. I appreciate all the time he set aside to assist me and for constantly challenging me.
- Kyle Liesker, my husband, for his constant support, encouragement, and countless conversation about supercells. I also really appreciate the time he took to read through this dissertation, help with GIS and excel related questions and most importantly for spending endless quality time with our son, Finn (who was born in the first year of this degree) so that I could work on my dissertation.
- My family for their constant support and assistance.
- The South African Weather Service for providing the radar data, especially Morne Gijben for his friendly assistance and quick response.
- Dr Michael Dixon (from the National Center for Atmospheric Research), for helping to identify the error and modifying the necessary program within the LROSE software, that resulted in the conversion issues due to the South African Weather Service's radar setup.
- James Ladue (from the National Oceanic and Atmospheric Administration), for providing his assistance, knowledge, and input with the identification of the supercell events, especially the more challenging events.
- Lourens Snyman (from the Department of Geography, Geoinformatics and Meteorology), for helping to create the Kernel Density Estimation function map and for all the other assistance and advice regarding the maps created in QGIS.
- The South African Weather Service librarians, Karin Oxley and Anastasia Demertzis, for their assistances with regards to the library resources.
- The examiners for their valuable comments and contribution to this dissertation.

TABLE OF CONTENTS

LIST OF FIGURES

LIST OF TABLES

LIST OF SYMBOLS AND ABBREVIATIONS

°	Degree
%	Percentage
AGL	Above Ground Level
AMSL	Above Mean Sea Level
BWER	Bound Weak Echo Region
CAPE	Convective Available Potential Energy
cm	Centimetre
dBZ	Decibel relative to reflectivity
FFD	Forward Flank Downdraft
GHz	Gigahertz
GIS	Geographic Information System
HP	High Precipitation
Hz	Hertz
Jkg^{-1}	Joules per kilogram
km	Kilometres
kmh^{-1}	Kilometres per hour
kts	Knots
LEWP	Line Echo Wave Pattern
LP	Low Precipitation
LROSE	Lidar Radar Open Software Environment

ms^{-1}	Metres per second
mm	Millimetres
QGIS	Quantum Geographic Information System
RFD	Rear Flank Downdraft
SAST	South African Standard Time
SAWS	South African Weather Service
SI	Showalter Index
TITAN	Thunderstorm Identification, Tracking, Analysis and Nowcasting
µs	Microsecond
USA	United States of America
USGS	United States Geological Survey
UTC	Universal Time Coordinated
WER	Weak Echo Region
WMO	World Meteorological Organization
yr	Year

Chapter 1: Introduction

1.1 Background

Supercell thunderstorms are considered the most severe type of thunderstorm, known to be able to produce large hail, damaging winds, long-lived tornadoes and in some cases flooding (Burgess and Lemon, 1990; Moller et al., 1994; Ray, 1990; Weisman and Klemp, 1986). Supercells occur around the world such as in the United States of America (USA), Europe, Australia and Brazil (e.g., Allen, 2012; Antonescu et al., 2010; Bunkers et al., 2006a; Christodoulou and Sioutas, 2017; Feldmann et al., 2021; Held et al., 2010; Hocker and Basara, 2008). However, such thunderstorms were considered to be extremely rare in South Africa in the past (Admirat et al., 1985; Carte, 1979, 1981; de Coning et al., 2000). According to Admirat et al. (1985), very few supercells occurred in a 20-year period between 1962 and 1981 over the Highveld of South Africa (north-eastern interior, see section 3.2). The first supercell was identified on radar over this area in 1978, 7 years after the radar was installed (Carte, 1981). The definition for supercells and the identification of supercells using radar data (including Doppler velocities) was still evolving and being enhanced in the USA and the Northern Hemisphere at the time (Moller et al., 1994). Emphasis was placed on the "steady state" of a supercell by various authors in South Africa (e.g., Carte, 1979, 1981; de Coning et al., 2000), however, a few years later this was found internationally not to necessarily be the case (e.g. Doswell III and Burgess, 1993; Lemon, 1977; Moller et al., 1994) which is discussed in more detail in section 2.3).

More recently, evidence has shown that in South Africa supercells are in fact more frequent than previously believed. According to Visser (2001), the storm season of 1998-1999, where a high frequency of tornadoes occurred, confirmed that supercells thunderstorms were in fact more common. Rae (2014) provided 15 event dates, that were either visually observed or identified on radar between 1985 and 2011. Up until now this was the only attempt at a database of supercells within South Africa. With the installation of the Doppler radar network in 2010 by the South African Weather Service (SAWS) (Becker, 2014), numerous cases of supercells have been confirmed, but no formal database of all these events exists, nor have any other events, that may have occurred, been documented.

Over the Gauteng and Mpumalanga provinces of South Africa (location provided in section 3.2), various supercell events, which have also resulted in severe weather, have been identified between 2010 and 2020 (Table 1-1), either through scientific case studies or reports and media releases issued by the SAWS (Kruger et al., 2018; Lekoloane et al., 2021; Modika, 2020; Powell and Burger, 2014; Rae,

2014; SAWS, 2011, 2013, 2017; Sebego and Rae, 2017). Table 1-1 does not include all confirmed supercell events but only those that have been confirmed through published reports. Severe weather associated with these supercells (or on the day supercells occurred), resulted in damage to property, injury and in some cases loss of life over Gauteng and Mpumalanga (Table 1-1). The economic impacts have also been significant, for example on 11 and 28 November 2013 large hail resulted in insurance claims amounting to over 2 billion in South African Rands (Dyson et al., 2021). It is thus vital to accurately forecast and warn for supercell thunderstorms.

Table 1-1: Published reports of severe weather that occurred either due to a confirmed supercell thunderstorm or on a day where supercell thunderstorms were reported across the Gauteng and Mpumalanga provinces between 2010 and 2020. This is not an exhausted list of all supercell events, that resulted in damaging weather conditions, and only consists of those confirmed events that were formally published either through a case study or a SAWS issued media release or report.

Date (dd/mm/yy)	Location	Severe weather reported on the day	Impact of severe weather	Source
11/11/13	Benoni and Mamelodi, Gauteng	Large hail (golf ball size)	Damage to buildings and cars	Dyson et al., 2021 SAWS, 2013
28/11/13	Across Gauteng	Large hail, flooding, and damaging winds	Extensive damage to property (houses, cars, etc.), damage to infrastructure, at least 3 deaths	Powell and Burger, 2014 Rae, 2014 SAWS, 2013
09/10/17	Southern Gauteng Delmas, Mpumalanga	2 Tornadoes, large hail (golf to tennis ball size)	Damage to property (roofs blown off), damage to infrastructure, at least 1 death, minor injuries	Sebego and Rae, 2017
11/12/17	Vaal Marina, Gauteng Standerton, Mpumalanga	2 Tornadoes and Hail	Damage to houses and displacement of over 1000 people	Lekoloane et al., 2021 Kruger et al., 2018 SAWS, 2017
30/12/17	Soweto and Westonaria, Gauteng	Tornado	Damage to houses	Kruger et al., 2018
03/01/20	Taaiboschspruit farm Panbult, Mpumalanga	Tornado	Damage to houses and 200 hectares of pine tree plantation	Modika, 2020

1.2 Motivation

A significant amount of research on supercells has been conducted around the world, with most originating from the USA. Research has included the behavioural characteristics within a specific region, such as their initiation, movement, evolution, lifespan, and demise (e.g., Antonescu et al., 2010; Bunkers et al., 2006a; Christodoulou and Sioutas, 2017; Hocker and Basara, 2008). This has led to a better understanding, thereby contributing to the forecast and nowcast of these thunderstorms (e.g., Bunkers et al., 2006b).

Research in South Africa has predominantly been focused on severe thunderstorms in general, with emphasis on hail, wind damage, lightning, and tornadoes (e.g., Admirat et al., 1985; Carte and Held, 1978; Dyson et al., 2021; Gijben, 2016; Goliger and Lunt, 1997; Goliger and Retief, 2007; Olivier, 1990). Only a few scientific case study based articles on supercells have been published over the years (e.g., Carte, 1981; de Coning et al., 2000; Lekoloane et al., 2021; Powell and Burger, 2014), while Rae (2014) focused on the environment associated with supercells, although based on a small sample of only 15 event days over Gauteng. No supercell database exists in South Africa and research on supercells has been very limited, with no studies on their spatial, temporal, track, or lifespan characteristics specific to the region.

The supercell characteristics studies undertaken in other regions (Antonescu et al., 2010; Bunkers et al., 2006a; Hocker and Basara, 2008), have provided motivation for the research done in this dissertation, especially considering the lack of research on supercells in general over South Africa. Supercell thunderstorms are known to result in damage to property, injuries, and loss of life (section 1.1), thus it is necessary to understand these thunderstorms better and to establish trends and characteristics specific to the region. This may assist in improving forecasts, nowcasts and more accurate warnings of these thunderstorms, thus allowing communities within their path to respond adequately.

1.3 Research problems

The lack of knowledge on supercells in South Africa has led to the following research questions for the Gauteng and Mpumalanga provinces:

1. What frequency do supercells have?
2. What temporal distribution (seasonal, monthly, diurnal etc.) do supercells exhibit?
3. Is there a pattern in the initiation and demise location for supercells?

4. What is the general lifespan of supercells?
5. Is there a trend in the way supercell thunderstorms move, with regards to the direction of movement, distance covered, speed, and spatial distribution?

1.4 Aims and objectives

The aim of this research is to investigate the characteristics of supercells over the Gauteng and Mpumalanga provinces of South Africa during the warm season (September to February) using the available radar data from 2010 to 2020. To achieve this aim, the following objectives were carried out:

1. Using both the Irene and Ermelo radar dataset identify as many supercell thunderstorms as possible, that have occurred within the radars range between 2010 and 2020 for the months of September until and including February.
2. Analyse the temporal distribution of all available supercells identified within the database.
3. Analyse the spatial initiation and demise characteristics of all available supercells identified within the database.
4. Analyse the lifespan of all available supercells identified within the database.
5. Analyse the track characteristics, which include distance, speed, direction, and spatial distribution of all available supercells identified within the database.

1.5 Delineations and limitations

Since radar data was only available over a 10-year period (2010 to 2020), the aim of this research was not to establish a comprehensive climatology of supercells and their characteristics, but rather investigate the short-term characteristics that may exist over the given study area based on as many supercells that could be identified during this period. As more data becomes available in the future, this research can form part of a larger climatological study.

The first objective within this study was to identify as many supercells as possible (not all). Despite some limitations due radar measurements, as many supercells were identified as possible over the 10-year period. Events that were missed may have been as a result radar data availability, resolution, scan strategy, and thunderstorm distance from the radar, while the subjective method used to identify supercell case studies may also have influenced the detection of events. Therefore, the characteristics identified in this research were based on the database identified in this research and may contain some biases. More detail of these limitations and impacts are discussed in section 6.1.1.

The aim of this research was also to identify some of the characteristics of supercells over Gauteng and Mpumalanga, and not to determine why they occur. Although meteorological and topographical influences are briefly discussed, more detailed studies are required to understand all the factors influencing the characteristics identified, which can then be used to improve the current forecasting practices.

1.6 Outline of the dissertation

Chapter 2 consists of the literature review. It includes a brief background on the thunderstorm and severe thunderstorm climatology over South Africa, as well as past radar-based research on thunderstorms and supercells. The remainder of the chapter focusses on the literature of supercells, including their definition, environment in which they develop, how they develop, lifecycle, structure, classification, and some characteristics and properties of supercells determined in other regions around the world.

Chapter 3 provides details of the data and methodology used to complete this research. The study period and study area are discussed, followed by details on the radar data used as well as the LROSE (Lidar Radar Open Software Environment) software and TITAN (Thunderstorm Identification, Tracking, Analysis and Nowcasting) algorithm, used to view and analyse the data. In the last two sections the methodology used to conduct this research is provided.

Chapter 4 is the first chapter that presents the results. This chapter specifically focusses on the database of supercells identified over Gauteng and Mpumalanga, addressing the events and event days as well as the seasonal and monthly distributions.

Chapter 5 is the second chapter that provides the results relating to supercell characteristics based on the database discussed in chapter 4. The analysis of the supercell initiation, demise, lifespan, and track is presented in this chapter.

Chapter 6 presents a discussion of the results. This chapter examines the results provided in chapter 4 and 5 and compares them to other relevant research, discusses their implications and provides the limitations. The chapter starts by discussing the supercell database, then seasonal and monthly characteristics, followed by the characteristics identified for the left-moving and right-moving supercells.

Chapter 7 is the final chapter, including the conclusions, the contributions of this research to science, a summary of the limitations and challenges and the recommendations for future research.

Chapter 2: Literature Review

This chapter starts with a brief overview of the thunderstorm and severe thunderstorm climatology of South Africa (section 2.1), with emphasis on the north-eastern interior, where the study area is located, followed by a short section discussing previous research on radar-derived thunderstorm characteristics as well as research on supercells in South Africa (section 2.2).

The subsequent sections focus on literature relating to supercell thunderstorms. This comprises their definition (section 2.3), the environment in which they develop (section 2.4), how they develop (section 2.5), their life cycle (section 2.6) and structural characteristics (section 2.7). The literature presented in these sections formed the basis on which the supercell identification method developed for this research was based, which is detailed in section 3.5.

The chapter ends with a short section on various research investigating the characteristics and properties of supercell thunderstorms in other regions around the world (section 2.8), from which the research in this dissertation was inspired. These studies provided the information for which the results presented in chapter 4 and 5 were based.

2.1 Thunderstorm and severe thunderstorm climatology of South Africa

The environment over the north-eastern parts of South Africa (Figure 2-1) is conducive for convection, making it a favoured region for thunderstorm development with more than 60 thunderstorm days per year (Gijben, 2012; Gill, 2009; Schulze and Maharaj, 2007; Taszarek et al., 2021). This region falls within the summer rainfall region (October to March) (Gijben, 2012; Gill, 2009; Schulze and Maharaj, 2007). According to Gijben (2012; 2016) the highest region of the lightning ground flash density (10 to 15 flashes km^{-2} yr^{-1}) includes most of the Highveld (north-eastern interior, see section 3.2) with even higher values (15 to 20 flashes km^{-2} yr^{-1}) over the eastern parts of the Highveld. Lightning predominantly occurs from September to February over this region, with the highest activity occurring between December and February (Gijben, 2016). This region also experiences most of its rainfall in December and January (Schulze and Maharaj, 2007). During the early summer months (October to December), weather systems influencing this region are predominantly extra-tropical, becoming tropical by the late summer season (January to March) (Dyson et al., 2015).

Severe thunderstorms, which may produce large hail, damaging winds, tornadoes, or flash flooding, are known to frequent South Africa's interior, especially during the spring and summer season, usually peaking early in the season (Admirat et al., 1985; Blamey et al., 2017; Carte and Held,

1978; Dyson et al., 2021; Goliger and Lunt, 1997; Held and Carte, 1979; Olivier, 1990). Severe thunderstorms develop in environments that favour deep moist convection, with strong low-level wind shear and high instabilities (Doswell III and Schultz, 2006; Johns and Doswell III, 1992; Moller et al., 1994; Ray, 1990). The mid-latitudes are a common region for severe thunderstorm and supercell development as a result of the adequate wind shear that exists in the region (Doswell III, 2001).

Goliger and Retief (2007) found that wind damage as a result of intense thunderstorms (for example downbursts and tornadoes) was most common over the eastern and north-eastern parts of South Africa and occurred between the months of September and February. Goliger and Lunt (1997), published a book on nearly 200 tornado events that were reported over South Africa between 1905 and 1997. They found that areas of the highest tornado events and thus areas of the highest probability of occurrence, included highly populated areas of Gauteng, as well as the south-western parts of Mpumalanga. They also found that tornadoes were observed to occur from spring until late summer or autumn.

Research on hailstorms over South Africa, includes hail climatological studies and comparative studies with other regions around the world. Many of these climatological studies were carried out over the former Transvaal region (north-eastern parts of South Africa, see section 3.2) using hail observations either from hailpads, hailcards or synoptic weather stations, while in other cases using radar observations, where for example the Probability of Hail by Waldvogel et al. (1979) was utilised (e.g., Admirat et al., 1985; Carte and Held, 1978; Olivier, 1990). These studies showed similar temporal characteristics of hailstorms over the north-eastern parts of the country with the hail season ranging between September to April, peaking around November. In addition, Admirat et al. (1985) found that most severe hailstorms occurred between November and December while a peak in hailstorm activity was found to occur around 15:00 UTC. In general hailstorms over Gauteng and Mpumalanga areas usually occurred between 10:00 UTC and 18:00 UTC, peaking between 15:00 and 16:00 UTC, with very few events during the morning hours (Olivier, 1990).

More recently, Dyson et al. (2021), did a climatological hail study using the HAILCAST model which was run using ERA-Interim reanalysis data. Their results were very much in agreement with these observational studies. Specifically, over the north-eastern parts of the country, the hail day frequency was also found to peak in November and in general the Highveld had a high frequency of events. Higher areas of hail day frequencies included the southern parts of Gauteng and south-western parts of Mpumalanga, decreasing towards the north and east, which is in agreement with the

observational distribution determined by Olivier (1990) for the same region. In addition, both studies observed a westward geographical shift in the peak in hail day frequency as the season progressed.

Due to a lack of observations globally, various studies have used meteorological parameters from reanalysis data to determine climatological frequency and variability of severe thunderstorms (e.g., Blamey et al., 2017; Brooks, 2009; Brooks et al., 2003; Taszarek et al., 2021). Such studies have made use of Convective Available Potential Energy (CAPE) and windshear (often between 0 and 6 km above ground level (AGL) with speeds exceeding 15 ms^{-1}) to identify severe thunderstorms and tornadic environments. Taszarek et al. (2021) also included convective precipitation in their study to include areas of convective initiation, since CAPE alone was not always found to be sufficient. Brooks et al. (2003), Brooks (2009) and Taszarek et al. (2021) showed that severe thunderstorms were often associated with environments of high CAPE and high windshear, resulting in large hail and tornadoes. In an environment with low windshear, CAPE was found to be significant and vice-versa. Brooks (2009) also found that CAPE and shear had a more linear relationship rather than that used for the Bulk Richardson Number, an index often used to classify severe thunderstorms and supercells (Weisman and Klemp, 1982).

As a result of the environment, spring and early summer are a favoured time for severe thunderstorms to develop over South Africa (Blamey et al., 2017; Dyson et al., 2015). High vertical wind shear and CAPE values influence the north-eastern parts of South Africa during the warm season (especially during spring and early summer), contributing to conducive severe thunderstorm environments over the region (Blamey et al., 2017; Dyson et al., 2015; Taszarek et al., 2021). Vertical wind shear values, over the north-eastern parts of the country, are higher during the early summer months (October and November) and decrease as the season progresses, with the lowest values found to occur during February and March (Blamey et al., 2017; Dyson et al., 2015). According to Blamey et al. (2017) and Dyson et al. (2015), the presence and movement of the sub-tropical jet stream, from north to further south, throughout the summer season is the primary influence for the observed upper-level winds and thus the vertical speed shear. The number of days where wind shear values between 850 and 400 hPa exceeded 15 ms^{-1} were found to be high over the southern parts of Gauteng and Mpumalanga with the peak occurring in October to November (Blamey et al., 2017).

As the vertical wind shear decrease throughout the season, CAPE values increase, peaking in December, then decreasing from January through to March (Blamey et al., 2017; Dyson et al., 2015). Dyson et al. (2015), also found other instability parameters to have an increasing trend over Gauteng, with the Showalter Index showing a similar trend to that of the CAPE, while the K-index and elevated

K-index had a general increase throughout the summer season, relating to the observed increase in moisture. This increase in moisture and instability over Gauteng, was found to be the dominant factor in the development of deep moist convection for the mid-to late summer season.

Blamey et al. (2017), used the climatological CAPE and wind shear values obtained from reanalysis data to determine the number of days with a potential for severe convective environments. Due to the higher wind shear in the early summer, over the north-eastern parts of the country, severe environmental days were found to be greater during this period with a peak observed in November. Areas with a higher number of days, included southern Gauteng as well as the southern, eastern high-ground, and escarpment of Mpumalanga. A decrease from the north and west was observed from December onwards, with very few days found to occur over the north-eastern parts of South Africa by February and into March.

2.2 Previous research on radar-derived thunderstorm characteristics and supercell thunderstorms in South Africa

Hailstorms, long-lived thunderstorms and general thunderstorm characteristics were analysed and documented throughout the 1970s and 1980s over the Highveld and surrounding regions, using radar data obtained from the Randburg S-band (non-Doppler) radar located at Houtkoppen (Figure 2-1) (e.g., Carte, 1979, 1981; Carte and Held, 1978; Mader et al., 1986). According to these

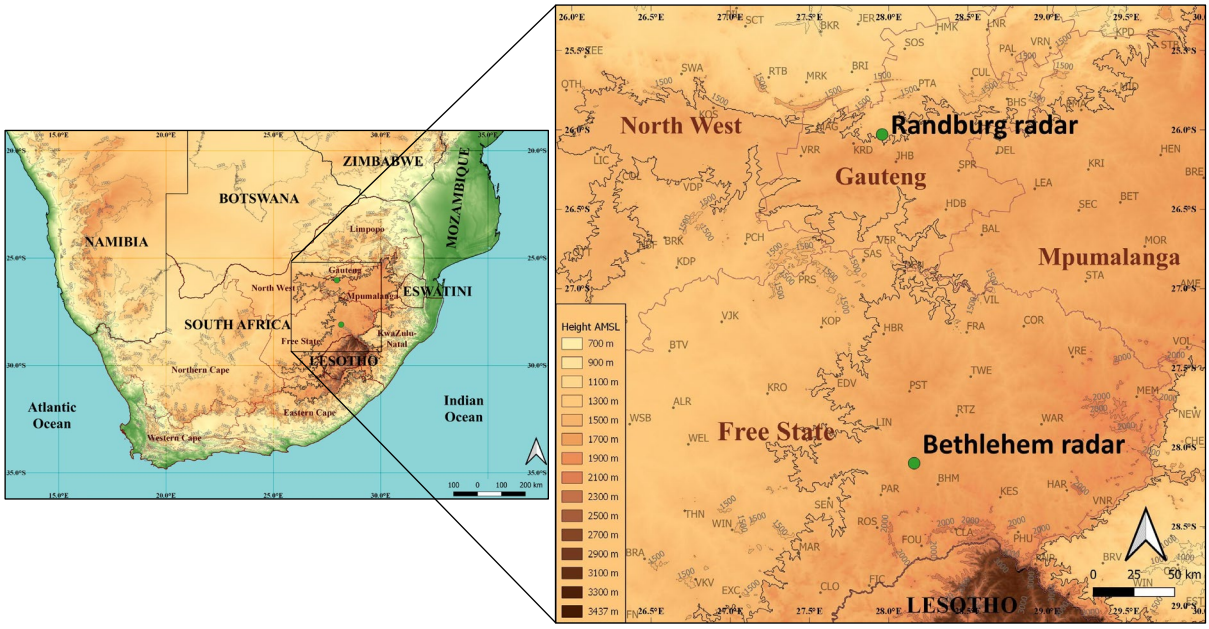

Figure 2-1: The location of the Randburg radar (in Gauteng) and Bethlehem radar (in the Free State). The topography of the area is also shown with each 500 m AMSL contour provided and the 1500 m AMSL contour (Highveld) is highlighted with a thicker, darker line. (Map created using QGIS, topographical data obtained from: (U.S. Geological Survey, 2021))

studies, long-lived thunderstorms as well as supercell thunderstorms were not very common in this region, compared to the Northern Hemisphere, and that most of the long-lived thunderstorms occurred as a result of new development on one flank of the thunderstorm rather than a single persistent thunderstorm (Carte, 1979, 1981).

In a severe thunderstorm outbreak over Pretoria west on 28 December 1976, Carte (1979) analysed one thunderstorm that appeared not to persist as a result of new development but was sceptical about classifying it as a supercell. This thunderstorm displayed similar radar features and matched the definition of supercells, documented in the USA, in that it deviated to the left, contained an appendage on the left flank, although only for a brief period, and contained a steady updraft. However, Carte (1979) was of the opinion that the thunderstorm was not considered to be in a steady state and that the Weak Echo Region (WER) on radar was not as well defined as those in the USA and did not show characteristics of a Bounded Weak Echo Region (BWER). For this reason, it was not classified as a supercell. A few other thunderstorms with a single core were also identified on radar throughout the 1970s but, characteristics did not support a steady state airflow required at the time to be classified as a supercell (Carte, 1981). The concept of the steady state and the requirement for the BWER is discussed in more detail in section 2.3, neither of which are required in the modern definition of a supercell.

According to Carte (1981), the first supercell was only identified on the Randburg radar on 16 and into 17 October 1978 over the Highveld region, 7 years after the installation of the radar. This thunderstorm did not contain well-defined radar features, compared to those identified in the Northern Hemisphere, with a small hook echo and only a WER. It was also noted that there was a lack of strong wind shear on this day. Despite these characteristics Carte (1981) still concluded that this was a supercell, due to the nature of the nearly steady state characteristics of this thunderstorm, that lasted for 5 hours and 45 minutes. In addition, this thunderstorm deviated to the left of flow. It was also highlighted that this thunderstorm was not particularly severe compared to others studied in the region in the past.

Mader et al. (1986) explored some of the characteristics of thunderstorms on the Highveld of South Africa using the Randburg Radar. This study included a sample of case days ranging between 1977 and 1984, although as noted by Steyn and Bruintjes (1990), the dataset may have had a slight bias towards the more severe event days and did not include all thunderstorm days. Various thunderstorm characteristics were examined, including the average lifetime, which was found to be 20 minutes, the average displacement, which was 8 km, and the average speed, which was 27 kmh^{-1}.

They also found that only about 20% of the thunderstorm cells lasted longer than 30 minutes (or moved at a speed exceeding 40 kmh^{-1}), while thunderstorms that did last longer than an hour tended to move more slowly and were more likely to deviate to the left of the mid-level winds. Most of the thunderstorm cells were also found to move from the south-west quadrant for two independent datasets.

Steyn and Bruintjes (1990) investigated thunderstorm characteristics over the eastern Free State, using the Bethlehem C-band radar (Figure 2-1). This was done for convective cloud days between October 1988 and March 1989 and only included thunderstorms between 8:00 and 20:00 South African Standard Time (SAST) due to operational limitations of the radar. Consistent with findings made by Mader et al. (1986), Steyn and Bruintjes (1990) found that the majority of the thunderstorms they investigated were short-lived, generally lasting for less than 30 minutes. Only an average of 10 thunderstorms per day, out of an average of 101 thunderstorms per day, were found to live longer than 1 hour. They also determined that the thunderstorm movement was predominantly from the west to the east, which differed slightly from the south-west to north-east movement determined by Mader et al. (1986). A difference in the average speed was also noted, where Steyn and Bruintjes (1990) observed a slightly higher average speed of 30.6 kmh^{-1}. In the study by Steyn and Bruintjes (1990), all thunderstorm days were considered, and the focus was not on severe event days. Some additional findings made by Steyn and Bruintjes (1990) included that most echoes developed between 13:00 SAST and 17:00 SAST, with the peak between 14:00 and 16:00 SAST. Areas of preferred thunderstorm development included the mountainous areas to the south-west of the radar (Figure 2-1).

de Coning et al. (2000), investigated a supercell that occurred over the north-eastern parts of the Free State, on 29 December 1997. The Bethlehem radar was used to track this thunderstorm, which started in Clarens, south-east of the radar (CLA on Figure 2-1), at around 19:00 SAST and tracked over Bethlehem and up to Petrus Steyn (PTS on Figure 2-1), north-west of Bethlehem, dissipating by 22:00 SAST. This thunderstorm was observed on radar to have a continuous core that lasted more than an hour. A WER was identified during the early stage (around 19:09 SAST), that then developed into a BWER at a later stage (20:55 SAST) on the northern or inflow side of the thunderstorm. A hook echo was observed on the equivalent radar reflectivity factor field (commonly referred to as reflectivity, which is used for the remainder of this dissertation), but no Doppler velocity data was available to confirm a mesocyclone. It is important to note that, although the thunderstorm lasted longer than 4 hours, no mention was made on the length of time the supercell features lasted.

Powell and Burger (2014), examined a well-known outbreak of supercell thunderstorms that occurred over various provinces including Gauteng on 28 November 2013. The S-band Irene Doppler radar, installed in 2010, was used to analyse these supercells and is, as far as the author is aware, the first published analysis of supercells in South Africa using the Doppler radar. Radar characteristics indicative of supercells were identified in numerous thunderstorms on the day, such as the hook echo, BWER, and mesocyclone. In another study done by Powell (2013), the hail mass aloft metric was analysed for 10 known hail cases between 2010 to 2012 over Gauteng, and their tracks were also analysed. It was noted in this study that most hailstorms had a slight deviation from the mean environmental winds, while damaging hailstorms showed to have a more significant deviation to the left. The type of thunderstorms that occurred was not mentioned, however, some of these case dates were known supercell event days (at least one supercell occurred), e.g., on 24 October 2010 and 19 October 2011 (Rae, 2014).

Lekoloane et al. (2021), carried out a study on a supercell that occurred on 11 December 2017 and although the focus was more on the dynamic and thermodynamic aspects, radar data was used to identify this supercell. This supercell developed over the northern Free State and moved over the south-western parts of Mpumalanga, spawning a tornado over the Vaal Marina. Only the hook echo and mesocyclone were mentioned in this study, not a WER or BWER and it was not clear when the features were first identified and when they dissipated. It was also unclear if the supercell or thunderstorm lasted for 7 hours[1].

2.3 Supercell thunderstorms: definition

Thunderstorms can be classified into various categories, including single cells, multicells and supercells. A single cell thunderstorm is defined as a single, small and isolated cumulonimbus cloud with a single updraft, often lasting between 30 to 50 minutes and tends to travel with the mean environmental winds (Houze, 1993; Weisman and Klemp, 1986). A multicell thunderstorm is made up of a group of single cells (two or more) that move together, with each cell usually in a different stage of development, and together produce a collective gust front (Houze, 1993; Weisman and Klemp, 1986). New thunderstorm cells tend to develop along the gust front, which may occur on a preferred storm flank and thus may result in an apparent deviation of the entire thunderstorm complex (Weisman and Klemp, 1986). Due to continuous re-generation of thunderstorm cells, this type of thunderstorm tends to live longer and effect larger areas (Weisman and Klemp, 1986). Multicells can

[1] This was one of the events identified in the research presented in this dissertation and the analysis showed that it was the thunderstorm that lasted 7 hours.

either occur in an unorganised group, be organised into a line or highly organised into a squall-line (Houze, 1993). Both single cells and multicells are known to produce severe weather, although severe weather associated with single cells is usually rare (Houze, 1993; Weisman and Klemp, 1986).

Supercells are the most powerful thunderstorm of the three thunderstorm categories. Although supercells are considered to have the lowest frequency of occurrence of all types of severe thunderstorms (multicells making up the highest percentage), they are significant contributors of damaging severe weather (e.g., large hail, strong damaging winds, long-lived tornadoes and flooding) (Burgess and Lemon, 1990; Moller et al., 1994; Ray, 1990; Weisman and Klemp, 1986). Supercells are defined as a fairly long-lived thunderstorm that contains a single, deep, and persistent rotating updraft, referred to as a mesocyclone (mesoanticyclone for anticyclonic rotating updrafts), and remains in a steady-state for an extended period (Browning, 1964; Burgess and Lemon, 1990; Falk, 1997; Moller et al., 1994; Ray, 1990).

The concept of "steady-state" of a supercell refers to the nearly steady reflectivity and velocity features observed in the supercell, which in the past has been considered a requirement throughout the thunderstorm's lifetime (Lemon, 1977). However, it was noted by some studies (e.g. Doswell III and Burgess, 1993; Lemon, 1977; Moller et al., 1994), that investigations and observations contradict this notion, since supercells evolve continuously and their "steadiness" usually only lasts for less than an hour, rather than throughout the thunderstorm's lifecycle. According to Doswell III and Burgess (1993), a supercell can in fact evolve within a few tens of minutes, while the cellular structure superimposed on this may evolve over a few minutes. The typical evolution of a supercell is described in section 2.6.

The mesocyclone (anticyclone) can be identified using Doppler velocity measurements and is discussed in more detail in section 2.3.3. According to Moller et al. (1994), the definition for the mesocyclone is not clearly defined globally, but suggested that it can be defined as having a vertical vorticity of 10^{-2} s^{-1} extending through a substantial depth of about a third of the thunderstorm's depth and lasting in order of tens of minutes. The depth at which the mesocyclone occurs is not consistent across all research. Bunkers et al. (2006a) defines the mesocyclone as a feature that occurs within the mid-levels, between 2 to 8 km AGL, Feldmann et al. (2021) required the signature to extend through a depth of 3 km, while Hocker and Basara (2008) made no mention of the depth when defining a mesocyclone in their study. According to Beck et al. (2006), low-level mesocyclones are smaller than those at mid-levels.

A time criterion, in order to classify the thunderstorm as a supercell, is required to ensure that the thunderstorm maintains a quasi-steady rotating updraft (Bunkers et al., 2006a; Hocker and Basara, 2008; Moller et al., 1994). The time required for supercell features (e.g., mesocyclone) to last, varies significantly, although values do remain below the typical lifetime of a supercell of 1 to 2 hours (Bunkers et al., 2006a). According to Doswell III and Burgess (1993), the term "persistence", used to describe the mesocyclone, refers to the time taken for an air parcel to travel from the inflow, in the low levels, up to the anvil in the thunderstorm, which they stated taking a few tens of minutes, which was the time criteria used by Moller et al. (1994). Bunkers et al. (2006a) broadly used this time definition, while Hocker and Basara (2008) and Antonescu et al. (2010) more specifically stated a time requirement of at least 30 minutes, which falls within the requirement of tens of minutes. However, in a study done by Christodoulou and Sioutas (2017), the supercell features only needed to last for 10 minutes and that done by Feldmann et al. (2021), required clone to last at least 3 scans (i.e., 15 minutes) which do not meet the criterion provided by Moller et al. (1994). Burke and Schultz (2004) used a longer requirement, stating that the mesocyclone had to last 1 hour or more to be classified as a supercell, which follows a similar classification by Weisman and Klemp (1984).

Rotation of the updraft in a supercell can either be cyclonic (more common) or anticyclonic (less common) (Weisman and Klemp, 1984; Wilhelmson and Klemp, 1978). As discussed in section 2.4 and 2.5, the direction of rotation depends on the environment in which it develops. The rotational velocity values, required to be classified as a supercell, may differ. For example, Bunkers et al. (2006a) used a rotational velocity difference of 20 ms^{-1} across an area less than 10 km, while Hocker and Basara (2008) used a rotational velocity of 7.7 ms^{-1} at base level. Hocker and Basara (2008) based their low value on past supercell event case studies, which showed values ranging between 18 ms^{-1} and 110 ms^{-1}, thus ensuring they were able to account for all possibilities. Feldmann et al. (2021) also used a lower value of 10 ms^{-1}. With regards to the size of the mesocyclone, although not always included as a definition criterion, it is known to have a typical core size of 1 to 10 km in width, which falls within the horizontal *storm-scale* category (Lemon and Doswell III, 1979; Stumpf et al., 1998).

Radar reflectivity signatures were used to identify supercells well before Doppler radars came into existence. The significance of using volume scan techniques to identify thunderstorm characteristics, were highlighted by various authors (e.g., Burgess and Lemon, 1990; Lemon, 1977; Moller et al., 1994) in the analysis of supercells, as earlier studies did not use this technique. The supercell reflectivity features are now most often used in combination with Doppler velocities to identify supercells (Bunkers et al., 2006a; Hocker and Basara, 2008; Moller et al., 1994). According to Doswell III and Burgess (1993), utilising the radar reflectivities alone will not be sufficient to classify a

convective storm. However, others have based their definition predominantly on the reflectivity features and only used the velocity field when available or when the reflectivity features were not clearly defined (e.g., Bunkers et al., 2006a; Klimowski et al., 2003). Radar reflectivity features that are indicative of a supercell include a WER or BWER in the vertical structure, as well as a hook echo or pendant echo in the lower levels of the storm, partially surrounding the updraft (Browning, 1964; Burgess and Lemon, 1990; Lemon, 1977). These radar reflectivity features are discussed in more detail in section 2.3.1 and 2.3.2.

Supercells generally travel to the left of the mean environmental winds in the Southern Hemisphere (to the right in the Northern Hemisphere), but in some cases they may even deviate to the right (or to the left in the Northern Hemisphere) (Browning, 1964; Burgess and Lemon, 1990; Moller et al., 1994). According to Bunkers et al. (2000), the mean 0 to 6 km AGL non-pressure weighted wind correlated well with the deviations in supercell movement observed and thus suggested these levels to calculate supercell movement. For simplicity, in this dissertation, those supercells that deviate to the right or contained relevant radar features on the right flank were named “right-movers” and those that deviate to the left or contained the features on the left flank were named “left-movers”. The direction of deviation and preferred deviation, depends on the environment in which the supercell develops, which is discussed in section 2.4. The deviation of a thunderstorm was required in a study done by Bunkers et al. (2006a), to classify a supercell. However, it is important to note that not all supercells will deviate, especially if the updraft propagation is not strong, and there have been situations where non-mesocyclone thunderstorms deviate (Moller et al., 1994).

Supercells most commonly develop from a multicell thunderstorm and often from a non-severe multicell (Burgess and Lemon, 1990; Lemon, 1977; Ray, 1990; Weisman and Klemp, 1986). A supercell is often described to be a “single cell”, however, this is not always the case, as supercells have been observed to maintain multicell characteristics or multicell structures are superimposed on the supercell (Doswell III and Burgess, 1993; Nelson, 1987; Nelson and Knight, 1987; Ray, 1990; Vasiloff et al., 1986). According to Moller et al. (1994), the supercell classification does not need to include the criteria that the thunderstorm must be unicellular. Supercells that maintain multicellular structures were termed hybrid multicellular-supercellular storms by Nelson (1987) and Nelson and Knight (1987). Some of the observed changes to the reflectivity features are discussed in section 2.3.1 and 2.3.2.

Supercells are typically classified as either classic, Low Precipitation (LP) or High Precipitation (HP) supercells (Moller et al., 1994). In the case of LP supercells, precipitation is substantially lower, especially in the mesocyclone, compared to that of a classic supercell thus they are often smaller in

size and contain lower reflectivities (Burgess and Davies-Jones, 1979; Doswell III and Burgess, 1993; Moller et al., 1994). For HP supercells, precipitation is significant, especially within the mesocyclone, thus contains a larger echo size with persistently high reflectivities (Moller et al., 1994; Moller et al., 1990). Despite the amount or distribution of precipitation, they all have the common feature of the deep and persistent mesocyclone (anticyclone). However, the ability to detect the supercell using reflectivity data may be more difficult as a result of varying precipitation amount (Doswell III and Burgess, 1993). The change observed in reflectivity features, which predominantly impact the identification of the hook echo, is discussed in section 2.3.1.

A supercell may contain a series of periodic mesocyclones at low- and/or mid-levels and is known as a cyclic supercell (Adlerman et al., 1999; Beck et al., 2006; French et al., 2008). Each mesocyclone goes through a similar lifecycle with a new updraft developing once the older one weakens and dissipates. According to Adlerman et al. (1999), the cycling process in the simulated supercells took over 60 minutes, however, both Beck et al. (2006) and French et al. (2008) observed a much shorter cycling process (as short as 6 minutes) using high-resolution Doppler radar.

According to Davies-Jones (2006), all features, movement, etc. which mention areas of “left” and “right” in literature for the Northern Hemisphere, can be interchanged to fit supercells in the Southern Hemisphere. For this reason, all further discussions of supercells in this dissertation have been adapted to fit the Southern Hemisphere, unless otherwise stated. In addition, all figures in section 2.3 to 2.7 have been adapted or obtained for left-moving supercell examples, which are dominant in the Southern Hemisphere. For the right-movers, these features are found on the right rather than left flank of the thunderstorm.

2.3.1 The hook echo

The hook echo, one of the most familiar radar reflectivity features, appears as a hook like appendage or pendant shaped echo on the inflow side of the storm (Figure 2-2) (Burgess and Lemon, 1990; Falk, 1997; Lemon, 1977; Markowski, 2002). The hook echo indicates the presence of the mesocyclone (mesoanticyclone) either at the surface or in the upper levels with cyclonic (anticyclonic) rotation occurring in the area of the hook echo (Burgess and Lemon, 1990; Doswell III, 2001; Falk, 1997; Markowski, 2002). The appearance of the hook echo on radar is still not fully understood, but the most recognised theory is that it occurs due to the horizontal advection of precipitation from the main radar echo around the rotating updraft (Markowski, 2002). Suggestions have also been made,

from reliable radar observations, that the descent of rain in the rear flank downdraft (Figure 2-7) contributes to the formation in some cases, possibly all cases (Markowski, 2002).

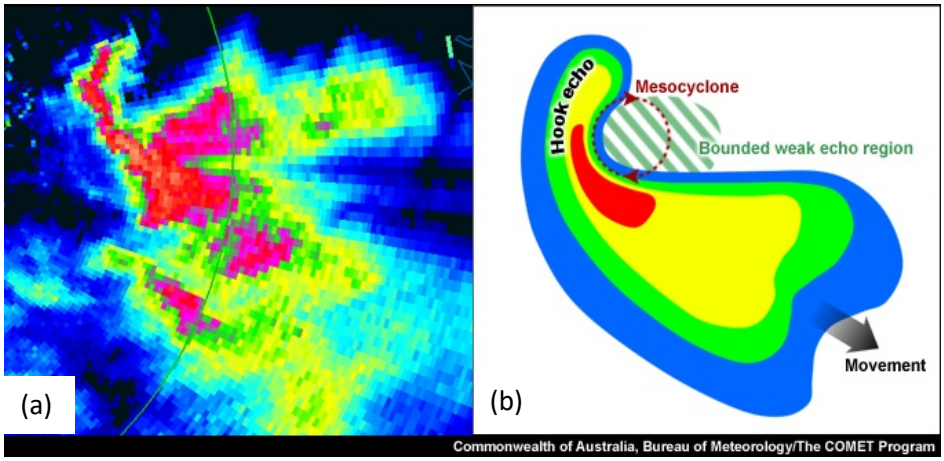

Figure 2-2: (a) A real time radar reflectivity example of a Hook Echo of a left-moving supercell over Australia. (b) A conceptual diagram of a hook echo for a left-moving supercell thunderstorm in the Southern Hemisphere. (Obtained from: The Commonwealth of Australia, Bureau of Meteorology, via the University Corporation for Atmospheric Research (UCAR) COMET MetEd Website at http://www.meted.ucar.edu, and has been fully funded by the Bureau of Meteorology. ©2010, the Commonwealth of Australia, Bureau of Meteorology. All Rights Reserved)

The hook echo for left-movers is located on the rear left flank of the thunderstorm (rear right flank for right-movers) between the boundary of the updraft and the rear flank downdraft, often perpendicular to the thunderstorm's movement (Figure 2-2 and Figure 2-7) (Burgess and Lemon, 1990; Falk, 1997; Markowski, 2002). Associated with this hook echo is a concave region in the thunderstorm's reflectivity echo (Figure 2-2) with a strong reflectivity gradient found on its border (Lemon, 1977). The hook echo for classic supercells is often comprised of fairly low reflectivities, 31 to 45 dBZ, compared to that of the main precipitation core (which us higher) (Doswell III and Burgess, 1993; Moller et al., 1994). Radar observations have shown that the width can be a few kilometres, depth a few hundred meters and can take on a variety of shapes (Markowski, 2002). In a study done by Fujita in 1973 (cited in Markowski, 2002), several hook echo shapes were proposed and are provided in Figure 2-3. This includes the classic hook shape and the pendant shape as well as some other less common shapes, such as the doughnut shape, bird shape and spiral shape.

The hook echo is a low-level feature, usually extending to only a depth of about 3 to 4 km within the supercell, thus the lower elevation scans or the lower Constant Altitude Plan Position Indicator (CAPPI) product of the radar reflectivity data are used to identify this feature (Burgess and Lemon, 1990; Falk, 1997).

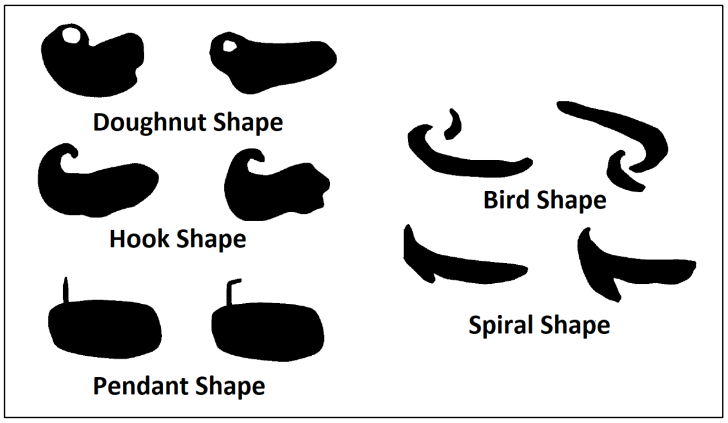

Figure 2-3: The 5 hook echo reflectivity shapes proposed by Fujita adapted for the Southern Hemisphere (left-moving supercells). (Adapted from: Fujita, 1973 cited in Markowski, 2002)

The hook echo is not necessarily a feature observed within all supercells and the description provided in this section is typical for classic supercells. For LP supercells the hook echo is often not well defined and may not be recognisable, with overall lower reflectivities observed (Bluestein and Woodall, 1990; Burgess and Davies-Jones, 1979; Grant and van den Heever, 2014; Moller et al., 1994). In the case of HP supercells, the hook echo is not always present and often the low-level echo is shaped like a kidney bean (Moller et al., 1990). Where the hook echo is visible, the reflectivity values are often similar to the main precipitation core (Doswell III and Burgess, 1993). In the case of a hybrid multicellular-supercellular thunderstorm the hook echo shape is often observed to be that of a pendant rather than a classic hook shape.

2.3.2 The Bounded Weak Echo Region and Weak Echo Region

A WER occurs as a result of a strong updraft and can be identified in most severe thunderstorms, although persists in a supercell (Lemon, 1977). A BWER also occurs due to an intense updraft, usually found to be more intense than those associated with a WER, with precipitation particles suspended in the upper part of the thunderstorm, which are unable to fall back into the core of the updraft (Burgess and Lemon, 1990; Falk, 1997). The rotating updraft also plays a role in the formation of the BWER (Falk, 1997). The definition of a supercell has often included the presence of a BWER, but it was found that not all supercells contain it and may only feature a persistent WER (Lemon, 1977; Moller et al., 1994). It was also noted by Moller et al. (1994), that a storm that contains a BWER is very likely to be a supercell, although it has not been a common stand-alone requirement for supercell classification. The WER is often identified in the early stages of a thunderstorm's evolution, but during the mature stage the BWER may develop (Burgess and Lemon, 1990). In hybrid multicellular-supercellular thunderstorms the BWER was found to be larger in size compared to the classic supercells, while also containing multiple centres indicating multiple updrafts (Nelson, 1987).

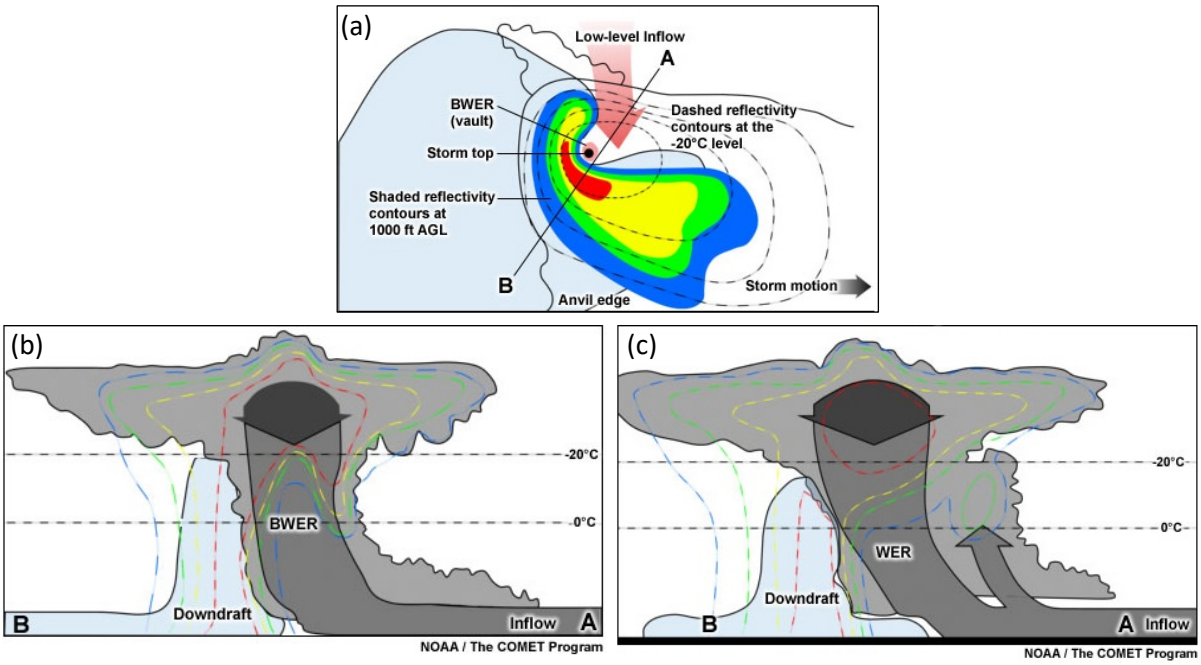

Figure 2-4: A conceptual diagram of a BWER and WER. (a)The low-level radar reflectivities with the -20°C level reflectivity contours shown (dashed lined) and the location of the cross-section taken from A to B. (b) The vertical cross-section taken from A to B showing the location of the BWER in the mid-levels. (c) same as (b) but showing a WER. (Obtained from: The Commonwealth of Australia, Bureau of Meteorology, via the University Corporation for Atmospheric Research (UCAR) COMET MetEd Website at http://www.meted.ucar.edu, and has been fully funded by the Bureau of Meteorology. ©2010, the Commonwealth of Australia, Bureau of Meteorology. All Rights Reserved.).

Since the presence of a WER or BWER is related to the intense updraft within the thunderstorm it is found on the inflow side of the storm, which is either on the left or right flank depending if the supercell is a left-mover or right-mover (Burgess and Lemon, 1990; Lemon, 1977). The BWER is a mid-level feature that can either be identified on plan view or on a cross-section, located near the hook echo or echo top. It is usually easier to identify the hook or the echo top first. In mid-levels a BWER appears as a hole of low reflectivities surrounded by higher reflectivities (Burgess and Lemon, 1990). A cross-section taken through the area of the updraft, almost perpendicular to the thunderstorm's movement (Figure 2-4 (a)), will show a reflectivity signature similar to that shown in Figure 2-4 (b), with higher reflectivities, in the mid-levels, located on both sides of lower to no reflectivities (Burgess and Lemon, 1990; Lemon, 1977).

The WER is also found in the region of the updraft and is identified on a cross-section. In this case the reflectivity signature will only show high reflectivities on one side and above (Figure 2-4 (c)) and will not include the overhang of reflectivity in mid-levels applicable for the BWER (Burgess and Lemon, 1990; Lemon, 1977).

2.3.3 The mesocyclone/mesoanticyclone

A Doppler radar's velocity field will depict the mesocyclone (anticyclone) as a well-defined couplet of inbound and outbound flow (lateral shear) next to each other at an almost constant distance (usually 1 to 10 km in width) (Donaldson, 1970; Rinehart, 2010; Stumpf et al., 1998). According to Donaldson (1970) a strong lateral shear may suggest a local concentration of vorticity. An example of this lateral shear pattern can be seen in Figure 2-5 (feature 100 km north of the radar) for cyclonic rotation, where the negative radial velocities (blue colours) indicate movement towards the radar, while positive radial velocities (red and orange colours) indicate movement away from the radar. Also note the area of apparent no velocity between the two and the location of the maximum velocities relative to the lower velocities. Particles moving perpendicular to the radar have a 0 ms^{-1} radial velocity (Rinehart, 2010). The pattern for anticyclonic rotation would show the negative velocities (blues) on the left and positive velocities (reds) on the right.

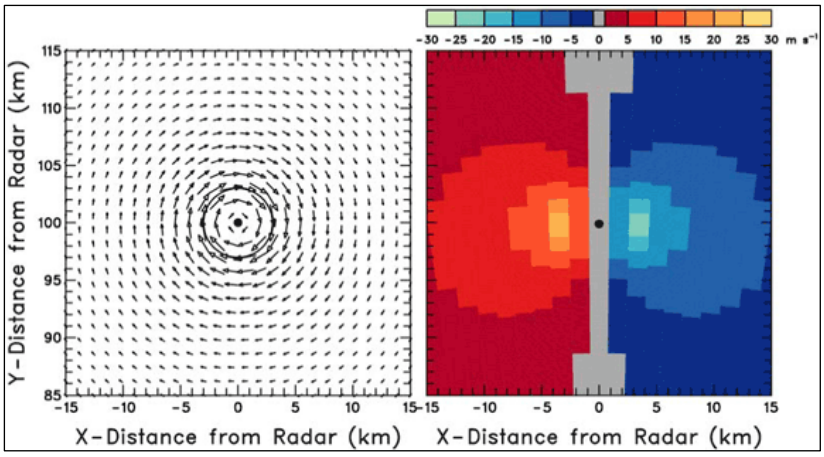

Figure 2-5: A conceptual diagram of the Doppler velocity pattern observed for cyclonic rotation in the Southern Hemisphere with the radar located at the centre of the x-axis (0 km) but 85 km to the south of the feature. (Obtained from: Brown and Wood, 2007)

According to Brown and Wood (2007), a more distorted pattern is observed, compared to this idealised pattern shown in Figure 2-5, when the mesocyclone (anticyclone) is located closer to the radar. Generally, if the storm is close to the radar, the velocity pattern of the lower velocities will extend towards the radar and may converge at the radar if the storm is close enough. Another factor that will influence the pattern observed in the velocity field, is the combination of convergence and divergence with rotation (Brown and Wood, 2007). This will impact the orientation of the zero radial velocity region in the centre of the feature, which will be located at an angle relative to the radar. In addition, motion of the storm or mesocyclone will also impact the circulation pattern as well as the flow field below and around the mid-levels of the storm. More details on the appearance of these patterns can be found in Brown and Wood (2007).

The mesocyclone on the Doppler velocity field is associated with the rotating updraft and is thus located near the hook echo, echo top or WER/BWER identified on the reflectivity field. During the early stages or in some cases even throughout the supercell's lifecycle, the mesocyclone may only be identified in the mid-levels (section 2.3 and 2.6). The CAPPI product, with the assistance of a cross-section, can be used to identify the mesocyclone.

2.4 Environments favouring supercell thunderstorm development and their movement

Environments that are found to be most conducive for the development of a supercell thunderstorm include strong low-level wind shear and high instability, as represented by high values of CAPE and other instability indices (Moller et al., 1994; Ray, 1990). Although such conditions may occur over a broad area, not all thunderstorm cells will take on supercell characteristics, which according to Bluestein and Weisman (2000), may be due to various factors such as mesoscale variations in the environmental conditions or destructive interactions between thunderstorm cells. Johns and Doswell III (1992) observed that the spring season over the USA was very favourable for supercell development, which is also a favoured time for severe thunderstorms over South Africa (Admirat et al., 1985; Blamey et al., 2017; Carte and Held, 1978; Goliger and Lunt, 1997; Held and Carte, 1979; Olivier, 1990).

According to Rasmussen and Wilhelmson (1983), a CAPE value of more than 1500 Jkg^{-1} is required for supercells to develop. However, Johns and Doswell III (1992), reiterated by Moller et al. (1994), showed that a significant number of supercells occurred in conditions with a lower CAPE value, as low as 200 Jkg^{-1}, but in these situations the vertical wind shear was strong. The opposite is also true for cases that develop in areas with high CAPE values, where the wind shear is often observed to be fairly low (Johns and Doswell III, 1992). The climatology of convective instability (e.g., CAPE) over the north-eastern parts of South Africa, was discussed in section 2.1.

Vertical wind shear (speed and direction), especially in the low and mid-levels, has been found (through observations and outputs from numerical models) to be the most important parameter with regards to supercell development (Johns and Doswell III, 1992; Moller et al., 1994). The pattern of vertical wind shear is an important factor as it allows for the tilting of the horizontal vorticity into the vertical, resulting in the development of the rotating updraft (Moller et al., 1994). The thunderstorms inflow layer, which is confined to 3 or 4 km AGL, is considered an important layer for the mesocyclone (anticyclone) development (Moller et al., 1994). Weisman and Klemp (1982; 1984) included the vertical wind shear up to a 6 km depth in the Bulk Richardson Number. Strong vertical shear also

prevents the gust front from moving away from the storm, preventing the updraft and inflow from being cut-off (Houze, 1993).

Studies have shown that supercells can also develop in environments lacking significant directional wind shear, although in such cases the speed shear was found to be very strong (Moller et al., 1994). Most supercell thunderstorms observed in the USA occur in a directionally sheared environment, but there have been observations of those that develop in a unidirectionally sheared environment (Houze, 1993; Weisman and Klemp, 1986). It was found by Klemp and Wilhelmson (1978) that in a unidirectionally sheared environment, where supercells develop as a result of storm splitting (section 2.5), both the left-moving and right-moving supercells have an equal chance of propagating as a self-sustaining thunderstorm. However, in an environment where wind direction changes with height (which is usually more common), either the left- or right-mover will be favoured. Where vertical wind changes in a clockwise direction with height (veering winds), the right-mover will be favoured, while an anti-clockwise change in wind with height (backing winds) will result in favouring the left-mover (Davies-Jones, 1984; Klemp and Wilhelmson, 1978; Weisman and Klemp, 1984). Backing winds with height are most common in the mid-latitudes of the Southern Hemisphere, thus this environment favours left-moving supercell, contrary to that found in the Northern Hemisphere. Dyson et al. (2015) showed that over Gauteng the mean wind direction had a north-westerly to westerly or south-westerly shift in wind direction with height during October to January (surface up to 500 hPa).

Speed shearing is also an important component in supercell development. Weisman and Rotunno (2000) and Falk (1997) found that the wind variations in the lowest 4 to 6 km AGL should be greater than 20 to 25 ms^{-1} (≈ 40 to 50 kts). In a study done by Johns and Doswell III (1992), it was observed that for most cases, the 0 to 6 km and 3 to 6 km mean wind speed was approximately 15 ms^{-1} (≈ 30 kts). This highlights the importance of the strength of the mid-tropospheric wind, although they further noted that the lower 0 to 3 km layer was also important for supercell development. In addition, Droegemeier et al. (1993) determined, through a study on simulated supercells, that the storm-relative winds were required to be at least 10 ms^{-1} (± 20 knots), regardless of the directional shear. The climatology of vertical wind shear over the north-eastern parts of South Africa, was discussed in section 2.1.

2.5 The formation of supercell thunderstorms

Differing theories on the development of the updraft rotation, and thus formation of a supercell, exist. From simulated studies of supercells, it was shown that under unidirectionally sheared

environments (where speed shearing occurs) storm splitting tends to occur (Wilhelmson and Klemp, 1978). However, in the study done by Davies-Jones (1984) it was shown through simulations and observations that rotation can develop simply through the tilting of horizontal streamwise vorticity into the vertical and storm splitting does not occur. The former theory is based on nonlinear effects while the latter is based on linear effects, of which according to Davies-Jones (1984), the nonlinear effects play a very small role in updraft rotation.

In situations of thunderstorm splitting, it was shown that prior to the split, a vortex couplet (one being cyclonic and the other anticyclonic) develops on either side of the thunderstorm's updraft core, which forms when the updraft is superimposed on the horizontal vorticity and is tilted upwards (Houze, 1993; Klemp, 1987). These eddies, that develop in the region of the thunderstorm's updraft, result in strong vertical pressure gradients, which is responsible for the splitting of the thunderstorm (Houze, 1993; Klemp, 1987; Weisman and Klemp, 1986). Two opposing updraft rotations develop within the thunderstorm as the updraft splits, one rotating cyclonically and the other anticyclonically (Ray, 1990; Wilhelmson and Klemp, 1978). As the updrafts move laterally apart the downdraft within the thunderstorm tilts the vortex lines downwards and each thunderstorm cell will have a vortex pair with an updraft and a downdraft (Klemp, 1987). Once the thunderstorm itself splits the one thunderstorm cell (which contains the cyclonic rotating updraft) may deviate to the left of the mean winds, while the other (containing the anticyclonic rotating updraft) may deviate to the right (Klemp, 1987; Weisman and Klemp, 1984; Wilhelmson and Klemp, 1978).

In the study by Davies-Jones (1984) it was shown that cyclonic (anticyclonic) rotation developed in the updraft when storm-relative winds veered (back) with height, which results in streamwise vorticity, or where the environmental flow contained streamwise vorticity in the storm's reference frame. In their study it was shown that as the vortex lines, containing horizontal vorticity, are lifted and cyclonic (anticyclonic) rotation occurs on the right (left) side relative to the shear vector. A counter rotating downdraft also develops.

2.6 The supercell thunderstorm life cycle

Figure 2-6 shows an idealized evolution of radar reflectivities (plan view and cross-section) of a thunderstorm that develops into a left-moving supercell (dominant supercell in the Southern Hemisphere). Initially, the thunderstorm echo in the lower to upper levels is aligned vertically over each other, approximately over the central parts of the thunderstorm echo, with no visible echo

overhang in the upper levels and no strong reflectivity gradient (Figure 2-6 (a) and (b)) (Burgess and Lemon, 1990; Lemon, 1977).

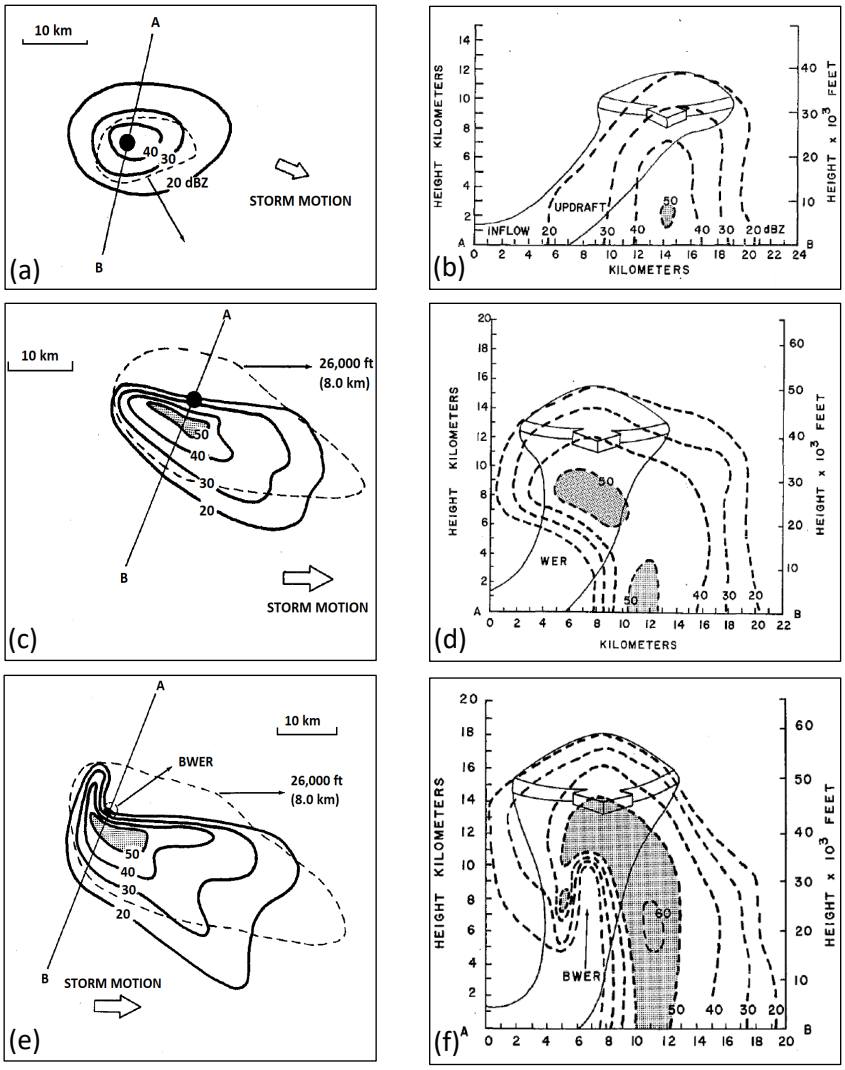

Figure 2-6: (a) Schematic of a radar echo on plan view for a thunderstorm. The solid lines indicate the surface reflectivity contours, the dashed line indicates the echo of more than 20 dBZ at mid-levels, while the black dot indicates the location of the maximum echo top in the upper levels. (b) cross-section through the thunderstorm on 5(a) from A to B, showing radar reflectivity contours (dashed lines) as well as the updraft location. (c) Similar to 5(a) but the thunderstorm is entering its first stage of supercell development. (d) Similar to 5(b) but cross-section taken from 5(c) with the WER indicated. (e) Similar to 5 (a) but the thunderstorm has entered its mature stage of a supercell. (f) Similar to 5(b) but cross-section taken from f(e) with the BWER indicated. (Adapted from: Lemon, 1977; Burgess and Lemon, 1990).

The first stage of a supercell is usually characterised by the development of the WER on the left flank of the thunderstorm (Figure 2-6 (c) and (d)) (Burgess and Lemon, 1990; Lemon and Doswell III, 1979). This occurs due to a strong updraft and strong divergence in the upper levels. As the WER develops the echo top moves to the left-flank over the WER and the low-level echo gradient increases (Figure 2-6 (c) and (d)) (Burgess and Lemon, 1990). It is also at this stage that the thunderstorm will usually slow down and start to deviate (Lemon and Doswell III, 1979). As the updraft intensifies further

the WER expands and the storm top increases in height, while the low-level echo core moves towards the updraft (Lemon, 1977; Lemon and Doswell III, 1979).

The second stage of a supercell is commonly associated with the development of the BWER (although it may not always develop), which occurs as the updraft intensifies and the ice and water content increases around the updraft (Figure 2-6 (e) and (f)) (Lemon, 1977; Lemon and Doswell III, 1979). As a result of the intense updraft, the echo top is often observed to reach its highest altitude during this stage (Burgess and Lemon, 1990; Lemon, 1977). The mesocyclone also develops, usually starting in the mid-levels, at about 5 to 8 km AGL, and is initially located in the area of the BWER (Burgess and Lemon, 1990; Lemon, 1977; Lemon and Doswell III, 1979). Over time the mesocyclone may move down towards the surface. The formation of the supercell is complete once the hook echo has developed (Burgess and Lemon, 1990; Lemon, 1977).

The last stage is known as the collapse stage, which is characterised by an increase in the reflectivities within the BWER, the lowering of the BWER top, a decrease in the size and the eventual collapse of the BWER (Burgess and Lemon, 1990; Lemon, 1977; Lemon and Doswell III, 1979). During this stage the echo top will also decrease in height as the updraft decreases and the size and intensity of the downdraft increases (Lemon, 1977; Lemon and Doswell III, 1979). The low-level hook echo will also dissipate, extending out northwards and then eastwards, wrapping around itself, while the low-level storm echo will increase in size and may weaken (Burgess and Lemon, 1990; Lemon, 1977). The mesocyclone is also known to separate from the BWER, either just before or during this stage, displacing the mesocyclone upwind from the BWER and thus the centre is found within the main precipitation area of the thunderstorm (Lemon, 1977; Lemon et al., 1978; Lemon and Doswell III, 1979). Since the echo top remains near the core of the circulation, it too will shift and will thus be over the main thunderstorm core once again (Lemon, 1977). It is also important to note that the mesocyclone will also move down towards the surface or become stronger at the surface, close to the time of separation (Burgess and Lemon, 1990; Lemon and Doswell III, 1979). It is during this shift in location that the structure of the mesocyclone changes from a rotating updraft to a divided structure, with a cyclonically curved updraft in the warm inflow sector and a strong cyclonically curved downdraft in the cool outflow sector (Lemon and Doswell III, 1979).

2.7 Structural characteristics of the airflow within a mature supercell thunderstorm

A supercell's main components include an intense rotating updraft and two distinct downdrafts (Browning, 1964; Lemon and Doswell III, 1979). The updraft is located on the left flank of the

thunderstorm, UD on Figure 2-7, and is fed by the warm inflow air with strong components from the left flank of the storm (Browning, 1964). The two downdrafts are known as the Rear Flank Downdraft (RFD) and the Forward Flank Downdraft (FFD).

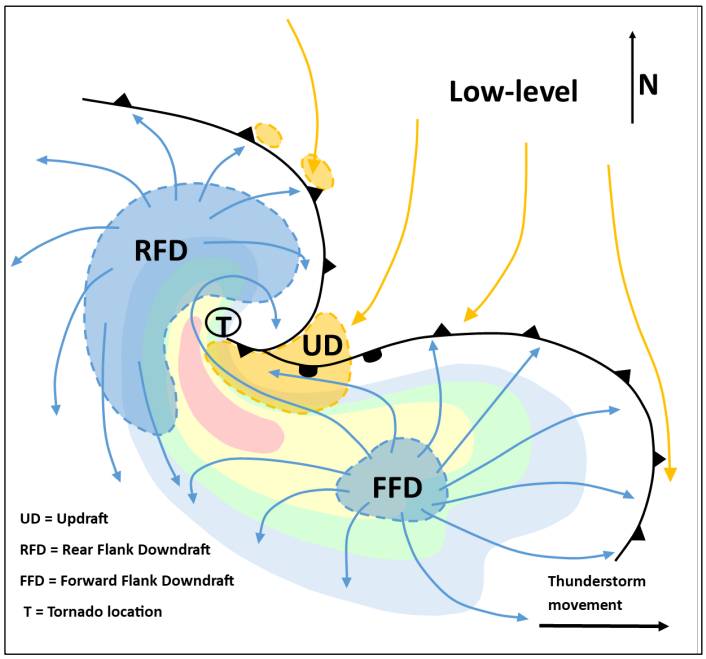

Figure 2-7: Conceptual model of a left-moving supercell thunderstorm in the Southern Hemisphere. Overlain on the low-level radar echo is the surface location of the gust fronts (shown by the solid line with frontal symbols), downdrafts (RFD and FFD) and the updraft indicated by the shaded blue and orange areas respectively. Streamlines showing the direction of the surface air flow are shown by the arrows (blue shows cold air and yellow indicates warm air) and the location of a possible tornado (T) is also shown. (Adapted from: Lemon and Doswell, 1979).

The FFD is located in the main precipitation region of the thunderstorm, downwind of the updraft (Figure 2-7) (Lemon and Doswell III, 1979). The outflow of air at the surface results in a weak discontinuity or gust front on the forward and left flank of the supercell's radar echo (Figure 2-7 ahead of the FFD). This discontinuity may spread out away from the echo with time but may also remain almost stationary along the left flank. This downdraft usually forms before the RFD develops (Davies-Jones, 2006).

The RFD has a slightly more significant role, especially with regards to the mesocyclone structure and tornadogenesis but it also contributes to the storms decay, as it results in the initial disruption of the updraft (Lemon and Doswell III, 1979). This downdraft is located upwind of the updraft on the rear of the rotating thunderstorm (Figure 2-7). Lemon and Doswell III (1979), proposed the upper levels as the source for the RFD, differing to other research which had suggested it originated from the mid-levels. However, they also state that air that reaches the surface from the

RFD is not necessarily from the upper levels but rather that it starts there and mixes with large amounts of air as it descends through the mid-levels.

As this downdraft reaches the surface, it spreads along the surface resulting in a gust front, known as the RFD gust front (Figure 2-7 ahead of the RFD) (Davies-Jones, 2006; Lemon and Doswell III, 1979). The RFD gust front may interact with the weaker gust front from the FFD, thus resulting in a wave structure and an "occlusion" (Lemon and Doswell III, 1979). As a result of convergence, the air from the inflow region ahead of the RFD gust front is forced up, thus resulting in an extension of the updraft (Figure 2-7) (Davies-Jones, 2006; Lemon and Doswell III, 1979). Airflow from the RFD also wraps around the updraft over time (Davies-Jones, 2006).

2.8 Characteristics and properties of supercell thunderstorms

Research on supercell around the world has not only been focused on the environment, dynamics and radar characteristics but has also included an analysis of the general development, evolution, and decay. This section provides information about studies that were done in the USA, Romania, Greece, and Switzerland that looked at the characteristics of supercells in their region. These studies provided the basis for the research presented in this dissertation, and the results obtained in this research (presented in chapter 4 and 5) focused on similar characteristics. A comparison was also provided in chapter 6.

Bunkers et al. (2006a), did a study focusing on long-lived supercells (supercells that lasted longer than 4 hours) over the USA and analysed various properties, such as how and where they developed, how they moved, how long they lasted as well as their method of demise. In their study, 224 long-lived supercells were considered across the central and eastern USA, and they were compared to short-lived events (lasting ≤ 2 hours). Hocker and Basara (2008) also conducted a study on supercell behaviour but focused on the frequency, spatial and temporal aspects of initiation and demise as well as the movement of supercells across Oklahoma between 1994 and 2003, using Geographic Information System (GIS). In their study an attempt was made to identify all supercell events not only the most severe or classic supercells, as has been done frequently in the past, and thus their dataset consisted of 943 supercells.

These studies in the USA inspired similar short climatology radar-based studies of supercells over south-eastern Romania by Antonescu et al. (2010) and in Greece by Christodoulou and Sioutas (2017). In the study done by Antonescu et al. (2010) the case dataset consisted of 282 supercell events that occurred between 2003 and 2006 during the May to September convective seasons. They

analysed the initiation, termination, track and longevity of supercells. Christodoulou and Sioutas (2017), used a database of 49 individual supercell events that occurred on 30 event days over central and northern Greece, during the warm seasons (April to September) of 2004 to 2015, to determine a baseline climatology of supercells. This included the annual, monthly, and daily distribution, general radar characteristics (e.g., maximum reflectivity, storm tops and diameter), lifetime, speed, track, and convective mode. In the study done by Christodoulou and Sioutas (2017), the criteria used to identify the cases included a restriction on reflectivities (which had to be more than 55 dBZ) and Doppler velocity data was not used, thus there was a possible bias towards the more classic and severe supercells. In addition, the thunderstorm had to last for longer than 2 hours thus some short-lived events may not have been captured.

In a more recent study, Feldmann et al. (2021), investigated supercell thunderstorms over the Alpine region in Switzerland. In this study a radar-data-based mesocyclone detection algorithm was implemented over a period of 5 years (2016-2020) across the radar network for the months of April to October. No total number of mesocyclones detected within this period was provided but on average 80 thunderstorms exhibited a mesocyclone per season and on average 22 active days per season. This study also investigated some of the temporal and spatial characteristics of these thunderstorms.

2.8.1 Supercell thunderstorm distribution

Bunkers et al. (2006a) found that most of the long-lived supercell events occurred over the central and eastern parts of the USA and less in the west (an area characterised by rugged terrain and little moisture). It was noted, that not all cases were found, and that coverage was fairly limited in the west. Long-lived supercell frequency was found to be enhanced just east of the Rocky Mountains in the west, which was consistent with areas of thunderstorm initiation. Preferred areas of supercell activity were also noted over Oklahoma (USA), Greece, Romania and Switzerland, including areas with mountainous terrain (Antonescu et al., 2010; Christodoulou and Sioutas, 2017; Feldmann et al., 2021; Hocker and Basara, 2008).

The initiation of supercells is often referred to as the time when a thunderstorm exhibits supercell characteristics, i.e., the mesocyclone is first observed (Antonescu et al., 2010; Bunkers et al., 2006a; Hocker and Basara, 2008). Hocker and Basara (2008) noted a favoured area of supercell initiation over Oklahoma with some of these areas also found to be located close to terrain features. In Greece, Christodoulou and Sioutas (2017), found that supercells were more common over the

northern parts, with the initiation region corresponding to areas near mountainous terrain. Antonescu et al. (2010) also saw higher activity regions of supercell initiation over south-eastern Romania, including the eastern and western parts of Bucharest city, which lies just south of a prominent mountain range, and near the Black Sea also an area characterised by slightly steeper terrain. Feldmann et al. (2021), also noted highest activity of mesocyclonic storms south of the Alps in the Prealpine region. However, the inner Alpine region was found to lack mesocyclones where steep slopes and high-altitudes were found to occur.

Another finding made by Hocker and Basara (2008), regarding the initiation location, was a shift in the location as the year progressed. A general east to west shift was observed with the most western location observed during the summer months, while the mean location moved eastwards again during the last 3 months of the year. Antonescu et al. (2010) noted a north-westward shift from August to July and then back towards the south-east for the remainder of the convective season for the supercells that developed in the Black Sea area.

Both Bunkers et al. (2006a) and Hocker and Basara (2008) noted temporal initiation characteristics of supercells across the USA. Hocker and Basara (2008) found that most supercells in Oklahoma developed between 20:00 UTC and 00:00 UTC (14:00 and 18:00 local time), which corresponded to results by Bunkers et al. (2006a), where the average initiation time of long-lived supercells was found to occur around 22:00 UTC (late afternoon). Bunkers et al. (2006a) also noted a peak frequency of long-lived supercells between 00:00 UTC and 01:00 UTC, with most long-lived events occurring between 18:00 and 08:00 UTC. Antonescu et al. (2010) determined a peak in the activity over south-eastern Romania at around 14:00 UTC (late afternoon) and a secondary peak at 18:00 UTC. Over Switzerland the mesocyclonic storms peaked with general thunderstorm activity with their peak in initiation at 15:00 UTC (late afternoon), although a secondary peak was observed overnight between 00:00 and 04:00 UTC with a minimum occurring around 4:00 UTC (Feldmann et al., 2021). All the above results correspond to the diurnal cycle in daytime heating and development of thunderstorms during maximum solar heating.

The “demise” of a supercell was a term used by Bunkers et al. (2006a) to describe the termination or end of a supercell. It was highlighted that the demise of a supercell did not necessarily mean the end of the thunderstorm itself, as the thunderstorm could evolve into a non-supercell thunderstorm and can continue to persist for some time. Bunkers et al. (2006a), looked at the cause of supercell demise for long- and short-lived events and did not include the temporal and spatial characteristics. Hocker and Basara (2008), on the other hand, looked at the temporal and spatial

characteristics. They found that most supercells across Oklahoma generally dissipated between 23:00 UTC and 03:00 UTC (late afternoon to evening) and the location of supercell demise was common over the northern and north-eastern parts of Oklahoma.

2.8.2 Supercell thunderstorm movement and lifespan

All 4 studies discussed in section 2.8, analysed the general propagation track of supercells. Findings by Hocker and Basara (2008) revealed that supercells across Oklahoma had a mean track from the south-west between January and May, north-westerly track between June and September, and then south-westerly track once again for the last 3 months. Bunkers et al. (2006a) also determined a general track from the south-west, west and north-west for long-lived supercells across the USA, although regional variations did occur. Only about 10 supercells were noted to move from the south and even less from the north. In general, long-lived supercells were noted to have very little deviation in their path (track). Antonescu et al. (2010) observed that supercells generally moved from the south-west to north-east over south-eastern Romania and Switzerland respectively, during the convective thunderstorm months, which differs to that found by Hocker and Basara (2008), over Oklahoma (USA) during a similar time, but corresponds to the general finding made by Bunkers et al. (2006a) for the entire USA. Christodoulou and Sioutas (2017) also found that, in Greece, supercells tended to move from either the west, south-west or north-west, which was also the dominant direction of movement over Switzerland as shown by Feldmann et al. (2021).

Both Hocker and Basara (2008) and Antonescu et al. (2010), examined the general lifespan of supercells and came to a similar conclusion, that a significant portion of supercells lasted 30 minutes to an hour, with numbers dropping significantly with time. Antonescu et al. (2010) did not observe any supercells that lasted more than 5.5 hours over Romania, while the longest lasting supercell found by Hocker and Basara (2008) was around 7.5 hours over Oklahoma. Christodoulou and Sioutas (2017) also looked at the lifespan and found that in Greece the supercells had an average lifetime of 3 hours, although this was based on the entire thunderstorm's lifespan. They also determined the average speed and distance travelled by supercells, being 31.2 kmh^{-1} and 91.8 km respectively, however, once again this was based on the entire thunderstorm. Bunkers et al. (2006a) found that on average, long-lived supercells (those lasting longer than 4 hours) existed for 5.5 hours, while short-lived events (lasting less than 2 hours) lasted on average 1.4 hours over the USA.

2.9 Summary

Thunderstorms frequent the north-eastern parts of South Africa from September to February, with severe thunderstorm activity peaking during the early season. In particular, hailstorms were found to peak during November. In spring and early summer, weather systems are predominantly extra-tropical in nature with higher values of vertical wind shear and sufficient convective instability to support the development of severe thunderstorms. During the late summer months weather systems are more tropical in nature with instability increasing but vertical wind shear decreasing. This corresponds to a decrease in the severe convective environment over the north-eastern interior during the later summer months. Numerous studies examining thunderstorm characteristics and severe thunderstorms using radar data, have been carried out over the north-eastern interior of South Africa, although only a small number of case studies on supercell thunderstorms have been conducted. Details on these studies were provided in section 2.2.

Supercells are a type of severe thunderstorm that contain a single, deep, and persistent rotating updraft (mesocyclone) that lasts for tens of minutes. On radar, characteristic features include the hook echo and BWER or WER on the reflectivity field and a mesocyclone/mesoanticyclone on the Doppler velocity field. The mesocyclone (anticyclone) usually starts at mid-levels and may move down to the lower levels, with a horizontal width between 1 and 10 km. Supercells can also be classified as HP or LP, for which the hook echo feature is often not well defined. In addition, supercells can also experience a cycling process, whereby a new rotating updraft develops as the old one dissipates and thus it may lose supercell features for a short period of time. This information presented in section 2.3, provided the foundation on which the criteria for supercell identification in this research was based and discussed in section 3.5.

The rotating updraft may either occur on the rear left flank with a cyclonic rotation (left-moving supercells) in the South Hemisphere or on the right flank with anticyclonic rotation (right-moving supercells). Adequate vertical wind shear (speed and direction) and instability is required for supercell development, although the former is the most important factor. Backing wind directions with height, which are favoured over South Africa, predominantly result in left-moving supercells, while veering winds predominantly result in right-moving supercells, although both may occur in a unidirectionally sheared environment. Details on the formation, life cycle and structure of supercells were also provided in this chapter (section 2.5 to 2.7), which provided further background to help develop the identification criteria used to identify supercells in this research which is provided in section 3.5.

Short-term climatological studies of supercell thunderstorms in the USA, Romania, Greece and Switzerland have been carried out to investigate their characteristics specific to the region. This included spatial and temporal characteristics as well as characteristics relating to their initiation, track, and demise. Details of these studies, which inspired the research conducted in this dissertation, were discussed in this chapter (section 2.8), and forms the basis of the rationale use to depict the results presented in chapter 4 and 5.

Chapter 3: Data and Methodology

This chapter provides information about the data and methodology that was used in this study. The first two sections provide information about the study period (section 3.1) and study area (section 3.2). This is followed by detailed information about the SAWS radar data that was used (section 3.3). Then information regarding the LROSE software is discussed, in which the Rview and TITAN algorithm is found (section 3.4), as this was used to view and analyse the data. Following this, is the methodology that was used to identify supercell thunderstorms (section 3.5) and to analyse their characteristics which includes their initiation, lifespan, track, and demise (section 3.6).

3.1 Study period

Only supercells that developed in the warm season were considered, where the warm season was defined as the spring and summer months (September to February). Severe thunderstorms and supercells are known to occur outside of this season (e.g., March, July etc.) (Dyson et al., 2021; Rae, 2014), but since lightning (thunderstorm) activity and especially severe thunderstorms are common in the spring and summer months (Admirat et al., 1985; Blamey et al., 2017; Carte and Held, 1978; Goliger and Lunt, 1997; Held and Carte, 1979; Olivier, 1990), only these months were considered in this study. Radar data was obtained for 10 seasons between September 2010 to February 2020 and all available days were analysed where thunderstorms occurred.

3.2 Study area

Data from the Irene and Ermelo radar was used, confining the study area to the 200 km radial range of each radar, which is shown by the circles on Figure 3-1. The area thus includes the Gauteng, Mpumalanga, extreme southern Limpopo, western North-West, northern Free State, and the northern KwaZulu-Natal provinces. Eswatini (previously known as Swaziland) also falls within the coverage area of the Ermelo radar. The study area is referred to as the "radar coverage area" in this dissertation but note that the greatest portion covers the areas of the Gauteng and Mpumalanga provinces.

The radar coverage area falls within the elevated plateau region that extends approximately 1000 m Above Mean Sea Level (AMSL), with large areas reaching 1500 m AMSL (Figure 3-1) (Taljaard, 1994). Simpson and Dyson (2018) defined the Highveld as the area of 1350 m AMSL, while others (e.g., Mader et al., 1986; Rae, 2014) mention areas of 1500 m AMSL. In this dissertation the area of 1500 m

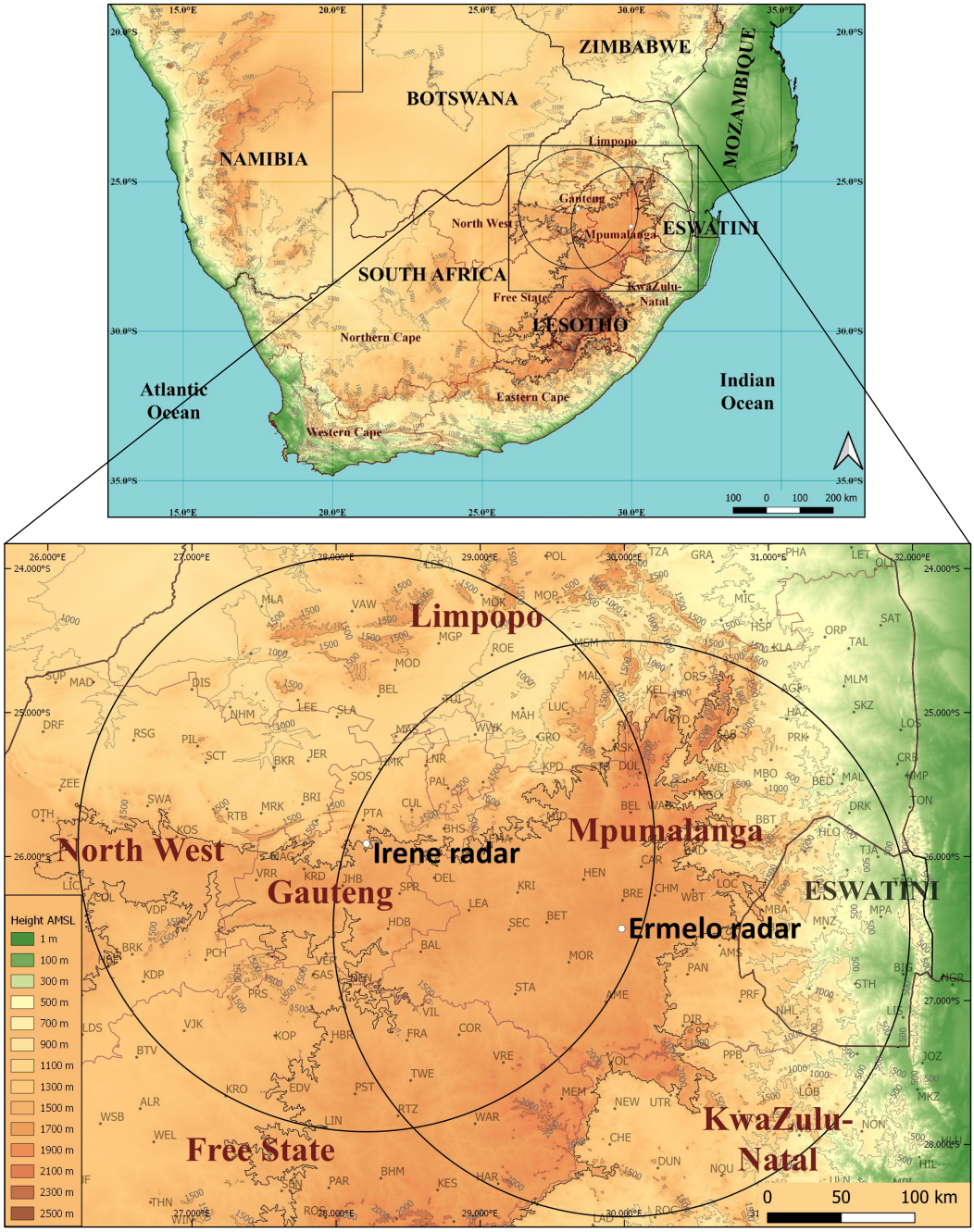

Figure 3-1: The study area which includes the 200 km range ring (black circle) from both the Irene and Ermelo radar. The topography of the area is also shown with each 500 m AMSL contour provided and the 1500 m AMSL contour (Highveld) is highlighted with a thicker, darker line. Various suburbs are shown (indicated by the three letters). (Map created using QGIS, topographical data obtained from: (U.S. Geological Survey, 2021))

AMSL or more was considered as the Highveld, which dominates the southern and central parts of the radar coverage area (Figure 3-1). Due to the elevated terrain, the average surface pressure in the study area is therefore closer to 850 hPa. For this reason, the 850 hPa pressure level was used to depict surface conditions in Figure 3-2 and Figure 3-3. The escarpment, a steep change in the topography, extends over the eastern parts, dropping rapidly into the Lowveld, the low-lying area in the topography, in the extreme eastern (Figure 3-1).

The mean synoptic conditions over South Africa during the warm season are shown in Figure 3-2, while Figure 3-3 provides the mean monthly vertical wind profile over the Irene and Ermelo radar location. The mean synoptic circulation and winds were created using National Centre for Environmental Prediction (NCEP) reanalysis-2 data (Kanamitsu et al., 2002) from 1979 until 2020. This data has a horizontal resolution of 2.5° and was used to provide an overview of the synoptic conditions occurring over South Africa and not to predict or describe synoptic conditions specific to supercell thunderstorm development.

During September, the early spring season (Figure 3-2 (a)), the surface trough (850 hPa) is located along the west coast, while the high pressure north-east of the country extends its ridge over the eastern parts of South Africa. The upper high pressure (500 hPa) is found to the far north of South Africa with a westerly to north-westerly flow over South Africa. The winds are thus found to back from a northerly to north-easterly wind at the surface to a north-westerly wind at 700 hPa but westerly from 600 hPa upwards (Figure 3-3). By November (Figure 3-2 (b)) the surface trough has migrated

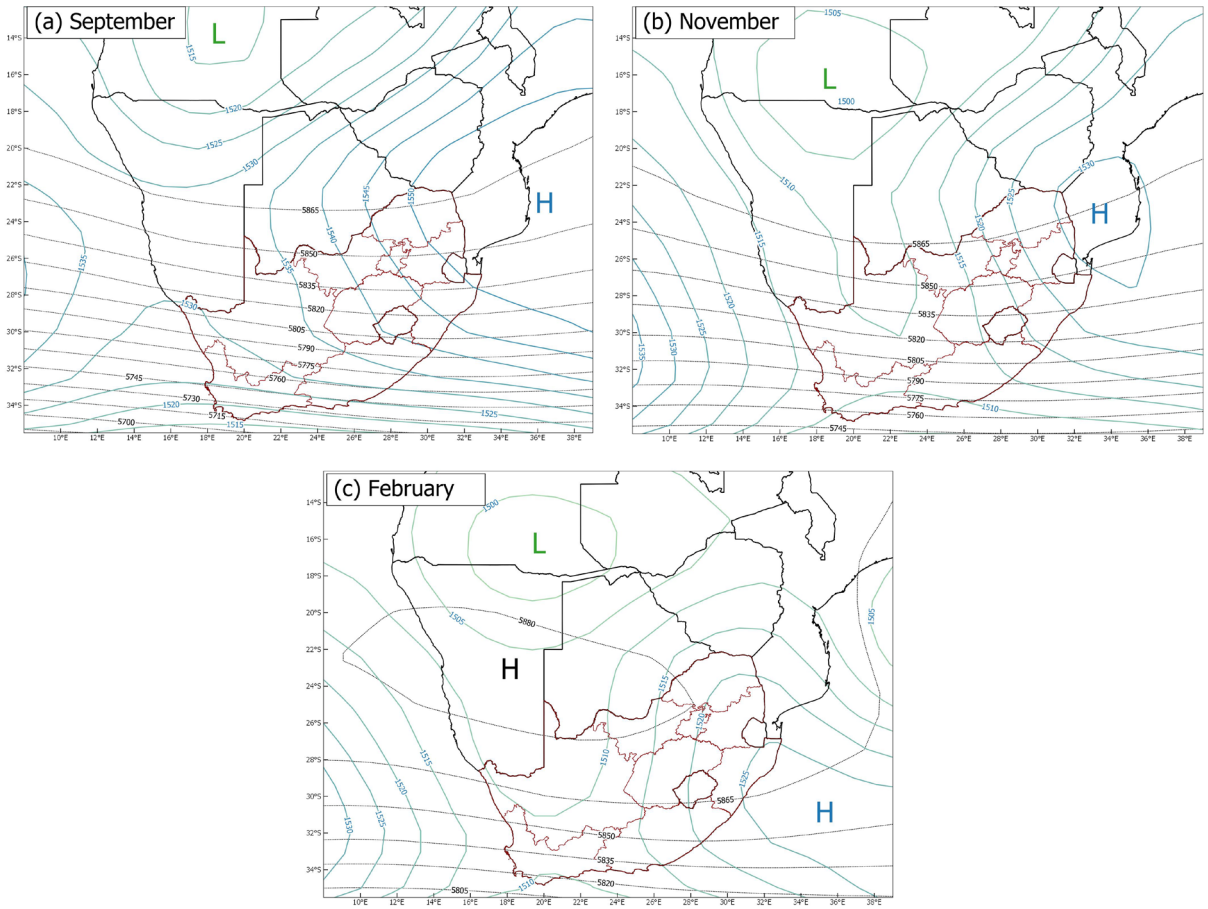

Figure 3-2: Long-term mean monthly 850 hPa (solid colour contours) and 500 hPa (dotted black contours) geopotential heights over southern Africa for (a) September, (b) November and (c) February. The blue "H" indicated the surface high, pressure, green "L" indicates the surface low pressure and the black "H" indicates the upper high pressure.

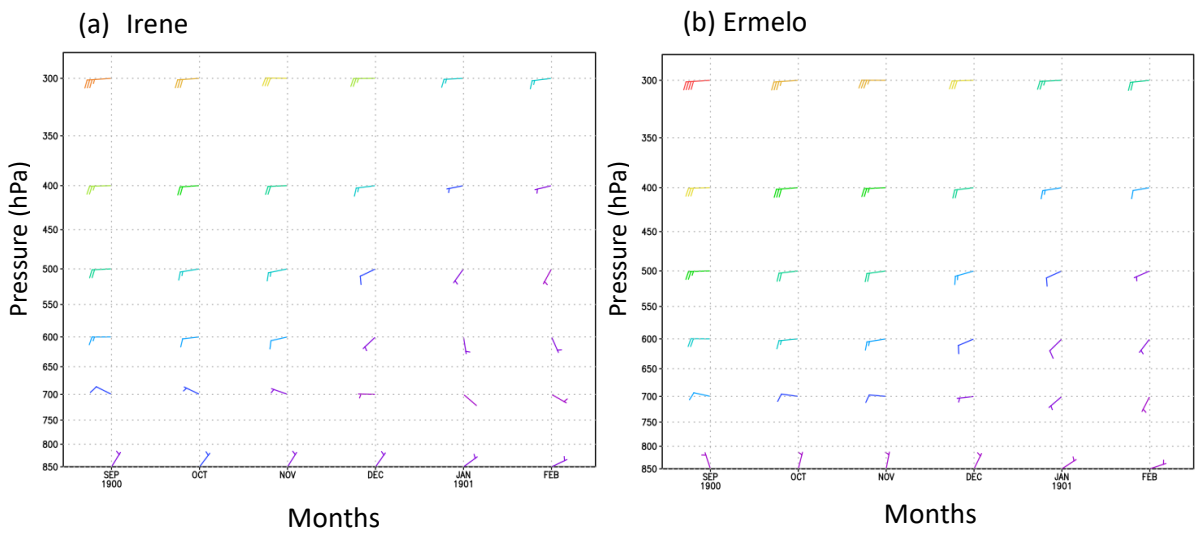

Figure 3-3: The mean vertical wind direction and speed (in knots) for September to February over (a) Irene and (b) Ermelo.

south and eastwards over the western interior of South Africa and the surface high has moved west over southern Mozambique, thus a northerly to north-easterly flow remains in the lower levels over the eastern parts of South Africa. In the upper levels the wind shifts to a westerly to south-westerly flow, as the upper high pressure system migrates further southwards. The vertical wind profile over Irene and Ermelo (Figure 3-3), shows this shift in wind direction from the surface upwards. These conditions are similar for October through to December, although winds in the upper levels decrease in speed from December. In February (Figure 3-2 (c)), the surface trough has migrated westwards again, the surface high has moved south-eastwards, while the upper high has moved further south over southern Namibia and south-western Botswana. This results in both a further decrease in speed, particularly at 500 hPa, and a shift in the wind from north-easterly at the surface to south-easterly at 700 hPa and south-westerly from 500 hPa over Irene but south-westerly from 700 hPa upwards over Ermelo. Although not shown, the subtropical jet stream is found to migrate further southwards during the warm summer months, contributing to the decrease in upper levels winds as the season progresses (Blamey et al., 2017; Dyson et al., 2015).

As discussed in section 2.3 and 2.4, supercells are known to deviate to either the left or right of the mean environmental winds (Browning, 1964; Burgess and Lemon, 1990; Moller et al., 1994) and according to Bunkers et al. (2000), the mean 0 to 6 km AGL non-pressure weighted wind should be considered. The NCEP reanalysis 2 data was used to calculate the 850 hPa (surface) to 400 hPa (≈6 km AGL) mean wind direction and speed for each month as well as over the entire warm season (Table 3-1). A shift in the mean 0 to 6km wind directions are observed across the warm season, from a westerly wind in September for both locations to southerly over Irene and west south-westerly over

Ermelo in January. As discussed previously the mean wind speed also shows a decrease with lower values observed over Irene compared to Ermelo.

Table 3-1: The mean monthly and mean warm season 850 to 400 hPa (0 to ≈6 km) wind speed and direction for the area near Irene and Ermelo.

	Irene		Ermelo	
	Wind speed (kts)	Wind Direction (°)	Wind speed (kts)	Wind Direction (°)
September	11.3	278	16.5	273
October	9.9	275	14.7	270
November	8.8	273	13.2	269
December	5	260	9.5	261
January	1.3	188	5.5	246
February	1.6	145	4.4	238
Warm season	**5.7**	**269**	**10.5**	**265**

3.3 Radar data

Radar data was provided by the SAWS from both the Irene and Ermelo radars, which are Gematronik METEOR 600S systems operating in the S-band frequency and are Doppler capable with only a horizontal polarisation. The Irene radar became operational in January 2010, although high quality data was only available from October 2010, while the Ermelo radar became operational in November 2010, although data was available from September 2010 (Becker, 2014). Multiple changes were made to the radar scan strategy and setup over the 10-year period and have been provided in Appendix 1 and discussed in more detail in section 3.3.2.

A weather radar transmits a pulse of electromagnetic radiation into the atmosphere, which travels approximately at the speed of light, and receives back scattered energy from targets within the atmosphere (Rauber and Nesbitt, 2018; Rinehart, 2010). This is done via the antenna, which rotates at a specified elevation angle, antenna speed and Pulse Repetition Frequency (PRF). The PRF is the rate at which the radar transmits these pulses. As the radar rotates it sends out a series of pulses at intervals long enough for each pulse to reach a specified distance and returns before the next pulse is transmitted. The antenna will continuously move and collect information on the signal amplitude and Doppler phase shift at specified azimuths and range gates, which are determined by the user. Once the radar has scanned the atmosphere 360° around it, at a specified elevation angle, the radar will be angled up or down to a new elevation angle and repeat the process, thereby scanning as much of the atmosphere as possible in the desired temporal resolution. The radar measures the power (amplitude) that has been returned from targets in the atmosphere and this power is converted into a quantity known as the equivalent radar reflectivity factor, commonly referred to as reflectivity (the term used throughout this dissertation). In addition, the phase shift of the returned energy is measured and is used to calculate the radial velocity of moving targets. More details regarding the

radar hardware components and how radars work can be found in Rauber and Nesbitt (2018) and Rinehart (2010).

3.3.1 Data availability

According to the World Meteorological Organization (WMO), radar availability should be 96% or more on an annual basis (WMO, 2018). Although a large dataset was available for both the Irene and Ermelo radar, gaps in the data were unfortunately present. This included either a full day or part of the day without data, which may have been caused by either power outages, equipment failure or availability of spare parts to name a few. There were also some data quality issues noted on some of the days when analysing the data. For example, a drop in power was observed from one scan to the next (later increasing again), spikes appeared within the data (not related to beam reflection (see Becker, 2014) or electromagnetic spikes (e.g., radio interference) or files were corrupted with no usable data contained within the file. Although not flagged as a day with data issues, there were also some instances, that one scan contained reflectivity data but no velocity data and vice versa.

Figure 3-4 provides the radar data availability per season for both Irene and Ermelo for the warm seasons considered in this study. The Ermelo radar suffered more outages compared to Irene, where of the 1813 possible days, a total of 749 full days (or majority of the day) were missing, while the Irene radar had 174. Only during the 2019-2020 summer season did the Ermelo radar availability exceed the WMO recommended 96%, while Irene met or exceeded this value during each season

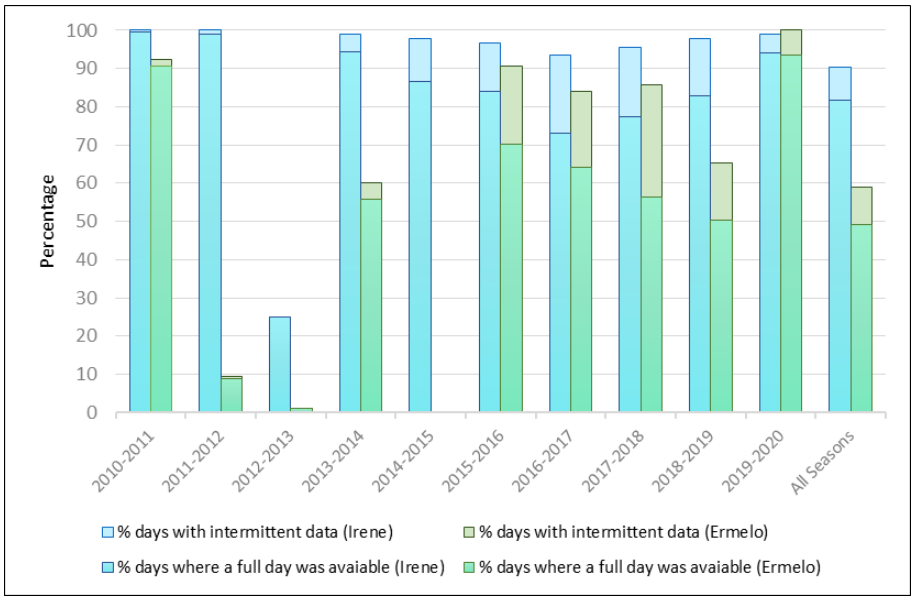

Figure 3-4: Radar data availability per season and for all seasons for the Irene and Ermelo radar. The percentage (%) days with intermittent data, days where all data was available and the overall available days with data (sum of the two) is shown on the graph.

except in 2012-2013 and 2016-2017. It is important to note that this availability was based on 6 months and not an entire year. In total 82% of the days were unaffected by data issues (i.e., full day was available) for the Irene radar and 49% for the Ermelo radar (Figure 3-4).

The largest gap in the data for the Irene radar was in 2012-2013 (Figure 3-4), with no data in 2012 up until the 13 January 2013. Ermelo radar also experienced a similar gap during this season, which lasted until 1 February 2013. In addition, major gaps in the Ermelo radar dataset were also noted in 2011-2012 and 2013-2014, while the entire 2014-2015 season was not available (Figure 3-4). Ermelo thus only has a more reliable dataset from the 2015-2016 season onwards although a slight drop in availability was noted during the 2018-2019 season (Figure 3-4).

Figure 3-4 also provides the percentage of days where intermittent data occurred. This either occurred in the morning, afternoon, or both. Data was either missing for the entire period (e.g., afternoon), part of the period (e.g., a few hours in the afternoon) or there may have been some data quality issues. If only 1 or 2 scans were missing within an hour it was not flagged as intermittent data. Intermittent data may not have always impacted the analysis of events. In total, the Irene radar experienced intermittent data on 9% of the days and the Ermelo radar 10%. This varied from one season to the next (Figure 3-4), although intermittent data mostly occurred during the last 5 seasons. As determined in other regions around the world, supercells often develop in the afternoon (2.8.1). In total Irene experienced 103 days where data was either missing, intermittent or had general issues between 12:00 UTC and 23:59 UTC and Ermelo had 116 days. Similarly, but less significant, data issues for the first 12 hours of the day (from 00:00 UTC until 11:59 UTC) were experienced on 109 days on the Irene radar and 126 days on the Ermelo radar.

The radar availability for each month was also analysed (not shown) and the availability for each month, for the 10 seasons considered, showed small variation. Irene radar showed the highest to be in February at 98% and lowest in October and December at 87%. Ermelo experienced a much lower overall availability, but also had small variation from one month to the next, with the highest in February at 64% and lowest in October at 50%. Although the variations were small, availability could still have resulted in a bias towards a specific month if for example all unavailable days in that month were days on which supercells occurred.

3.3.2 Data specifications

The Irene radar is situated at 25.9°S and 28.2°E (Figure 3-1), at an elevation of 1560 m AMSL, while the Ermelo radar is situated at approximately 26.5°S and 29.98°E (Figure 3-1), at an elevation of

1785 m AMSL. The Irene and Ermelo radar operate at approximately 10 cm wavelength (S-band range) and have a beamwidth of approximately 1°, although exact values differ slightly between the two radars (Table 3-2). According to the metadata, there were also some slight changes made to the Ermelo radar's beamwidth and wavelength from September 2015 and again from September 2019 (Table 3-2). Both the Irene and Ermelo radar originally operated at a maximum radial range of 300 km from the radar, but was adjusted to a 200 km range by 14 January 2013 and October 2013 respectively (Table 3-2). In this research only data up to 200 km was used, regardless if data up to 300 km was available. The reason for this is discussed in sections 3.3.2.2 and 3.3.2.3.

Table 3-2: Radar data specifications for the Irene and Ermelo radar obtained from the metadata.

	Irene radar	**Ermelo radar**
Latitude	25.911816°S	26.497955°S
Longitude	28.210766°E	29.984056°E
Height	1560 m AMSL	1785 m AMSL
Wavelength	10.452 cm	**Initial:** 10.563 cm **≈ September 2015:** 10.0 cm **≈ September 2019:** 10.601 cm
Frequency	2.87 GHz	**Initial:** 2.84 GHz **≈ September 2015:** 3.0 GHz **≈ September 2019:** 2.83 GHz
Beamwidth	0.93°	**Initial:** 0.94° **≈ September 2015:** 1° **≈ September 2019:** 0.93°
Pulse width	1.67 µs **From 21/10/2010 – 5/11/2010:** 0.83 µs	1.67 µs **From 01/09/2010 – 5/11/2010:** 3.33 µs
Elevation angles	**Initial:** 0.5°, 1.3°, 2.1°, 3.1°, 4.2°, 5.5°, 6.9°, 8.5°, 10.3°, 12.4°, 14.7°, 17.4°, 20.4°, 23.8°, 27.6° and 32° **From 21/10/2010:** 0.5°, 1.3°, 2.3°, 3.4°, 4.7°, 6.2°, 7.9°, 9.9°, 12.2°, 16.8°, 17.8°, 21.3° and 30° **From 06/11/2010:** 0.5°, 1.3°, 2.3°, 3.4°, 4.7°, 6.2°, 7.9°, 9.9°, 12.2°, 16.8°, 22° and 30°	**Initial:** 0.5°, 1.3°, 2.3°, 3.3°, 4.6°, 5.9°, 7.5°, 9.2°, 11.2°, 13.5°, 16.1°, 19°, 22.3°, 26°, 30.2° and 35° **From 06/11/2010:** 0.5°, 1.3°, 2.3°, 3.4°, 4.7°, 6.2°, 7.9°, 9.9°, 12.2°, 16.8°, 22° and 30°
Maximum range	**Initial:** 300 km **≈ 14/01/2013:** 200 km	**Initial:** 300 km **≈ October 2013:** 200 km

Four volume files are created for both the Irene and Ermelo radar once scanning has taken place. The first is a raw reflectivity field (measured in dBZ) without any filters applied, the second is corrected reflectivity field (measured in dBZ) with pre-processed filters applied, the third is the Doppler velocity measurement (measured in ms^{-1}) and the last one is the spectrum width (measured in ms^{-1}). In this study only the first 3 data fields were used, of which the uncorrected reflectivity field was only used where data was negatively impacted by filters or the removal of data due to the applied thresholds.

During signal processing thresholds are applied to the data to remove poor quality data, although they may remove useful data depending on the setup of the radar (SelexES-Gematronik,

2014). Far ranges are impacted the most as the signal is often weaker and it becomes more difficult to differentiate it from noise. Initially both radars operated at a 300 km range, but it was adjusted to 200 km for the higher levels (6.2° and upwards) from 6 November 2010, while the lower levels were adjusted by 14 January 2013 and October 2013 for the Irene and Ermelo radar respectively. The largest impact was noted before 6 November 2013, where a significant amount of data was removed, therefore the uncorrected reflectivity field was predominantly used during this period.

Filters (Doppler filter, speckle remover, etc.) are applied to the raw data, which remove ground clutter, anomalous propagation and other non-meteorological features, without removing the meteorological features (Becker, 2014; Rauber and Nesbitt, 2018; SelexES-Gematronik, 2014). According to the metadata and Becker (2014), filters such as the Infinite Impulse Response (IIR) Doppler filter and speckle remover are included for both the Irene and Ermelo radar. No other quality control measures are applied to the data, such as the removal of velocity folding through correction algorithms[2].

3.3.2.1 Scan strategy

The Irene and Ermelo radar use a volume scan technique, whereby the antenna rotates 360° moving in 1° azimuth intervals at a specific elevation angle, although from 6 November 2010 until February 2011 the Irene radar's lower elevation scans (0.5° to 4.7°) operated at 0.8° azimuth intervals (Appendix 1) (Becker, 2014). As a result of various adjustments made to the elevations scans, the total scan time varied between 325 to 359 seconds for both radars (Appendix 1), but the overall temporal resolution of the data was approximately 6 minutes, with the processing of the data included. Both radars scan from the highest elevation first, then move down through various elevations until they reach their lowest elevation scan (Becker, 2014). One of the advantages of scanning from the top down, is that the critical lower part of the thunderstorm, that impacts the surface, is the latest information available (the top will be approximately 6 minutes old). The antenna is also never pointed directly above the radar thus a cone shaped area of no data, known as the cone of silence, is found directly above the radar (Rinehart, 2010).

For most of the dataset both radars had a 12-level scan strategy starting at 30° and ending at 0.5°, but prior to 6 November 2010 both had a 16-level scan strategy as well as some slight differences in the elevation angles (Table 3-2). In addition, from late October 2010, the Irene radar scan strategy consisted of 13 levels (Table 3-2).

[2] EH Becker (scientist at the Centre for Climate Research, Singapore), 2021, personal communication, 15 October.

Initially, both radars operated at a PRF of 500 Hz and thus a Nyquist velocity of approximately ± 13 ms^{-1} (Appendix 1). The Nyquist velocity is the maximum velocity that a Doppler radar can detect, which is limited by the range at which the radar operates (Rinehart, 2010). Both the maximum range and Nyquist velocity depend on the PRF, thus resulting in the Doppler Dilemma, whereby an inversely proportional relationship exists between the two (Rinehart, 2010). Increasing the Nyquist velocity will decrease the maximum range and vice versa.

Staggering the PRF into different ratios, by alternating between a higher and lower PRF from one pulse to the next, increases the velocity, while still maintaining a longer range at which a radar can operate at (Holleman and Beekhuis, 2003; Joe and May, 2003). One disadvantage to using this method is that the sampling rate is lowered, thus reducing the data quality. From the 21 October 2010 staggering was introduced to the Irene radar for the lower scan angles and by 6 November 2010 for the Ermelo radar. The ratios were adjusted a few times over the 10-year data period for the lower elevation scans (Appendix 1). The maximum range that the higher elevation scans operated at were also adjusted to accommodate a higher Nyquist velocity rather than using staggering, although staggering was used for all levels from September 2011 until 13 January 2013. The PRF ranged between values as low as 375 Hz up to 750 Hz, while the upper-level scans contained a fixed PRF of either 1000 or 1200 Hz (Appendix 1).

It is important to note the changes in the scan strategy and thus the changes in the Nyquist velocity when analysing the radial velocity. A low Nyquist velocity will result in certain features becoming more difficult to interpret as winds may easily exceed this speed in the atmosphere, resulting in velocity folding (Joe and May, 2003). Velocity folding occurs when the phase shift, due to the moving target, is more than ± 180° from the transmitted phase (Rinehart, 2010). In most cases it can quite easily be recognised and will appear as an abrupt discontinuity in the velocity field with areas of strong velocities that move towards and away from the radar right next to each other (Rinehart, 2010). There are cases where folding is not as easily recognised, for example when an entire isolated thunderstorm results in velocity folding or in the case of C-band or X-band radars that have very small Nyquist velocities and thus velocity folding may occur more than once.

The changes to the Nyquist velocity for both the Ermelo and Irene radar are shown in Appendix 1. According to the metadata the Nyquist velocity for the Ermelo radar was significantly lower than for the Irene radar from October 2013 (as low as ± 12.5 ms^{-1}). However, when calculating the Nyquist velocity, based on the given PRF and radar wavelength, the values should be higher. For example, on 27 November 2013, the 7.9° scan has a PRF of 1000 Hz and with a wavelength of

10.56 cm, the Nyquist velocity should be ± 26.4 ms^{-1}. However, the metadata provided a Nyquist velocity of only ± 12 ms^{-1}. A visual inspection was conducted on this case day and the 7.9° scan showed areas of velocity folding occurring with values near ± 12 ms^{-1} (not exceeding this). Thus, the Nyquist velocity values provided in the metadata are correct and the provided PRF values appear to be incorrect.

Both radars in general had poor quality Doppler velocity data prior to 6 November 2010, with folding happening regularly due to the low Nyquist velocity. Thus, velocity data was not used to identify supercells during that period, likely resulting in several supercells, that did not contain the classic reflectivity features, being missed. In addition, from October 2013 onwards, velocity folding potentially had an impact on the identification of some supercells on the Ermelo radar, due to the low Nyquist velocity (between ± 12.5 to ± 18.75 ms^{-1}) (Appendix 1). It must be noted that events were still identified on this radar using the velocity field from October 2013 onwards.

3.3.2.2 Spatial resolution

Various factors influence the resolution of the radar, which in turn impact the identification of small-scale features. The energy returned to the radar from the atmosphere is determined by the radar sample volume (Rauber and Nesbitt, 2018; Rinehart, 2010). The sample volume takes on a conical shape and is determined by the range from radar, pulse length, and antenna beamwidth. The Irene and Ermelo radar predominantly had a pulse width of 1.67 µs resulting in a pulse length of 500 m (Table 3-1). Some slight changes to the pulse width were observed during 2010. Since the energy that is received back at the radar relates to particles at the front and back of the transmitted pulse the contributing radial dimension of the sample volume is half the pulse length (Rinehart, 2010). Therefore, 250m for both radars. These volume samples are range averaged to produce a range bin (pixel) resolution of 500 m. The azimuth resolution for each of the bin values are determined by the angle steps and is set to 1° for both radars (Rauber and Nesbitt, 2018). However, since the antenna is moving in azimuth the sample volume will undergo a "smearing" effect resulting in a beamwidth larger than the antenna beamwidth (Brown et al., 2002; Rauber and Nesbitt, 2018). This is known as the effective beamwidth. The effective beamwidth depends on the rotational speed of the antenna, PRF and the time interval between pulses (Brown et al., 2002; Doviak and Zrnic, 1993).

The beam broadening effects with distance and the effective beamwidth together impact the detection of small-scale features. A larger sample volume with distance from the radar, results in the averaging out of small-scale features, since total beam filling is assumed (Becker, 2014; Burgess and

Lemon, 1990; Rinehart, 2010). Both the hook echo and mesocyclone (anticyclone) may be impacted as these small-scale features may be lost (Burgess and Lemon, 1990; Donaldson, 1970). In the case of the mesocyclone rotational signature, for example, the radius should not be smaller than the sample volume in order for it to be detected (Burgess and Lemon, 1990; Doviak and Zrnic, 1993). Donaldson (1970) suggested that the diameter of the rotational signature on radar should be between 1.5 times the antenna beamwidth (1.5° for most modern weather radars) and half a radian (≈ 29°) for it to be recognised on radar. If the sample volume, which increases with distance from the radar, becomes larger than the radius of the rotational signature, radar analysis will become difficult (Burgess and Lemon, 1990). However, radars operating with an antenna beamwidth of 1° are not often impacted within a 200 km range. For this reason, Burgess and Lemon (1990) and Donaldson (1970), suggested confining the range to less than 200 km to be able to confidently identify a supercell. This was the first reason why only data up to a range of 200 km was considered in this research.

Despite using a maximum 200 km radial range for each radar, the supercell features were still significantly impacted with distance from the radar. A good example of this is shown in Figure 3-5 for

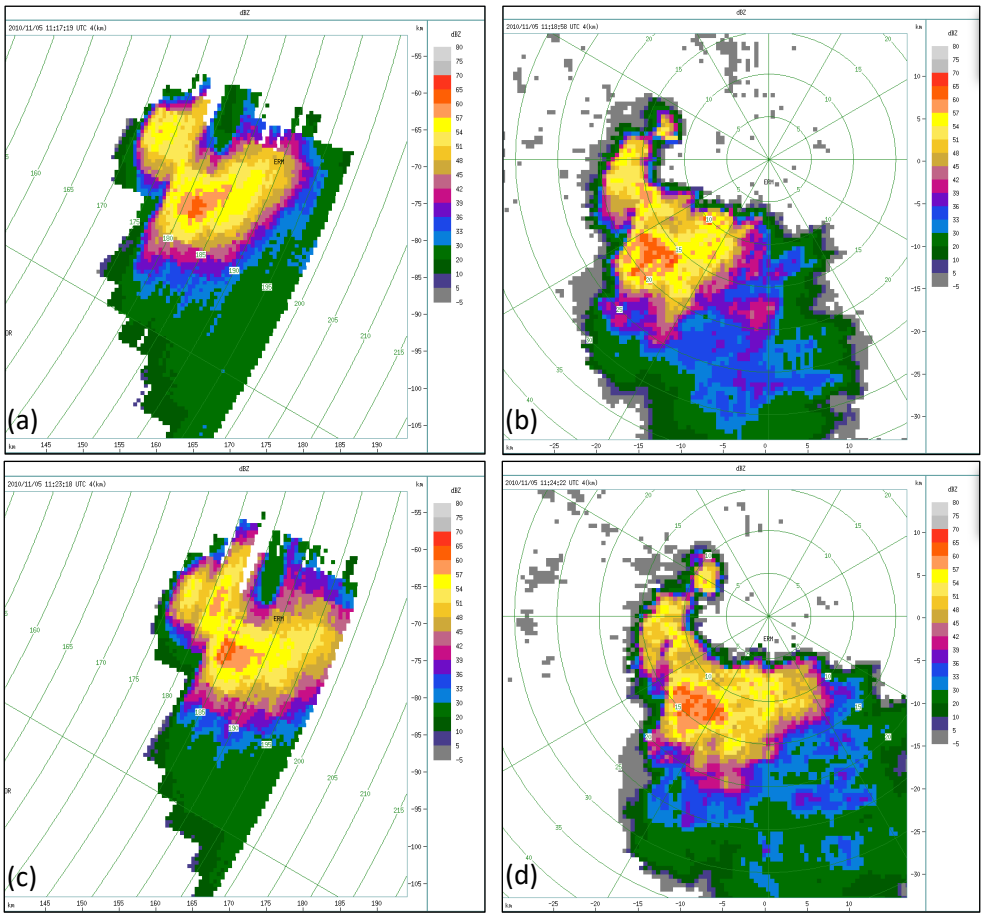

Figure 3-5: Reflectivity field (dBZ) on 5 November 2010, showing the hook echo of a left-moving supercell at the 4 km CAPPI level for the Irene radar at (a) 11:17:19 UTC and (c) 11:23:18 UTC and for the Ermelo radar at (b) 11:18:59 UTC and (d) 11:24:22 UTC.

a supercell thunderstorm that was identified on 5 November 2010. This supercell was found to occur 170 to 200 km from the Irene radar but was located within 20 km of the Ermelo radar. The 4 km CAPPI level is shown for each radar showing the hook echo of the supercell at almost the same time (approximately 1 minute apart). The shape of the hook echo is much broader and lacks the classic shape on the Irene radar compared to the Ermelo radar and may have been missed if only the Irene radar had been available on this day. Unfortunately, this may have occurred on various occasions due to the poor availability of the Ermelo radar (section 3.3.1).

3.3.2.3 Beam elevation with distance

As a result of the curvature of the earth and beam propagation through the atmosphere, the radar beam will increase in height with distance from the radar (Rauber and Nesbitt, 2018; Rinehart, 2010). Atmospheric conditions, such as changes in vertical temperature or humidity gradients (e.g., inversions), will impact beam propagation. Under conditions of standard refraction, the radar beam will bend downwards, but will not follow the curvature of the earth, thus it will be higher up in the atmosphere with distance from the radar (Rauber and Nesbitt, 2018; Rinehart, 2010).

If we assume the earth's radius is approximately 6374 km at a latitude of 26°S, then the height of a 0.5° scan at a distance of 200 km from the radar will be approximately 2.38 km above the radar, which is 3.9 km AMSL for the Irene radar and 4.2 km AMSL for the Ermelo radar. This may pose a problem with the detection of low-level supercell features since the lower part of the thunderstorm will not be detected at this distance from the radar. This was the second reason data was only analysed to a maximum range of 200 km in this dissertation. Even at distances of 150 km the height of the 0.5° scan would be approximately 1.3 km above the radar, thus potentially impacting the detection of low-level features at any distance from 150 km up to 200 km from the radar.

3.4 The LROSE software and TITAN algorithm

LROSE, in which the TITAN algorithm is managed, was used to conduct this research (Dixon and Javornik, 2016; Dixon and Wiener, 1993). The Rview application within LROSE was used to view the data, while TITAN was used to track and analyse the thunderstorms. Operationally, the SAWS converts the data into CAPPI levels, thus in this research it was also used to identify supercell features, along with the cross-section product. The cross-section product built into the Rview application, provides information of the vertical profile of the data over a chosen distance, which is calculated using the CAPPI levels. This was used to analyse the vertical profile of the thunderstorms. A maximum reflectivity product, also available within the Rview application, provides the highest reflectivity value

within a vertical column above a certain point (Milrad, 2017). This product was not used for supercell identification but rather used when manually tracking thunderstorms.

3.4.1 Conversion of data

The multiple volume scans are stored in polar coordinates containing the radar range, elevation and azimuth angle for each scan, which is stored in a Gematronik volume (VOL) file format (Becker, 2014; Rauber and Nesbitt, 2018). In order to view the radar data using the Rview application in LROSE, the data was converted from polar to cartesian coordinates, where data is stored in a Meteorological Data Volume (MDV) file format (Becker, 2014; Dixon and Wiener, 1993). Data is converted into a grid cartesian space with east-west x-coordinates, north-south y-coordinates and vertical z coordinates (Rauber and Nesbitt, 2018). The resulting data used in this research thus contained a grid resolution (longitude and latitude) and a vertical resolution of 0.5 km respectively. However, it is important to note that the impact on the resolution discussed in section 3.3.2.2 holds and thus despite a grid resolution of 0.5 km across the radar coverage area, the detection of small-scale features is still impacted with distance from the radar (e.g., Figure 3-5).

The polar coordinates are interpolated to a horizontal plane at set altitudes (CAPPI levels) (Becker, 2014; Rauber and Nesbitt, 2018). This is done using the data from the individual volume scans (Figure 3-6), where the elevation steps that are used to provide the information are determined by the distance from the radar (Mittermaier and Terblanche, 1997). Thus, for areas closer to the radar, predominantly higher elevation scans are used, and decreases with distance. The conversion of data into a CAPPI display can be classified into two methods, a visual projection and an interpolation method (Mittermaier and Terblanche, 1997). The visual projection method results in very abrupt transitions, where data moves from one elevation to the next, while the interpolation method (applied

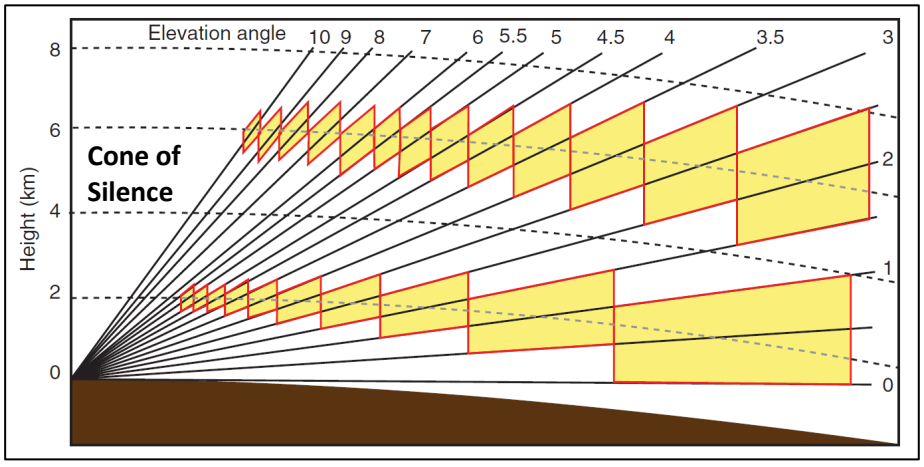

Figure 3-6: Strategy used to create a CAPPI display with the radar's scan angles and the 2km and 6km CAPPI display strategy shown. (Obtained from: Rauber and Nesbitt, 2018).

to the data conversion for this research) results in a smoother transition. As can be seen in Figure 3-6, data is obtained from a slant elevation plane and is projected onto a horizontal plane that is also in line with the surface of the earth (Mittermaier and Terblanche, 1997; Rauber and Nesbitt, 2018). When data is converted, an 8-point linear interpolation grid transformation is used, assigning the 8 nearest data grid points from the polar coordinates to the cartesian grid point. More detail on this interpolation method can be found in Mittermaier and Terblanche (1997) and Rauber and Nesbitt (2018). Data converted in this research used a minimum of 4 points up to a maximum of 8 (as is done operationally at the SAWS), thus at least 4 valid data points out of a possible 8 were required for the interpolation to go ahead.

Each CAPPI display height is calculated to a height in kilometres AMSL and in total 36 levels were created during the conversion process, starting at 2 km AMSL, moving up 0.5 km increments to a maximum of 20 km AMSL. As was discussed in section 3.3.2.3, the radar beam height increases with distance. This results in a limitation on the CAPPI display, as the lower CAPPI levels will have a limit in the range at which they are available. Only CAPPI levels from approximately 4 km AMSL upwards have a range up to 200 km, while those between 2 and 3.5 km AMSL only have a range of approximately 80 km to 180 km. In addition, because of the cone of silence, areas close to the radar are impacted by a loss in data, specifically the higher CAPPI levels, as this area increases in the upper levels (Figure 3-6).

3.4.2 Storm identification and storm tracking algorithm

The TITAN algorithm identifies a thunderstorm based on a contiguous area of reflectivity values that exceed a specified threshold (Dixon and Seed, 2014; Dixon and Wiener, 1993). This threshold is automatically set in the TITAN tracking script at 35 dBZ with a maximum value of 80 dBZ, thus any reflectivities that exceed 35 dBZ are considered, but not those exceeding 80 dBZ. Operationally the SAWS has been using a threshold of only 30 dBZ. This threshold can be adjusted as required. The algorithm is executed using a two-step approach (Dixon and Wiener, 1993). In the first step, neighbouring points in the data grid on the horizontal x-direction (east-west) that exceed the threshold are identified, which is done on all CAPPI levels. Then in the second step these points are analysed to determine where they are found to occur adjacent to each other (in the x- y- and z-direction) and are grouped together therefore classifying as one storm. This results in a 3-dimensional analysis of each thunderstorm. This method is known as the single threshold method.

One disadvantage of the single threshold method is that thunderstorm cells that have an overlap region but do not merge are classified as one thunderstorm (Dixon and Seed, 2014). A dual

threshold method can be implemented to prevent this from happening. In this method a second threshold is set, for example at 40 dBZ, and the maximum reflectivity within a column rather than the CAPPI product is used (i.e., the analysis is done in 2-dimensions). Grid points that exceed this second threshold are identified and small areas are ignored if the following thresholds are not met. Firstly, the sum of all smaller areas (higher threshold) must be greater than 50% of the larger area (lower threshold), then, each smaller area must be greater than 5% of the sum of all the smaller areas together, and lastly, each smaller region must be greater than a set size which is automatically set to 20 km^2. If these thresholds are not met, then the smaller area is discarded. All these thresholds can be adjusted as desired. Once the storm has been identified, various storm analysis calculations can be performed, including the centroid position (Dixon and Wiener, 1993).

The TITAN storm tracking algorithm uses various steps to match thunderstorms identified in one scan to the next scan (Dixon and Seed, 2014; Dixon and Wiener, 1993). Firstly, the distance a storm has travelled is considered, where a shorter rather than a longer distance is favoured in the matching process. Secondly, the shape, properties, size, etc. are considered, with storms of similar characteristics matched together. This tracking algorithm also takes into consideration merging and splitting thunderstorms. More detail on how the algorithm tracks the thunderstorm can be found in Dixon and Seed (2014) and Dixon and Wiener (1993).

3.5 Identification of supercell thunderstorms

The first objective in this research was to identify as many supercells as possible within the radar coverage area. Thus, a clear definition using radar data was established, which is summarised in the decision tree shown in Figure 3-7. The definition developed in this dissertation was in line with those used by other studies (e.g., Bunkers et al., 2006a; Hocker and Basara, 2008; Moller et al., 1994) and discussed in more detail in section 2.3. The database of all the supercell events identified in this research are provided in Appendix 2.

Prior to implementing the decision tree, thunderstorms (for each available day) were analysed on the reflectivity field. If a thunderstorm contained one or more of the following features it was investigated further: high reflectivities, appeared to be persisting, deviated (left or right), contained an inflow notch or some evidence of a possible hook echo, a high reflectivity gradient on the inflow side of the storm, a WER, or a BWER. Most of the pre-analysis was done using either the lower CAPPI

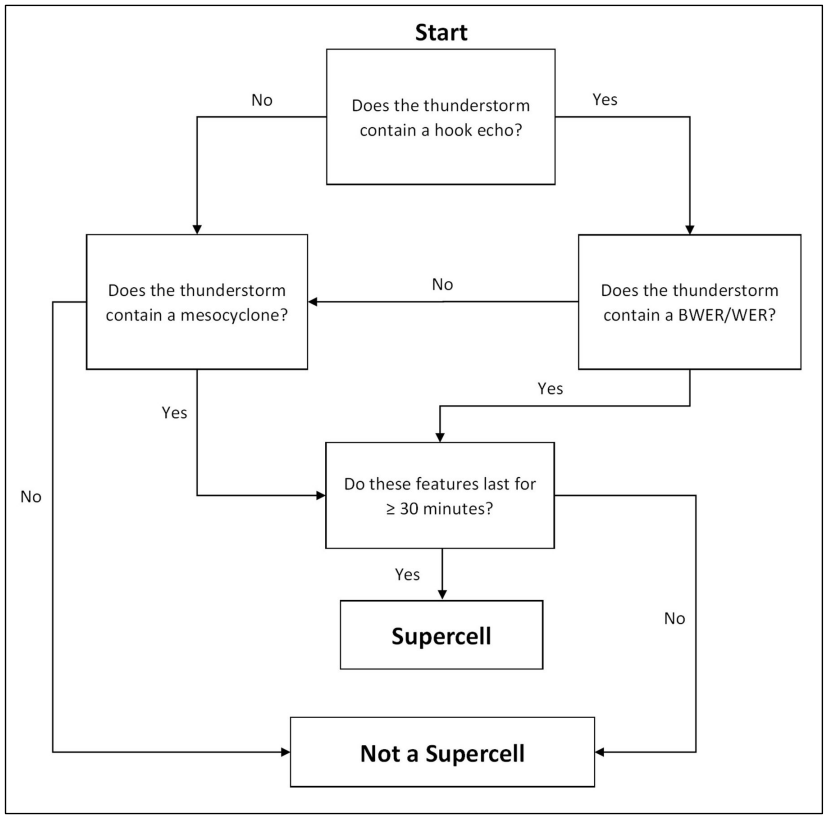

Figure 3-7: The decision tree used to identify supercell thunderstorms over the radar coverage area.

levels or maximum reflectivity product. Once a thunderstorm of interest was identified, the decision tree was implemented using the following steps:

1. The lower CAPPI level (2 to 4 km) was analysed to determine if a hook echo was present. The hook echo could take on any of the possible shapes discussed in section 2.3.1.
2. If a hook echo was identified, a cross-section was taken through the thunderstorm to determine if a BWER or WER was present.
3. If the hook echo and/or BWER/WER were unclear or not identified, then the velocity data was consulted to determine if a mesocyclone (mesoanticyclone) was present. The 3.5 to 10 km CAPPI levels (2 to 8 km AGL) were analysed to identify possible rotation and the rotational feature was required to be between 1 and 10 km in width.
4. The final step was to apply the time criteria. Supercell features were required to last for at least 30 minutes or 5 radar scan time steps.

The mesocyclone (anticyclone) alone was considered sufficient to classify the thunderstorm as a supercell. Both Hocker and Basara (2008) and Antonescu et al. (2010) only used the mesocyclone to identify supercells within their studies. Therefore, the reflectivity features were not a requirement in this dissertation, if a clear mesocyclone (anticyclone) was visible on the velocity field. Despite this, in

all cases where the mesocyclone was clear, the presence of the various reflectivity features or lack thereof were also documented.

Unlike other studies (e.g., Antonescu et al., 2010; Hocker and Basara, 2008), the mesocyclone (anticyclone) was not a requirement if the reflectivity features were well defined, which follows a similar approach taken by Bunkers et al. (2006a). The reason for not requiring this feature was because the rotational couplet on the Doppler velocity field is not always easy to identify, due the limitations on the Nyquist velocity (section 3.3.2.1), issues with distance from the radar (section 2.3.3 and 3.3.2.2), beam elevation with distance from the radar (section 3.3.2.3) and various circulation and flow patterns associated with or surrounding the mesocyclone (section 2.3.3). It must be noted that in some cases the hook echo on the reflectivity field may not have been clear (due to similar limitations), and so, if no mesocyclone (anticyclone) was detected for the same reasons, a supercell case may have been missed. Despite the mesocyclone (anticyclone) not being a requirement, its presence, or lack thereof, was always noted where reflectivity features were clear. Thus, some supercells that were identified contained all reflectivity and Doppler velocity features.

As a result of the cone of silence data in the mid- and upper-levels was not available directly above the radar. This made the identification of the BWER/WER and mid-level mesocyclone more difficult, whereas the hook echo (if present) was usually still visible. Thus, this was considered when implementing the decision tree and if a supercell was identified prior to moving over the radar and again once it moved away from the radar it was assumed that the storm maintained these characteristics throughout. In most cases, this only impacted one or two scans.

The time criteria of 30 minutes was in line with other studies done (e.g., Antonescu et al., 2010; Bunkers et al., 2006a; Burke and Schultz, 2004; Hocker and Basara, 2008; Moller et al., 1994). Since the radar has a temporal resolution of approximately 6 minutes, the supercell features had to persist for at least 5 radar scan time steps. In some cases, the temporal scan resolution was just under 6 minutes and thus the total time was around 29 minutes, but these cases were still included. For each scan, a different path of the decision tree (Figure 3-7) was possible, in other words it may have had the reflectivity features on one scan and then only the mesocyclone on the next.

As mentioned in section 2.3, thunderstorm deviation is not always observed in supercells and thus this was not a requirement in this dissertation. However, deviation was still considered when analysing the radar data to assist in the identification of a supercell. The deviation of a supercell predominantly occurs to the left of flow in this region with a mesocyclonic rotation, although right-

movers, with mesoanticyclonic rotation, are also possible and were thus included in this study. Each storm was classified as either a left- or right-mover based on if it contained a mesocyclone or mesoanticyclone respectively or contained the required reflectivity features on the left or right flank of the thunderstorm respectively.

As was done in the study by Bunkers et al. (2006a) cyclic supercells were taken into consideration, in this research, where possible, and were considered as one supercell. Thus, even if supercell features were lost, but regained them again shortly afterwards, possibly showing another decay and regeneration of the mesocyclone at a later stage and so on, the storm was considered as one supercell. However, if a supercell thunderstorm experienced a merger with another thunderstorm or lost its supercell features, showed no immediate signs of updraft re-generation, but then re-developed supercell features again at a much later stage, the supercell was labelled as a new supercell event.

Each supercell was labelled chronologically using the following format: SCyymmdd##. The SC stands for supercell, followed by the date of the occurrence (year (yy), month (mm) and day (dd)), and then numbered in order of appearance on that day (##). For example, SC14101001, was the first supercell that appeared on the 14 October 2010. In the case where a supercell experienced a merger or for some other reason lost its features but regained them again at a later stage (not a cyclic supercell), the supercell was classified as a new event but the label was linked to the previous event (e.g., SC14101001.2).

It is also important to note that the identification of supercells was heavily based on the reflectivity field as it was usually one of the first fields viewed when analysing the thunderstorms. Due to the large number of days that needed to be investigated between both radars, not all thunderstorms were analysed on the Doppler velocity field, and thunderstorms were only further investigated if it showed signs of severity (e.g., high reflectivity, WER/BWER etc.) or characteristics that may indicate a supercell thunderstorm (e.g., long-lived, deviated, inflow notch etc.). For this reason, some events may have been missed. This adds to those events that may have been missed due to the limitation on the radar data, discussed in section 3.3. Once again, the aim in this research was not to identify all events but as many events as possible given all the limitations.

Not all right-moving supercells were necessarily captured in this study. The focus was naturally towards the easier to identify and more likely to occur (Southern Hemisphere) left-moving supercells. Deviation to the right of the mean environmental winds and an indication of a hook echo, inflow notch or strong reflectivity gradient on the right flank was usually the main reason such thunderstorms were

investigated further on the Doppler velocity field. An observation made by the author during the analysis of possible right-moving supercells, was that the hook echo was often not well defined despite deviation occurring and a mesoanticyclone on the Doppler velocity field. Thus, any right-moving supercell that contained an ill-defined hook echo signature and did not have a mesoanticyclone, due to the limitations on the Doppler velocity field (previously discussed), may have been missed.

3.6 Supercell characteristics

To analyse the temporal, spatial, lifecycle, and track characteristics of all supercells identified within the radar coverage area, the following information was documented and analysed for each individual event or event day (containing at least 1 supercell event):

1. The season and month of occurrence.
2. The location and time of supercell initiation and demise.
3. The lifespan.
4. The track taken, from which the spatial distribution, direction of movement, length of track and speed was calculated and analysed.

The first radar scan where a thunderstorm exhibited supercell characteristics, defined in section 3.5, was used to place the initiation location and time. The last radar scan where a thunderstorm displayed the supercell features, was considered the time and location of the supercell demise. It is important to note that the actual thunderstorm from which a supercell developed may have lasted for a much longer period and that it was not the initiation or demise of the thunderstorm itself. In addition, the initiation/demise location and time may not have been the exact time and location that a supercell developed or decayed as this could have occurred at any time within the 6-minute period prior to the first scan or after the last scan, where supercell features were identified. If data was missing for more than 1 scan time step prior to initiation or after the demise (i.e., more than 12 minutes elapsed between the available scans) the location and time of either the initiation or demise of the supercell was marked as “unknown”. Lastly if supercells initiation or demise occurred at the edge of the radar, with the possibility that it moved out of the radar’s 200 km range, then the initiation/demise was also noted as “unknown”. However, this never occurred as discussed in section 4.1.

The centroid position of the supercell thunderstorm for each time step was used to document the track of the supercell thunderstorm as well as the initiation and demise location. A hybrid approach was used to obtain the centroid position of the supercell thunderstorms, to ensure the

approximate centroid of the supercell was being tracked and not overlapping storms. Either the TITAN algorithm was used, or their position was manually obtained. For the TITAN algorithm, either the single or the dual-threshold was used depending on the case. For some cases the single-threshold worked better to isolate the supercell from other surrounding thunderstorms and in those cases a reflectivity threshold of 45 dBZ was used. A higher reflectivity was chosen since supercells tend to exhibit a higher reflectivity value (as it is a severe thunderstorm).

In most cases, the dual threshold method of identification was used. The dual-threshold criteria were discussed in section 3.4.2. As a base, the lowest threshold was set to 45 dBZ, while the second threshold was set to 50 dBZ. For the remaining thresholds, the smaller areas (containing the > 50 dBZ echo) had to be more than 20% of the larger area (containing the > 45 dBZ echo), each smaller area had to be more than 5% of the sum of all the smaller areas within the thunderstorm, and each smaller area had to exceed an area of 10 km^2. Where supercells were not adequately tracked using these settings, the settings were adjusted (e.g., the reflectivity, area criteria etc.) until the adequate tracking was achieved. For each case the setting that was used was documented. It is important to note that the settings were adjusted to optimise the tracking of supercells and are thus not necessarily useful to determine other radar derived storm properties (e.g., maximum reflectivity, size of the thunderstorm etc.). The tracking number (in some case numbers) for each supercell event was documented. The track data was then extracted using the Tracks2ascii script and written into a text file, from where the tracks were obtained using the documented tracking number(s). The volumetric centroid position in latitude and longitude was extracted for each relevant time step.

For certain time steps, the TITAN algorithm track of the supercell was not optimal (despite adjustments made). This included situations where the track included another (other) thunderstorm echo(es) or the centroid position moved backwards from one scan to the next, due to thunderstorm mergers or splits. In these situations, manual extraction of the centroid position was performed and documented. This was based on the maximum reflectivity product and an approximate centroid position was taken using Rview. This was added to the relevant supercell case for the relevant time step.

In all cases the radar that was located closest to the supercell was used to identify the initiation/demise and track locations. Both radars were consulted to analyse the thunderstorm and identify the supercell features. Except for 1 case, all other cases were tracked using 1 radar (closest radar). On 19 January 2019, both Irene and Ermelo radar were analysed despite Irene being closer to the supercell. Due to several missing time steps in the Irene radar data, Ermelo was also used to

analyse the track taken for this event. A merged mosaic product could have been used but due to the missing data from Irene radar the decision was taken not to create this product.

On 5 November 2010, the Irene radar data experienced a technical issue from 12:17 UTC until 13:05 UTC. The issue occurred with the conversion of the data and was not present when viewing the original volumetric files on the Rainbow®5 software suite. Thus, the centroid position of the supercells that occurred during this time, were manually extracted using the Rainbow®5 software.

QGIS (Quantum Geographic Information System) was used to display and analyse the initiation, track, and demise for all supercells. The latitude and longitude centroid position at each time step of a given supercell, was converted into a vector line to determine the track. The direction of travel for each event was also displayed using an arrowhead. The QGIS length function was used to calculate the distance covered by each supercell event and was based on the entire track taken (i.e., each segment was included).

The bearing for each supercell event was calculated using the latitude and longitude position of the initiation and demise location of all events, including those events with unknown initiation and/or demise locations where the first/last available point was used. Since the bearing provided the direction supercells were moving the values were converted to represent the direction from which they were travelling. A rose diagram was created using 16 bins (each containing an interval of 22.5°) depicting the movement of all supercells and the number of events travelling from a given direction within a specific month.

The spatial distribution of all the left-moving (not right-moving) supercell tracks was analysed using the Kernel Density Estimation (KDE) function in QGIS. A similar approach to that used by Hocker and Basara (2008) was adopted, although some adjustments were made due to the much smaller dataset available. Supercell tracks were not buffered to incorporate their swath thus it was based purely on their vector path, which in turn is based on the centroid position, and not their area of influence. Since characteristics of supercells is still largely unknown within this region, an appropriate value to account for the variation in the size of events is not known. A grid of 1 km by 1 km was created over the data area containing the supercell tracks, which was a slightly smaller grid than that used by Hocker and Basara (2008). This was then used to count the number of lines that occurred within a 10 km search radius from each 1 km by 1 km grid cell. The entire line was used not the individual segments (between each centroid position). A KDE analysis of the initiation and demise locations was not performed due to the low number of events within the dataset.

The length of time each supercell lasted was documented and each event was classified as either a short-lived (≤2 hours), moderate-lived (> 2 hours but < 4 hours) or long-lived (≥ 4 hours) event based on the classification used by Bunkers et al. (2006a). The average speed for each supercell event was also calculated using the track distance (calculated using QGIS) as well as the duration of each event.

3.7 Summary

Radar data from the Irene and Ermelo Doppler radars was obtained from the SAWS and used to identify the supercells in this research. Only supercells that occurred within the warm season, defined as September to February, were included in this research. The entire 200 km radial range of each radar was investigated and this area includes most of the Gauteng and Mpumalanga provinces. A short overview of the topography and the climatological circulation patterns during the warm season were provided in this chapter. Details regarding the radar data used was also provided. Some of the biggest limitations noted in the data was the data availability, resolution of the data, height of the radar beam and the Nyquist velocity all of which may have had an impact on the detection of events.

The LROSE software and TITAN algorithm was used to identify and track the supercell thunderstorms. The CAPPI levels and cross-sections were analysed to identify supercell features. In this research a thunderstorm was classified as a supercell if it contained a clearly defined hook echo and WER or BWER on the reflectivity field. If the hook echo was not clearly defined, a mesocyclone (mesoanticyclone) had to be visible on the Doppler velocity field for it to be classified as a supercell. These radar features (either on the reflectivity field, Doppler velocity field or both) also had to persist for at least 30 minutes (5 radar scans). Each supercell was classified as either a left-mover or right-mover. The initiation of a supercell was defined as the first radar scan with supercell features, while the demise was set as the last radar scan with supercell features. The season and month that each event occurred in was documented as well as the location and time of initiation and demise, track taken and lifespan. The direction of each supercell track was calculated and QGIS was used to analyse the spatial distribution of the supercells and calculate the track length.

Chapter 4: Supercell Database

This chapter provides an analysis of the supercell database that was created using all available radar data for the 10 warm seasons (2010 to 2020). This database is based on the supercell definition developed for this research (section 3.5). The chapter starts by looking at the supercell events and event days that were identified (section 4.1), followed by their seasonal (section 4.2) and monthly (section 4.3) distributions. The monthly and seasonal distributions were based on the database established.

4.1 Supercell event days and events

In total 67 supercell event days (with at least 1 supercell event) were identified, comprising 115 left-moving and 6 right-moving events. All supercell tracks are shown in Figure 4-1 and Appendix 2 provides detailed information of all these events. The closest radar was used to identify each event (section 3.6), thus in total 66 events were identified on the Irene radar and 55 on the Ermelo radar. Only on 3 event days (5 November 2010, 10 November 2016, and 9 November 2019) were supercell events identified on both the Irene and Ermelo radar. Taking into consideration that not all right-movers were necessarily identified (section 3.5), as anticipated for the Southern Hemisphere, there

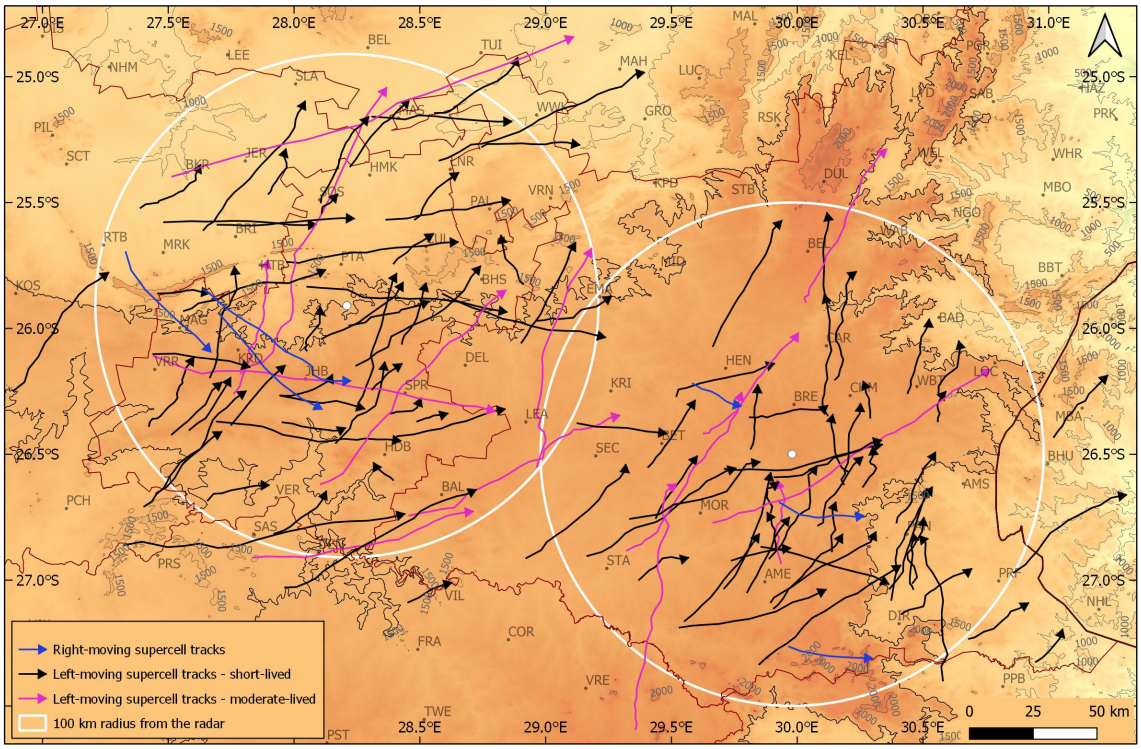

Figure 4-1: All right-moving (blue arrow), short-lived (lasting ≤ 2 hour) left-moving (black arrows) and moderate-lived left-moving (pink arrows) supercells identified within the study period. Each radar's 100 km range ring (white circle) is shown, with the white dot indicating the location of the radar.

were still significantly more left-movers than right movers in the radar coverage area. Due to the low sample of right-movers, some statistics and analysis on these events were not included or discussed in detail in this dissertation.

There were only 6 occasions where supercell outbreaks occurred over 2 consecutive days over the radar coverage area (Appendix 2). All occurred in either October, November, or December. Of the 115 left-mover events only 5 instances occurred where supercell features were lost and then regained again at a later stage (Appendix 2). No such instance occurred with the right-movers. In all 5 instances, the time between the demise of supercell features and redevelopment again was over 30 minutes (Appendix 2), and often occurred due to a merger or interaction with other thunderstorms.

On average 1.8 events occurred per supercell event day with a maximum of 7 events (all left-movers) occurring on 28 November 2013, although one supercell lost its features and then regained it again and thus was classified as two separate events. This event day was known for its significant damage, due to large hail that occurred across Gauteng, resulting in costly losses to insurance companies (Dyson et al., 2021). The 5th of November 2010 and 16th of November 2015 were also noticeable event days with 6 individual events occurring on each day (all left-movers), of which the latter also resulted in significant damage over Gauteng (SAWS, 2015). The rest either contained 1, 2 or 3 events (Appendix 2) of which only 12 days contained 3 supercells, 14 days 2 supercells and the remaining 38 days contained 1 supercell. Only on one day did 2 right-mover events occur (19 October 2011), otherwise only 1 event occurred per supercell event day. All right-movers identified, occurred on a day where either 1 or 2 left-moving supercells were also identified (Appendix 2)

Of the 115 left-moving events considered 3 had an unknown initiation location/time and 2 an unknown demise location/time (Appendix 2) due to gaps in the data availability exceeding 12 minutes (section 3.6). These 4 supercells were thus removed from the statistics relating to the lifespan, tracked distance, initiation, and demise times.

Most of the cases identified occurred within the 100 km radial range of each radar (Figure 4-1). Most of the supercells that had their initiation or demise location outside of this 100 km range, were found to travel within this range at some stage in their lifecycle, and could therefore be identified, as the limitations on the resolution and height of the radar beam (section 3.3.2.2 and 3.3.2.3) played less of a role on the identification of the supercell features. The likelihood that events were missed, that occurred outside of this 100 km radial range is very high. All events that developed or decayed outside of this range were closely examined, to ensure confidence in the location and time of supercell

initiation and demise. No supercell events were found to develop or lose supercell features beyond the 150 km radial range from the radar. The limitations of identifying supercell features at a distance from the radar (section 3.3.2) was likely a major contributor for supercell identification beyond the 100 km range. For this reason, the 100 km range ring was provided on most images depicting the supercell distribution, track, initiation, or demise discussed in chapter 4, since information beyond 100 km was less reliable.

4.2 Seasonal distribution

The seasonal distribution of all identified supercells in the database (left-moving and right-moving) is shown in Figure 4-2. The data availability was very low for both radars during 2012-2013 (section 3.3.1), thus no supercell events were identified during this period (indicated by * on Figure 4-2). For this reason, the study period going forward only consisted of 9 rather than 10 seasons and all statistics excluded this season. The Ermelo radar's availability for the first 5 seasons was also severely impacted (Figure 3-4) and no supercells were identified during 2011-2012 and 2014-2015 (* on Figure 4-2), since either very limited or no data was available for these seasons.

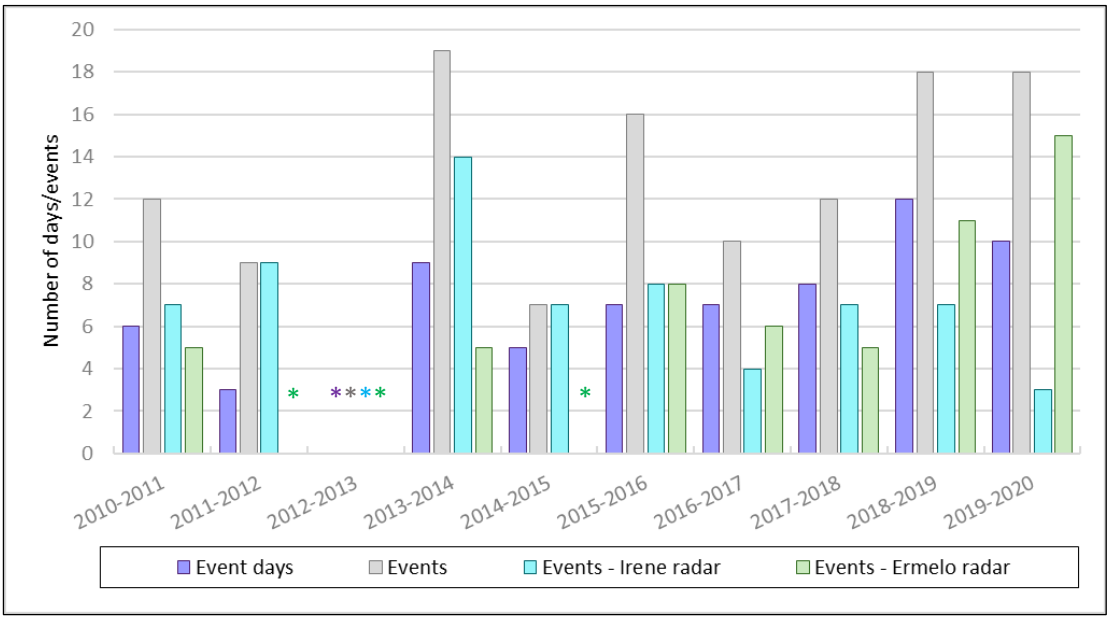

Figure 4-2: The seasonal distribution for all supercells identified within the warm seasons of 2010 to 2020. The * indicates where data availability was limited or not available as shown in Figure 3-4.

The highest number of events occurred during 2013-2014 (Figure 4-2), with a total of 19 left-movers, which was also the peak in the number of supercell events for the Irene radar coverage area (14 events). The biggest contributor to these events was 28 November 2013, where 7 events occurred. The peak in number of events for the Ermelo radar occurred in 2019-2020 (13 left-movers and 2 right-movers), which was also the lowest number of events for the Irene radar. The highest number of event

days occurred during 2018-2019, with a total of 12 days. The second highest was 2013-2014, which could have had more event days (and overall events) considering the Ermelo radar availability was 60%, although the availability during 2018-2019 was also low at 65%.

When considering the last 5 seasons only, as data availability was higher for both radars (section 3.3.1), the most active season for supercell events was both 2018-2019 and 2019-2020 (18 events respectively), during which more events were identified on the Ermelo radar than the Irene radar. The least active supercell season was 2016-2017 (7 event days and 10 events) and all events occurred between September and November (Appendix 2). The 2015-2016 season was also a noticeable year with a significant number of events (16), although event days were low (7 event days). On 3 event days multiple events occurred, including the 6 events that occurred on the 16 November 2015.

The total average supercell event days and events was 7.4 and 13.4 per season respectively (Figure 4-3). The average values for the first 5 seasons were 5.8 event days and 11.8 events, while the average for the last 5 seasons was 8.8 and 14.8 respectively (Figure 4-3). The Irene radar had an average of 7.3 events per season, with an average of 9.3 during the first half of the study period, decreasing to 5.8 during the second half (Figure 4-3). The Ermelo radar had a higher average of 9 events in the last 5 seasons compared to Irene, with only 1 season (2017-2018) containing less events (Figure 4-2). For the Ermelo radar the average for the first 5 seasons (* on Figure 4-3) was not representative due to the low availability.

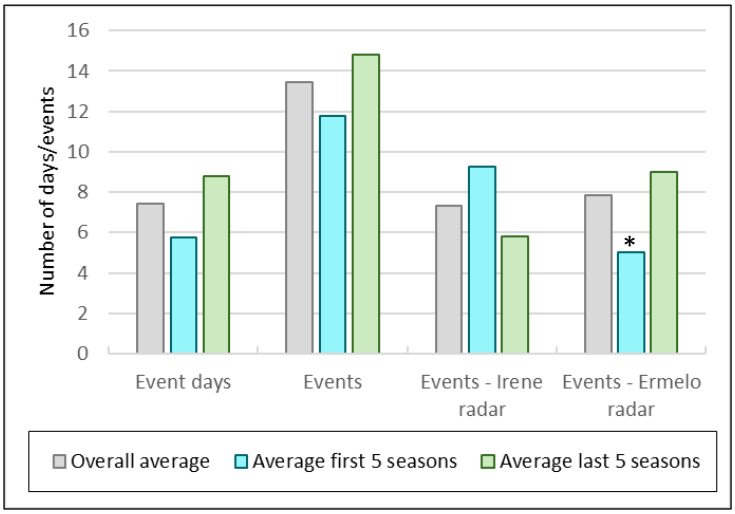

Figure 4-3: A bar graph showing the averages for the supercell event days, events, events identified on the Irene radar and events identified on the Ermelo radar. The total average for all seasons (excluding 2012-2013), the average for the first 5 seasons and for the last 5 seasons are shown. The * shows the average for this period may not be representative as it was only based on 2 seasons.

4.3 Monthly distribution

The supercell event days and events were grouped into the first and second half of each month (Figure 4-4). Supercell event days and events showed an increase during spring (September to November), peaking in either October or November and then decreasing through the later summer months. The spring season contained approximately 60% of the event days and 68% of the events. A peak in the number of event days occurred during the second half of October, although the total number of event days in October and November were the same (18 days). The peak in the number of events occurred 3 to 4 weeks later, during the second half of November, although the second half of October saw a secondary peak. All mass outbreak event days, with either 6 or 7 events, were experienced in November and contributed significantly to the higher number of events observed during this month. The number of event days and number of events decreased during the first half of December but then increased again during the second half of December, before dropping significantly again in January and into February (Figure 4-4).

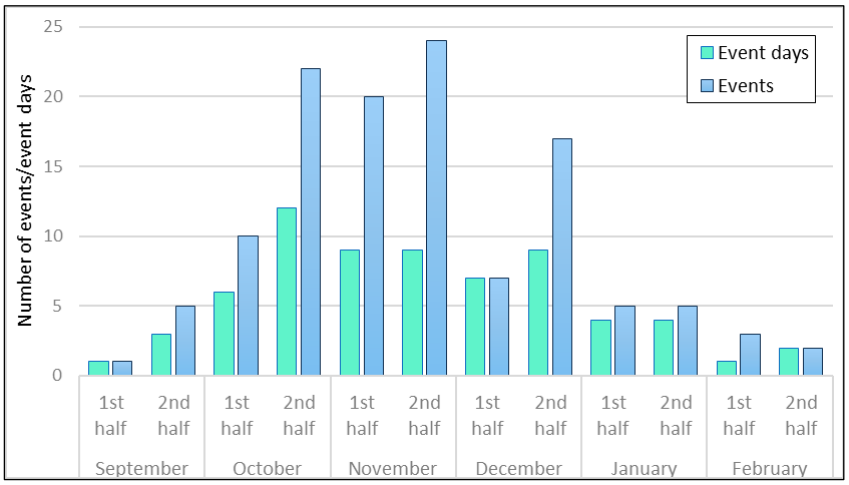

Figure 4-4: The bi-monthly (1st half and 2nd half) distribution for the number of supercell event days and supercell events identified within the warm seasons (2010 to 2020).

The bi-monthly distribution for the event days and events identified on the Irene and Ermelo radar was also analysed (Figure 4-5). As discussed in section 4.1, supercells were identified on both radars during 3 event days, which was taken into consideration when calculating the monthly distribution of the event days for each radar. Since all supercells were identified within 150 km for each radar (most within 100 km), Figure 4-5 (a) shows supercell events days and events that predominantly occurred over Gauteng, while Figure 4-5 (b) shows those that predominantly occurred over Mpumalanga.

The overall distribution of the supercell event days and events over Gauteng and Mpumalanga (Figure 4-5) contained a similar pattern to that shown on Figure 4-4 but some noticeable differences

(a) Irene radar

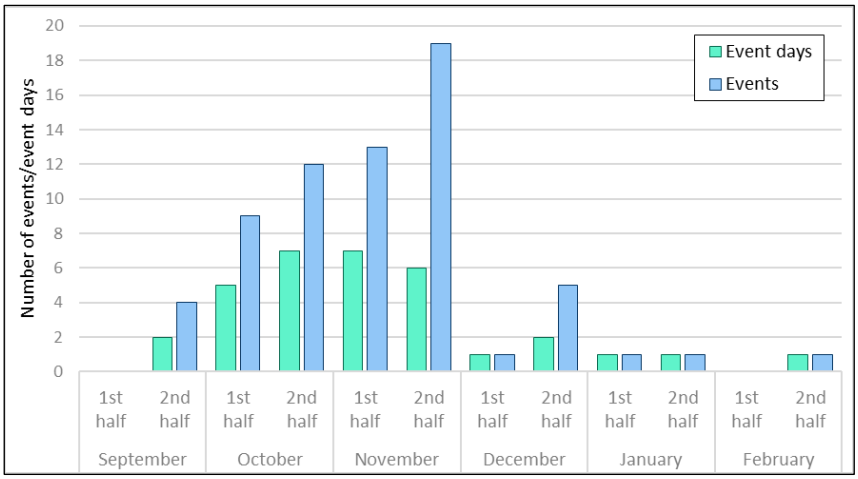

(b) Ermelo radar

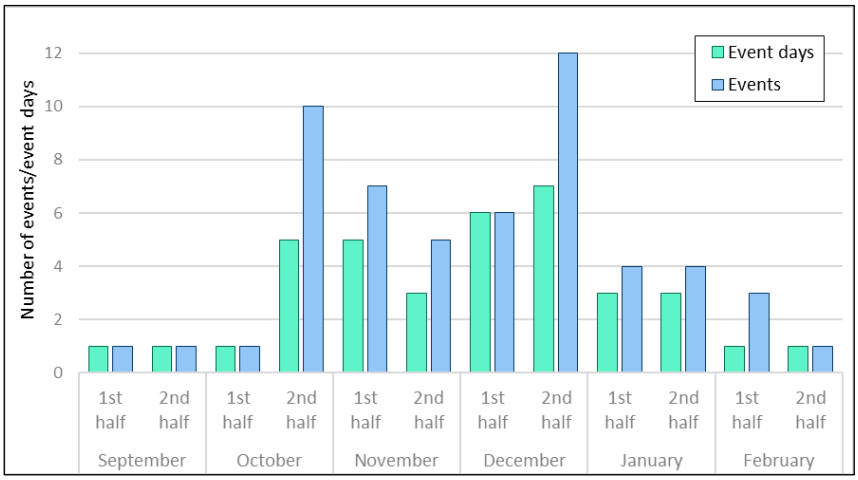

Figure 4-5: The bi-monthly (1st half and 2nd half) distribution for the number of supercell event days and supercell events identified within the warm seasons (2010 to 2020) on the (a) Irene radar (predominantly over Gauteng) and (b) Ermelo radar (predominantly over Mpumalanga).

were observed. Over Gauteng the peak in event days still occurred during the second half of October but also included the first half of November, with November containing the overall peak. The peak in events still occurred during the second half of November (Figure 4-5 (a)). The increase during the second half of December was much less pronounced compared to Figure 4-4. In contrast to this, the distribution over Mpumalanga showed to have the peak in both event days and events during the second half of December, with a secondary peak during the second half of October (Figure 4-5 (b)). Activity was also shown to be greater during January and February compared to the Gauteng region, which showed to have higher activity during the earlier part of the season (predominantly in spring).

4.4 Summary

A database of 115 left-moving and 6 right-moving events was established, over 67 event days. All right-moving events occurred on a day with at least 1 left-moving event. An average of almost 2

events were found to occur on a given event day with a maximum of 7 events on a given day. Almost all cases were identified within a 100 km radial range from each radar with none found to occur beyond 150 km. This indicates that distance from the radar was a significant limitation on supercell identification for this region.

The seasonal distribution based on the given dataset showed variations in supercell activity, with a peak in events in 2013-2014 and a peak in events days in 2018-2019. The 2016-2017 season saw the lowest frequency of events and event days in the last 5 seasons where availability was good. On average approximately 7 events and 13 event days occurred per season but this average was higher at approximately 9 events and 15 event days per season for the last 5 seasons. Gauteng saw a declining trend in supercell frequency across the 10-year period, while Mpumalanga had more events compared to Gauteng in the last 5 seasons.

The peak in supercell events days was found to occur during the second half of October while the peak in events occurred 3 to 4 weeks later in November (which also contained the overall peak). The monthly distribution for Gauteng and Mpumalanga revealed a slight shift in the supercell season. Over Gauteng supercells were more active during spring with the peak occurring in November. However, over Mpumalanga, activity only increased from late October with the peak in frequency occurring in December. Activity was also slightly greater in January and February compared to Gauteng.

Chapter 5: Characteristics of supercells

This chapter provides the results for the supercell characteristics determined from the supercell database identified and discussed in chapter 4. The supercell initiation and demise characteristics (section 5.1), lifespan (section 5.2), track distance (section 5.3), average speed (section 5.4), track direction (section 5.5), spatial distribution of the left-moving supercell tracks (section 5.6) and monthly track distribution (section 5.7). The methodology used to determine these characteristics was discussed in section 3.6.

The initiation and demise of supercells were determined for the first and last appearance of supercell features and did not include the initiation or demise of the thunderstorm, which may have persisted for some time prior and after supercell features were observed. Additionally, the track and lifespan were also only based on the period when the thunderstorm exhibited supercell features and not on the entire lifespan/track of the thunderstorm. The statistics relating to the initiation and demise times, lifespan, track distance, and speed excluded the events with an unknown initiation and/or demise location/time. Statistics and analysis for left-moving and right-moving supercells were separated, although due to the low sample of right-moving supercells the statistics are not representative and no significant conclusions can be drawn. Finally, as discussed in chapter 4, the 100 km radial range was included in most figures as this region contained most of the events and was less likely impacted by resolution and other limitations due to distance from the radar.

5.1 Initiation and demise

The diurnal distribution of left-moving supercell's initiation time showed an increase in activity from 9:00 UTC (SAST is UTC +02) onwards, peaking within the hour of 13:00 UTC, then decreasing into the evening and overnight (Figure 5-1). Very few events developed late at night or during the morning with most events developing between 11:00 and 17:00 UTC (88%) (Figure 5-1). The demise of left-moving supercells was found to peak within the hour of 14:00 UTC with most of the events decaying between 12:00 and 18:00 UTC (88%). Therefore, there was a 1-hour shift in time between the peak in supercell initiation and demise times, which corresponds to the average lifespan for left-moving supercells of 1 hour 12 minutes (section 5.2). As with the initiation, very few events decayed overnight and during the morning hours.

There was a noticeable geographical shift from the initiation to demise location of the left-moving supercells, towards the north-east (Figure 5-2). The initiation locations were well scattered around Gauteng (Figure 5-2 (a)), while over Mpumalanga supercell initiation was more active over the

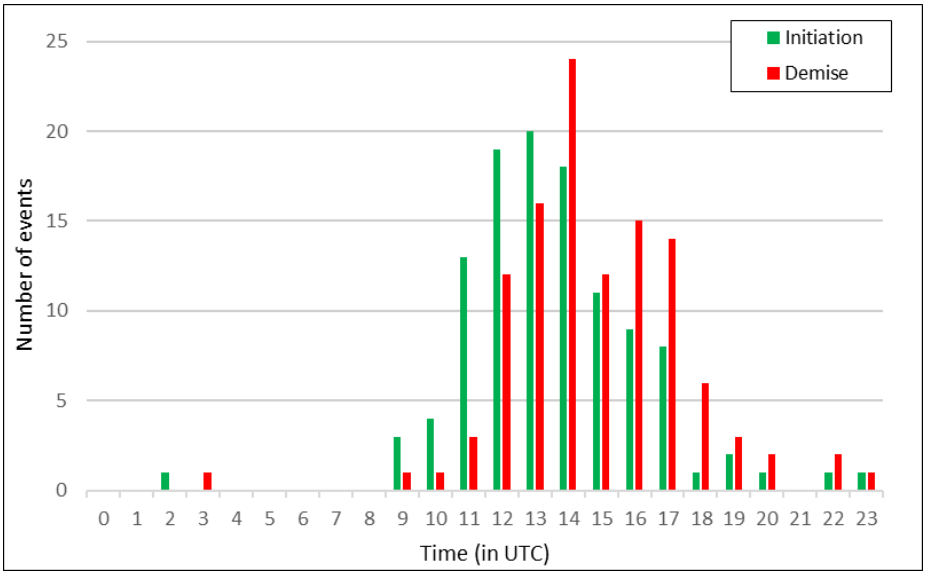

Figure 5-1: The diurnal distribution of left-moving supercell initiation (green) and demise (red) for all events with known initiation and demise times identified within the study period. The times were categorised into hourly intervals.

southern and central parts (Figure 5-2 (b)). Hotspots in supercell initiation activity included the southern parts of Gauteng. There were two instances where 2 supercells developed in almost the same location on separate occasions over the south-western parts (shown by A and B on Figure 5-2 (a)). Over Mpumalanga, hotspots in the initiation location included the southern central and south-east. The spatial distribution of the supercell demise locations (Figure 5-2) also showed areas well spread out throughout the central and northern parts of Gauteng, while over Mpumalanga the demise was more common over the central and north-eastern parts. Hotspots in demise locations included the south-western and north-eastern parts of Gauteng, and areas just to the south and east of the Ermelo radar. Very few supercells were found to develop or decay over the north-western parts of Mpumalanga, within the 100 km radial range of the Ermelo radar, a relatively flat area on the Highveld.

Not all supercell initiation or demise locations corresponded to an area of topography, although most events were found to develop and decay on the Highveld, which dominates much of the radar coverage area. However, some local observations were made. Over the south-western parts of Gauteng, several events were found to develop along a ridge (Ridge 1 on Figure 5-2 (a)), of which all except 1 (which travelled eastwards), were found to decay along a ridge further north (Ridge 2 on Figure 5-2 (a)). A similar pattern can be seen with various events that developed along Ridge 2 that then decayed along the Magaliesberg mountain range (Figure 5-2 (a)), although one was able to move well north of this mountain range. Ridge 1, 2 and the Magaliesberg mountain range are orientated approximately west to east. Over the north-eastern parts of Gauteng and into the north-western parts of Mpumalanga (area marked C on Figure 5-2 (a)) a significant number of supercells were found to decay either along the edge or just north of the Highveld in the lower elevations, thus it is possible

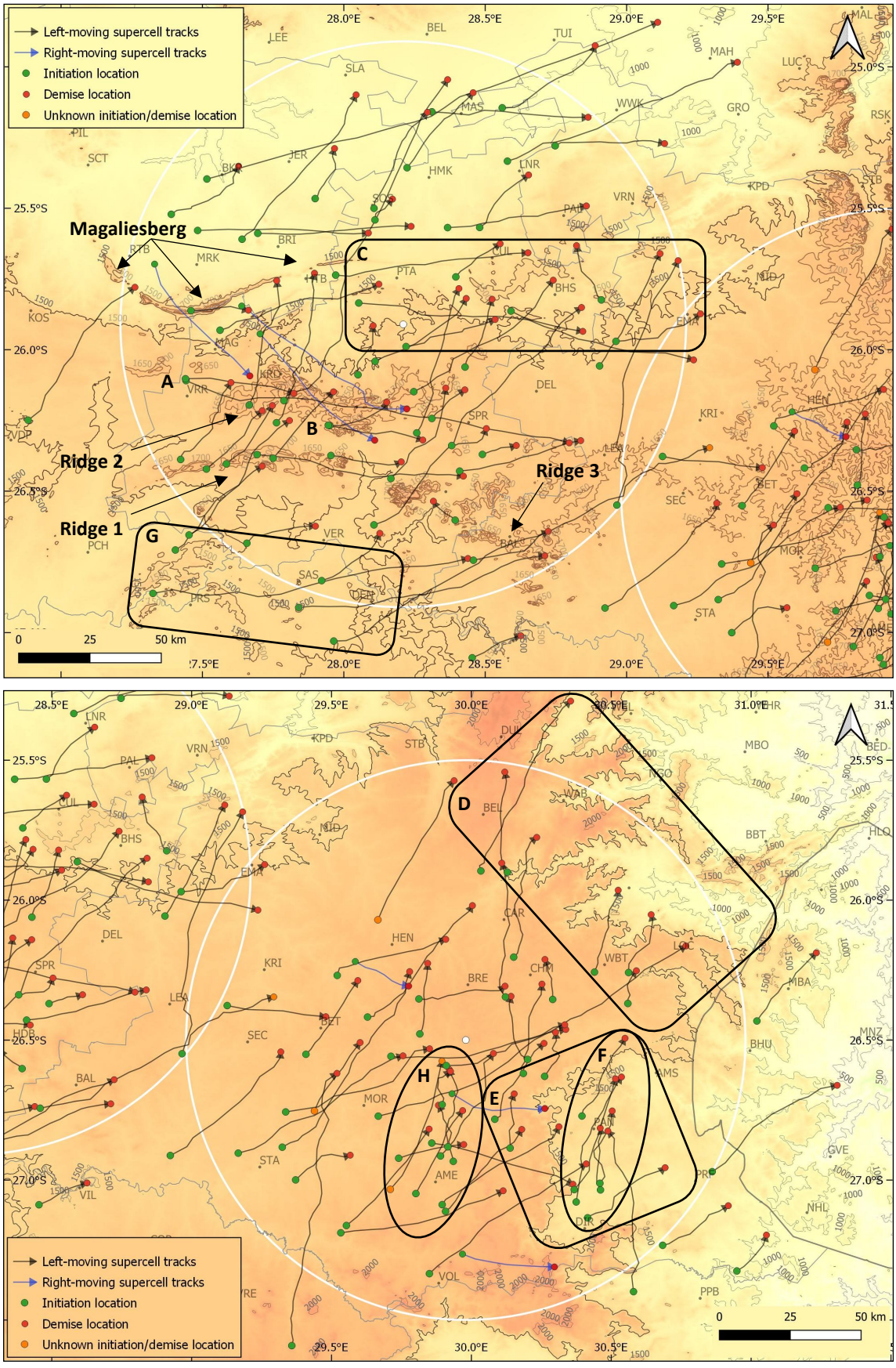

Figure 5-2: The Initiation and demise locations as well as the track of all left-moving (black arrow) and right-moving supercells (blue arrow) over (a) Gauteng (the 1500 to 1800 m AMSL contours in 50 m intervals are also shown) and (b) Mpumalanga (only every 500 m contour shown).

that the topography (downslope flow) influenced the demise of these supercells in this region. A similar observation was made over the north-eastern and south-eastern parts of Mpumalanga (areas D and E on Figure 5-2 (b)).

At least 5 events were confined to the lower lying south-eastern parts of Mpumalanga, between Dirkiesdorp and Panbult (DIR and PAN respectively on Figure 5-2 (b) with the area indicated by F). Initiation was found to occur in the lower areas just north of Dirkiesdorp and losing supercell features just north of Panbult, just before the edge of the Highveld. One supercell that developed north-west of Panbult, did move onto the Highveld but lost its supercell features soon after. All the events that developed over the extreme southern parts of Gauteng and northern Free State south of the Highveld (area G Figure 5-2 (a)), moved onto the Highveld but most decayed soon after, although some did so just before or along various ridges in the region (ridge 1 and 3 on Figure 5-2 (a)).

In contrast to these areas where topography may have had an influence on the initiation and demise of supercells, no obvious topographical features are noted for the hotspot in the activity south of the Ermelo radar (area H on Figure 5-2 (b)). This region is located on a relatively flat portion of the Highveld. However small-scale topographical features may have had an influence on these areas, which would require further, more detailed, investigations. In addition, the impact of environmental factors (e.g., areas of convergence) would also need to be investigated.

No conclusions on the temporal or spatial distribution of right-moving supercells could be made due to the low number of events. The initiation of the 6 right-moving events occurred between 11:00 and 16:00 UTC, while their demise occurred between 12:00 and 17:00 UTC. With regards to the initiation and demise locations, 3 events developed west of the Irene radar (Figure 5-2 (a)), one north of the Magaliesberg mountain range, one within the Magaliesberg mountain range and the other on the edge of the Highveld. All events moved onto the highveld, although the event that developed in the lower lying area north of the Magaliesberg mountains decayed soon after, just before Ridge 2 (Figure 5-2 (a)). All 3 events that occurred over Mpumalanga developed on the Highveld, while two lost their supercell features just before moving off the Highveld in the south-east (Figure 5-2 (b)).

5.2 Lifespan

The percentage of events decreased as the lifespan of left-moving supercells increased (Figure 5-3 (a)). A significant number of the supercell events (75%) lasted between 30 minutes and 1 hour 30 minutes (Figure 5-3 (b)). The average lifespan was approximately 1 hour 12 minutes (median of 1 hour 6 minutes).

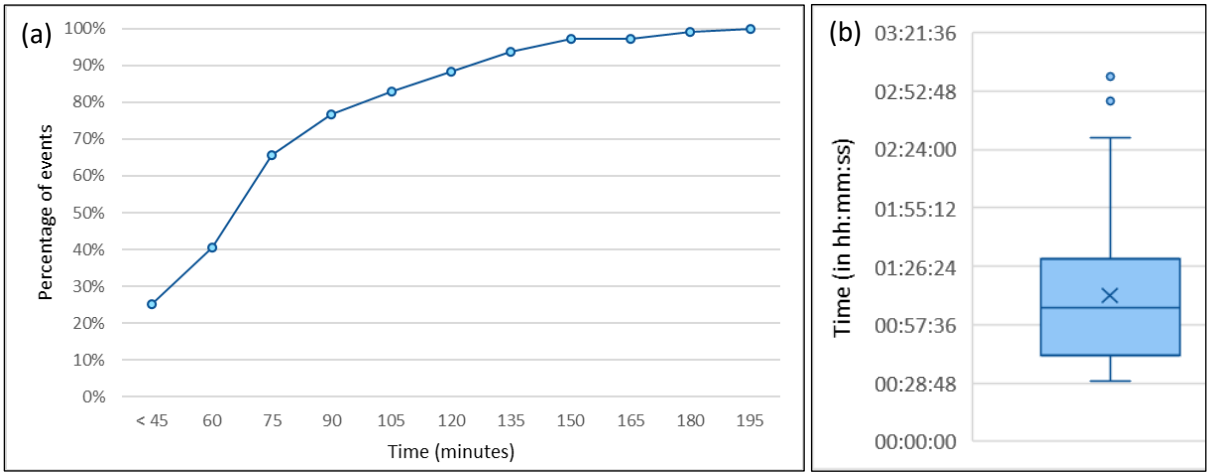

Figure 5-3: (a) A cumulative graph showing the percentage of left-moving supercell events that lasted for a given time (15-minute intervals). (b) A box and whisker plot showing the spread of the lifespan of the left-moving supercell events. For the box and whisker plot the minimum and maximum values (excluding the outliers) are shown by the lower and upper horizontal lines, the upper and lower whisker (vertical lines) each contain 25% of the data, the box contains 50% of the data and the lower and upper box boundaries indicate the 1st (25%) and 3rd (75%) quartile respectively. The line inside the box shows the median while the cross indicates the average. The data points above the upper whisker are the outliers.

In total, 98 (88%) of the left-moving supercells were short-lived events (lasting ≤ 2 hours) and 13 (12%) were moderate-lived events (lasting between 2 and 4 hours) (Figure 4-1). No long-lived events (lasting ≥ 4 hours) were identified. The average lifespan of the short-lived events was approximately 1 hour 3 minutes, while the average lifespan of the moderate-lived events was 2 hours 22 minutes. Of the 13 moderate-lived events 4 events had a track that extended beyond the 100 km range of either radar (Figure 4-1), thus these events could have lived longer. The longest-lived event (which was also considered an outlier as per Figure 5-3 (b)) lasted 3 hours and occurred on 16 November 2015 (A on Figure 5-4 (a)), which was also on a day where 6 events occurred in total (section 4.1). A total of 7 events lasted less than 31 minutes with the shortest-lived event occurring on 18 November 2019 with a lifespan of 29 minutes and 49 seconds (B on Figure 5-4 (a)). On 20 December 2018, 3 moderate-lived supercell events occurred, all 3 events occurred over Mpumalanga (C, D and E on Figure 5-4 (a)). No other day had more than a single moderate-lived event.

Of the 4 events with unknown initiation and/or demise times, 3 were short-lived and 1 was moderate-lived based on the available scans where supercell features were detected (Figure 5-2). It is likely that the moderate-lived event on 30 October 2013 and the short-lived event on 27 November 2013 lived longer and may even be classified as a long- or moderate-lived event respectively. The two short-lived events on the 4 February 2016 were short-lived, as data was available approximately 18 minutes before the first scan where supercell features were identified (Appendix 2).

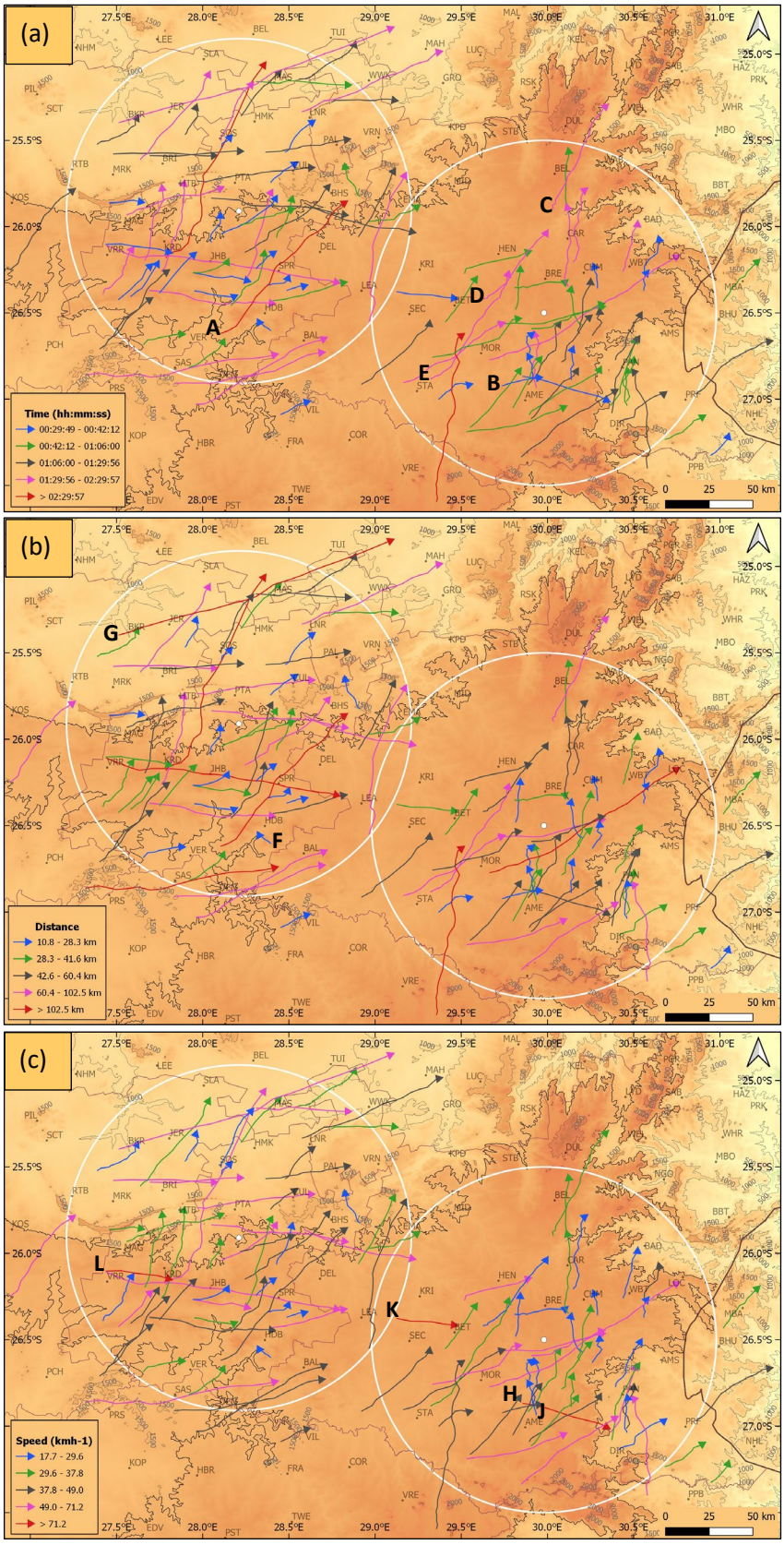

Figure 5-4: The left-moving supercell tracks with their (a) lifespan, (b) distance and (c) speed categorised into 5 groups based on the box and whisker plot in Figure 5-3, Figure 5-5 and Figure 5-7 respectively, with the lower whisker (blue), 1st quartile to median (green), median to 3rd quartile (grey), upper whisker (pink) and outliers (red) shown.

Of the 6 right-movers all were short-lived with an average lifespan of approximately 49 minutes. The longest-lived event occurred on 20 September 2014, lasting 1 hour 35 minutes, while the shortest-lived event was approximately 36 minutes and occurred on 9 November 2019 (Appendix 2). Comparing the lifespan of the right-movers to the left-movers that occurred on the same day, the right-mover was shorter lived in all cases except for 20 September 2014, where the left-mover only lasted 59 minutes (the right-mover lasted 1 hour 35 minutes).

5.3 Track distance

As was observed with the lifespan, as the distance increased, the percentage of events decreased (Figure 5-5 (a)), with 75% of the dataset tracking between 10.8 and 60.4 km (Figure 5-5 (b)). The shortest distance travelled was 10.8 km, on 15 November 2016 (F on Figure 5-4 (b)), which was also one of the few supercells that had a track from the south-east to the north-west rather than from the south-west (section 5.5). The longest distance tracked by a supercell (also considered an outlier on Figure 5-5 (b)) was 172.9 km, occurring on 1 November 2018 (G on Figure 5-4 (b)). The longest-tracked event may have lived longer and thus also tracked further as this thunderstorm was found to lose supercell features beyond 100 km from the radar. The post supercell thunderstorm remained intense and propagated out of the 200 km range of the radar. The average distance covered by the left-movers was 48.7 km (median of 41.6 km), while the average distance for the short-lived events was 41.6 km and 102.5 km for the moderate-lived events.

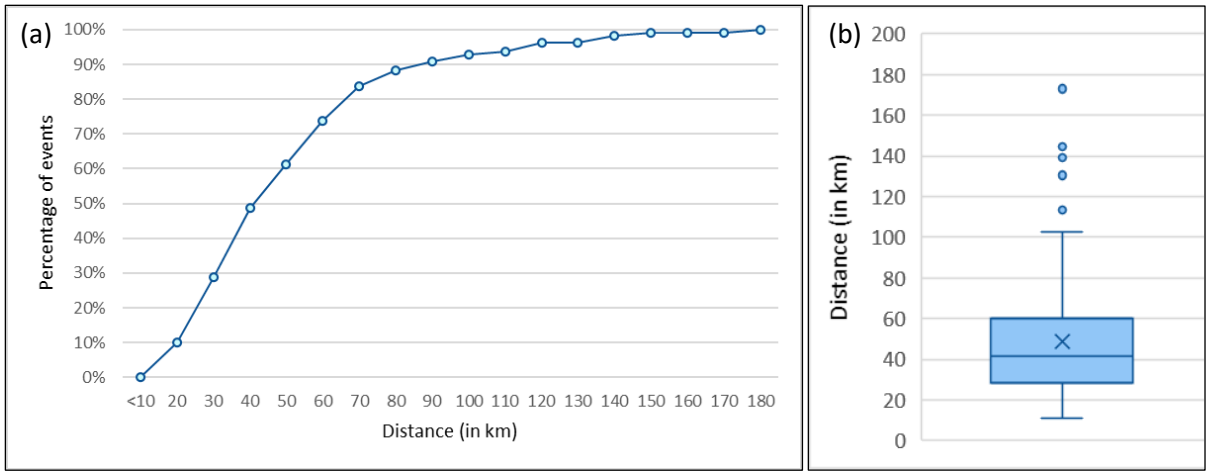

Figure 5-5: (a) Cumulative graph showing the percentage of left-moving supercell events that tracked for a specific distance (10 km intervals), (b) box plot showing the spread of the distance tracked by the left-moving supercell events. For the box and whisker plot the minimum and maximum values (excluding the outliers) are shown by the lower and upper horizontal lines, the upper and lower whisker (vertical lines) each contain 25% of the data, the box contains 50% of the data and the lower and upper box boundaries indicate the 1st (25%) and 3rd (75%) quartile respectively. The line inside the box shows the median while the cross indicates the average. The data points above the upper whisker are the outliers.

As expected, an increase in the lifespan was found to occur with an increase in the distance covered (Figure 5-6). However, as can be seen on Figure 5-4 (storm A longest-lived and storm G longest tracked) and Figure 5-6, the longest-tracked event was not the longest-lived event. The longest tracked event was only the 4th longest-lived event, lasting approximately 2 hours and 30 minutes. As noted by Bunkers et al. (2006a), long-lived supercells are not necessarily long-tracked supercells, which can occur in a short period of time with a fast-moving thunderstorm. The track distance depends on the speed of the supercell.

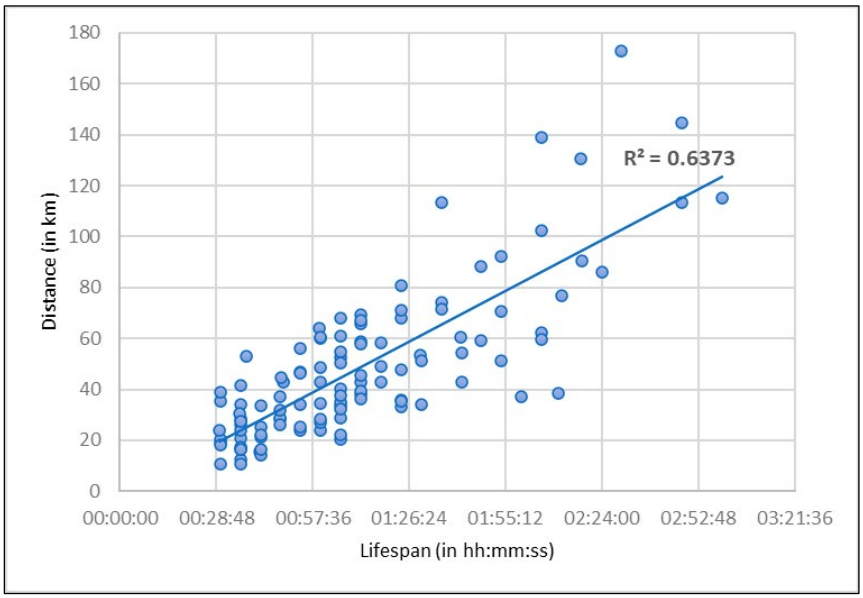

Figure 5-6: A scatter plot showing the relationship between the left-moving supercell lifespan vs the distance tracked.

Right-moving supercells were found to have an average track distance of 46.5 km. The shortest tracked distance for the right-moving supercells was 21.7 km, which occurred on 31 December 2019, while the longest tracked event occurred on 20 September 2014 at 74.3 km (Appendix 2). This longest tracked event was also the longest-lived event (section 5.2). Comparing the right-mover tracked distance with the left-moving supercells that occurred on the same day, the track was shorter for the right-movers on 19 October 2011, 9 November 2019, and 31 December 2019, otherwise it was either the same or longer.

5.4 Average speed

As was observed with the track distance and lifespan (both used to calculate the average speed), with an increase in the average speed there was a decrease in the percentage of events observed (Figure 5-7 (a)). The average speed for left-moving supercells was 40.8 kmh^{-1} (median of 37.8 kmh^{-1}) (Figure 5-7 (b)) while the average speed for the short-lived and moderate-lived events was

40.5 kmh^{-1} and 42.9 kmh^{-1} respectively. The fastest moving event occurred on 10 October 2010 (H on Figure 5-4 (c)) at 83.8 kmh^{-1} (also an outlier as per Figure 5-7 (b)), while the slowest moving event, at 17.7 kmh^{-1}, occurred on 14 December 2010 (J on Figure 5-4 (c)). A large percentage of the data (75%) showed to have speeds between 17.7 kmh^{-1} and 48.96 kmh^{-1} (Figure 5-7 (b)). The top 3 fastest moving events that travelled at speeds greater than 71 kmh^{-1} (H, K and L on Figure 5-4 (c)) were all categorised within the lowest lifespan category (Figure 5-4 (a)).

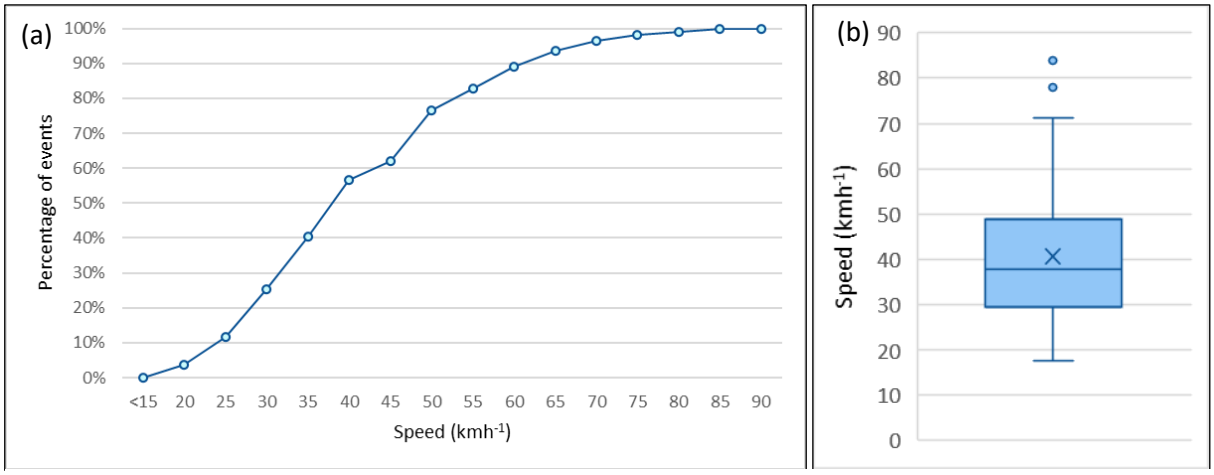

Figure 5-7: (a) Cumulative graph showing the percentage of left-moving supercell events that travelled at a specified average speed (5 kmh^{-1} intervals), (b) box plot showing the spread of the average speed travelled by the left-moving supercell events. For the box and whisker plot the minimum and maximum values (excluding the outliers) are shown by the lower and upper horizontal lines, the upper and lower whisker (vertical lines) each contain 25% of the data, the box contains 50% of the data and the lower and upper box boundaries indicate the 1st (25%) and 3rd (75%) quartile respectively. The line inside the box shows the median while the cross indicates the average. The data points above the upper whisker are the outliers.

The average speed for the right-moving supercells was 61.4 kmh^{-1}. The fastest moving event, which was also the fastest overall supercell within the database, occurred on 19 October 2011 travelling with an average speed of 98 kmh^{-1} (Appendix 2). The slowest moving event occurred on 31 December 2019 with an average speed of 36 kmh^{-1}, which was also the shortest tracked event. The speed of the right-moving events compared to the left-moving supercells that occurred on the same day, were greater for all cases except on 31 December 2019 (Appendix 2).

5.5 Track direction

The mean track direction for all left-moving supercells was found to be from the south-west with an average direction of approximately 224°. The largest number of events (29) were found to travel from the south-west but were closely followed by those travelling from the south south-west (28) (Figure 5-8). Very few events travelled from the west north-west (2), south-east (1) or south south-east (2).

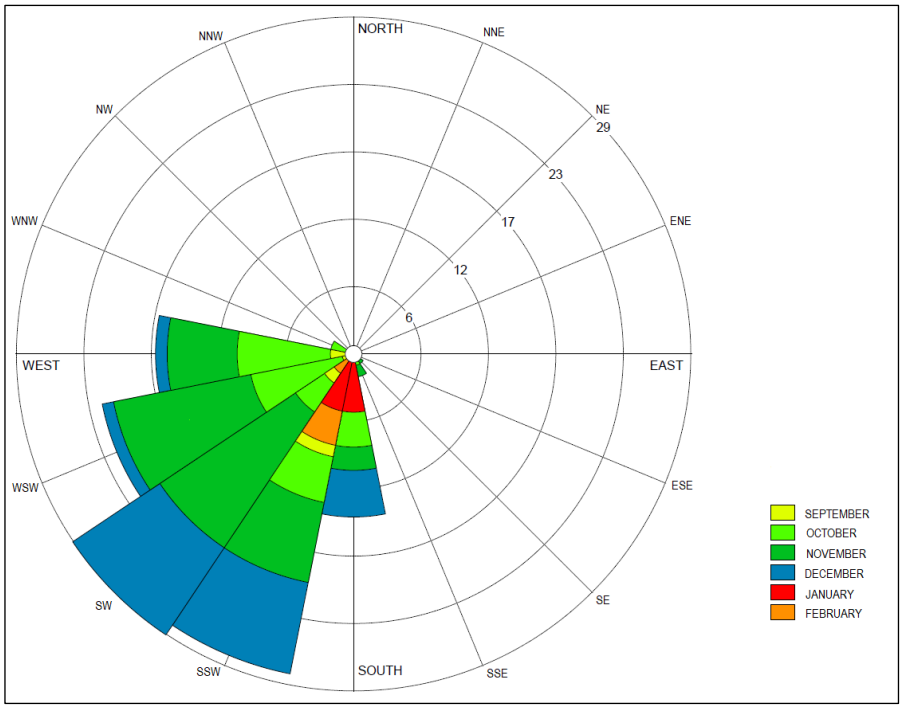

Figure 5-8: A rose diagram depicting the frequency count (number of events) of the left-moving supercell track directions (calculated from the start and end point), in the direction they are traveling from, using 16 bins (each containing an interval of 22.5°). The colours depict the number of events that occurred in the respective months in each direction. (Created using WRPlot View™)

The number of events that occurred in each direction for each month (Figure 5-8) as well as the mean track direction, showed a shift in the supercell tracks as the season progressed (also seen on Figure 5-9). The highest number of events was found to be from the west in September, west and west south west in October, south-west in November and December, south and south south-west in January and south south-west in February (Figure 5-8). The mean track direction, from which the supercells travelled, thus showed to be west south-westerly in September and October (249° and 239° respectively), south-westerly (227°) in November, south south-westerly (212 °) in December and then southerly (189°) in January. February saw the average tracks shift back again to south south-westerly (213°).

Keeping in mind the low sample size of the right-moving supercells, all 6 events showed a track travelling from approximately the north-west to south-east (Figure 4-1), ranging from 279° to 322° with an average of 300° (west north-west).

5.6 Spatial distribution of the left-moving supercell tracks

The spatial distribution for the left-moving supercells, calculated for each 1 km by 1 km grid with a search radius of 10 km, is shown in Figure 5-9. Left-moving supercells were found to be active over the entire Gauteng, while over Mpumalanga, supercell activity was found to extend mostly over

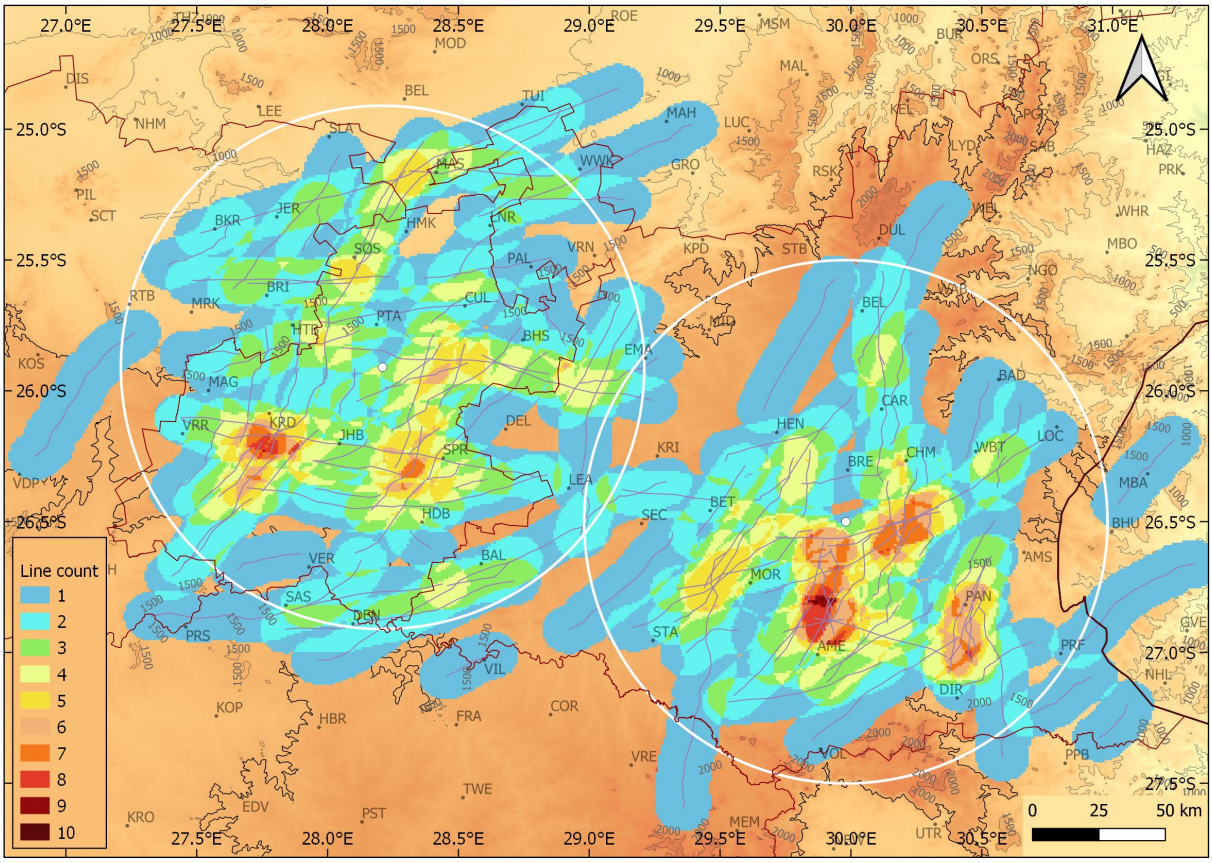

Figure 5-9: The track distribution of all left-moving supercells identified within the warm seasons (2010 to 2020). The colours indicate the number of tracks that occurred within a 10 km search radius for each 1km by 1km grid point and the pink lines show each of the supercell tracks used in the analysis.

the central and southern parts. A few hotspots of active supercell regions were identified (Figure 5-9). This includes the south-western and eastern Highveld of Gauteng (warm shades) as well as the south-eastern parts of Mpumalanga.

The area of greater activity over the south-western parts of Gauteng (highest for Gauteng) was found to occur between the 2 ridges in the area (Figure 5-2 (a)). As was noted with the initiation and demise location of the supercells in this region (section 5.1), topography may also be a contributor to this increased activity in supercells over this region. In general, the higher activity areas over Gauteng were confined to the Highveld, although there was an area of moderate activity found to occur over the lower lying north-western parts (Figure 5-9), in a region north of the Magaliesberg mountain range (Figure 5-2 (a)). Another noteworthy area of moderate to high activity was found just east of the Irene radar, extending south of Bronkhorstspruit (BHS on Figure 5-9) and out into Mpumalanga, south-west of Emalahleni (EMA on Figure 5-9). This area lies along the edge of the Highveld (Figure 3-1), thus the topography may have been a contributing factor to the increased activity. As discussed in section 5.1, an increase in supercell demise was also noted in this region.

The higher occurrence of supercells over Mpumalanga can be divided into 3 areas, an area south of the Ermelo radar (dark red on Figure 5-9) but north of Amersfoort (AME on Figure 5-9), another area east of the Ermelo radar (within 50 km from the radar), while a third area in the south-east between Dirkiesdorp and Panbult. The first two areas are on the Highveld, while the third area is found in a lower elevation area (Figure 3-1 and Figure 5-2 (b)) where supercells appear to be confined to this area. As shown in section 5.1, most supercells, in this lower lying south-eastern parts, decayed before moving onto the Highveld. An area of moderate activity can also be seen to the west and south-west of the Ermelo radar with approximately 5 events moving through the area between Standerton and Morgenzon (STA and MOR on Figure 5-9 respectively).

As was found with the initiation and demise locations (section 5.1), an area of lower to almost no activity was found in places over the western parts of Mpumalanga (Figure 5-9), within the 100 km range of the Ermelo radar. Although a more comprehensive comparison needs to be made, topography does not provide any visible characteristics that could explain this lower activity region. As mentioned in section 5.1, this area falls with the 100 km radial range of the Ermelo radar, where supercell identification was less impacted, and the area is found on a relatively flat portion of the Highveld.

5.7 Monthly track distribution

Early in the season (September), supercell activity, although low, was predominantly confined to the southern Highveld with activity increasing towards the north, particularly over the northern parts of Gauteng, from October and into November (Figure 5-10 (b) and (c)). Supercell activity was the highest over Gauteng in November, with this active region shifting to the south-eastern parts of Mpumalanga in December Figure 5-10 (d)). Activity was found to decrease significantly over Gauteng in January and into February (only 1 event in each month occurred in the given study period), while most of the events that did occur over Mpumalanga during these months occurred over the central and south-eastern parts (Figure 5-10 (e) and (f)).

When looking at the monthly distribution of the supercell tracks (Figure 5-10), the data availability also needs to be taken into consideration. Irene radar had a much higher availability compared to the Ermelo radar (section 3.3.1) thus may have influenced the general distribution to appear greater over Gauteng at certain times of the year (for example in November). However, the radar availability was relatively good for both radars from 2015 onwards, thus for the last 5 years the monthly distribution was analysed. The monthly distribution of the supercell tracks still showed this

trend in the shift in supercell activity across the warm season (not shown) although a decline in events was observed over Gauteng as was also discussed in section 4.2.

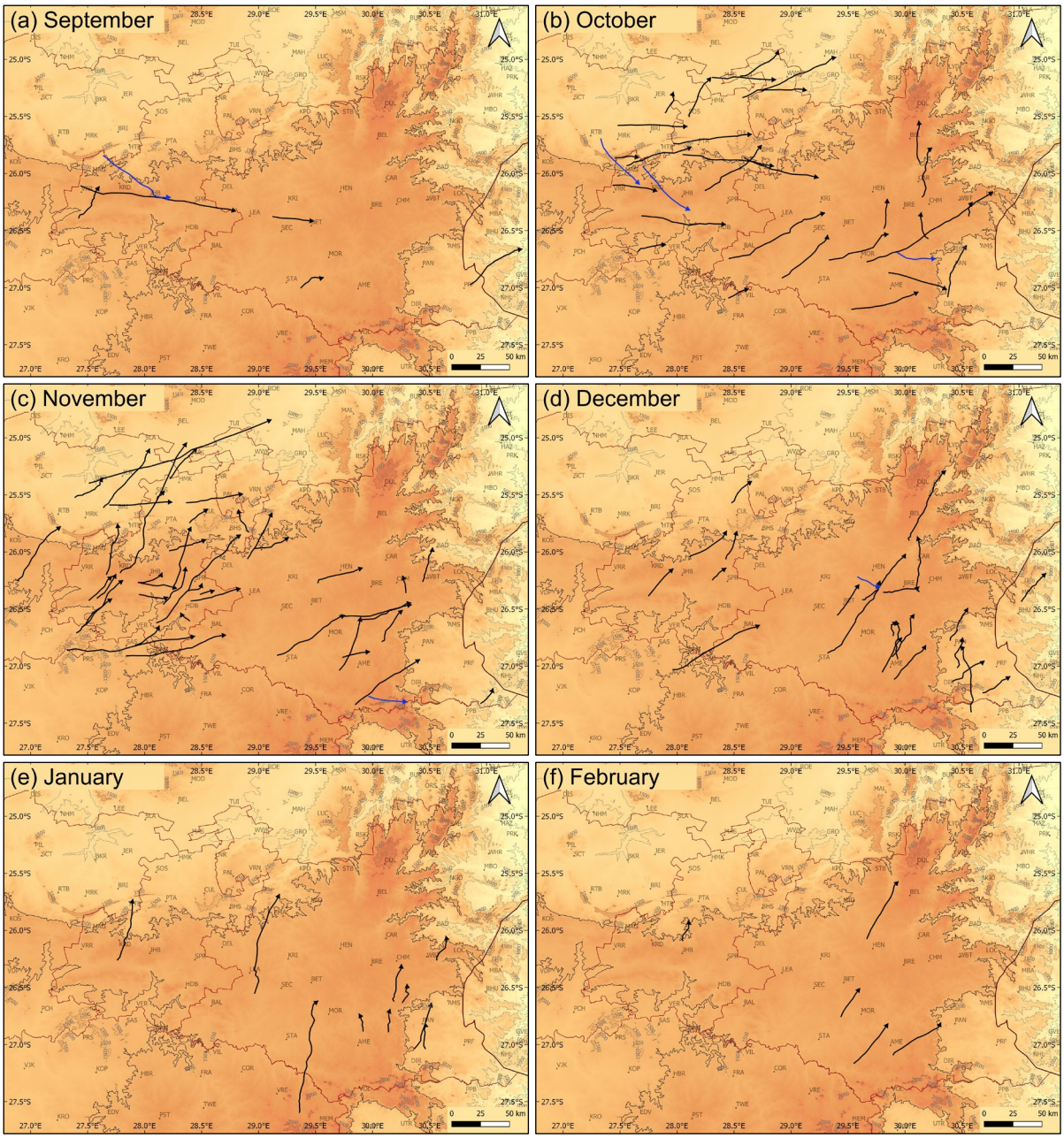

Figure 5-10: All left-moving (black) and right-moving (blue) supercell tracks identified during the warm seasons of 2010 to 2020 that occurred in (a) September, (b) October, (c) November, (d) December, (e) January, and (f) February.

5.8 Summary

Left-moving supercells were found to develop between 11:00 and 17:00 UTC, peaking at 13:00 UTC, while supercell demise predominantly occurred between 12:00 and 18:00 UTC with the peak at 14:00 UTC. Most of the events (88%) were short-lived with only 13 moderate-lived events (12%) and no long-lived events. Most events lasted between 30 minutes and 1 hour 30 minutes, with

an average lifespan of 1 hour 12 minutes. The average distance tracked was approximately 49 km with most events tracking between approximately 10 and 61 km. The longest-lived event lasting 3 hours and the longest-tracked event travelled approximately 173 km. As the lifespan increased the distance also tended to increase. However, the longest-tracked event was not the longest-lived event, likely due to the variation in the speed of the supercells.

Hotspots in the initiation, demise and spatial distribution of left-moving supercells were identified. This included the southern parts of Gauteng and southern central and south-eastern parts of Mpumalanga. Some areas of moderate activity were also observed over the north-western parts of Gauteng, along the edge of the Highveld over the eastern parts of Gauteng and areas west of the Ermelo radar. An area of lower activity was identified over the north-western parts of the Ermelo radar, within the 100 km radial range. Left-moving supercells predominantly travelled from the south-west, however, from September to January the mean track direction shifted from west south-westerly to southerly and then south south-westerly again by February. A shift in the track distribution was also noted with activity starting on the southern Highveld, increasing towards the north by October, with Gauteng containing most of the activity in October and November. From December the active area shifted to the south-eastern parts of Mpumalanga, while decreasing significantly over Gauteng.

Due to the low number of right-moving supercells, only some observations were provided. All right-moving supercells developed between 11:00 and 16:00 UTC, decaying between 12:00 and 17:00 UTC. The initiation and demise of 3 of the events occurred over Gauteng, west of the Irene radar, and the other 3 on the Highveld of Mpumalanga. All were short-lived events, with an average lifespan of 49 minutes and tracked on average approximately 47 km. The longest-lived event lasted 1 hour 35 minutes, which was also the longest-tracked event, travelling approximately 74 km. All events travelled from the north-west to south-east.

Chapter 6: Discussion of results

Since supercells were previously considered rare in South Africa, and doppler radar only became operational in 2010, little is known about the frequency of supercells over Gauteng and Mpumalanga as well as their characteristics, pertaining to their initiation, track, lifespan, and demise. The following research questions formed the basis on which this research was conducted for Gauteng and Mpumalanga;

1. What frequency do supercells have?
2. What temporal distribution (seasonal, monthly, diurnal etc.) do supercells exhibit?
3. Is there a pattern in the initiation and demise location for supercells?
4. What is the general lifespan of supercells?
5. Is there a trend in the way supercell thunderstorms move, with regards to the direction of movement, distance covered, speed, and spatial distribution?

The aim of this study was to investigate the characteristics of supercells over Gauteng and Mpumalanga during the warm season (September to February), using all available radar data from 2010 until 2020. First a supercell database was established and included both left and right-moving supercells, then their characteristics were investigated. The data and methodology used to complete this was discussed in chapter 3 while the results were provided in chapter 4 and 5. This chapter discusses the results presented in chapter 4 and 5. It starts with a discussion on the supercell database (section 6.1) including the shortfalls identified within this study, then looks at the temporal distribution characteristics (section 6.2), followed by the characteristics identified for the left- and then right-moving supercells (section 6.3 and 6.4 respectively).

6.1 The radar-derived supercell database

A total of 115 left-moving and 6 right-moving warm season supercells were identified in this research, over a period of 9 available seasons (2010 to 2020), and 67 event days. On average almost 2 supercell events occurred on a given supercell event day. Supercells were previously considered rare in South Africa with only 1 event found to occur on the Highveld during a period of 7 years in the 1970s (Admirat et al., 1985; Carte, 1979, 1981; de Coning et al., 2000). Growing evidence has shown that supercell frequency is higher than this, as a number of confirmed supercell events have been reported since 1997, through published case studies (e.g., de Coning et al., 2000; Lekoloane et al., 2021; Powell and Burger, 2014) as well as reports and media releases (e.g., Kruger et al., 2018; Modika, 2020; Sebego and Rae, 2017). In addition, Rae (2014) provided a small supercell database of 15 event days

that occurred over Gauteng and nearby regions during the summer seasons between 1985 and 2011. The database established in this dissertation has provided further evidence that supercells do occur over the Gauteng and Mpumalanga province of South Africa, and that their frequency is higher than that previously believed.

In the study conducted in Oklahoma (USA), a total of 943 supercells were identified over a 10-year period (Hocker and Basara, 2008) which is significantly higher than the number identified in this research. It is also important to note that the area covered by Oklahoma is almost double the study area considered in the research presented in this dissertation and all seasons, not only the warm seasons, were considered with the goal to identify all not only the more classic or severe events. The study done in south-eastern Romania also had a larger database in comparison to the research presented in this dissertation, with 282 events identified over only 4 years (Antonescu et al., 2010). The study in Greece had a smaller database of only 49 events (30 event days) over a 12-year period (Christodoulou and Sioutas, 2017), although as was discussed in section 2.8, their definition used to identify the events was limited to reflectivities exceeding 55 dBZ and the thunderstorm had to last 2 hours. The study area in Romania was slightly smaller and that in Greece slightly larger than that used in the research presented in this dissertation.

The database established in this research is the first radar-based supercell thunderstorm database in South Africa. Although Rae (2014) provided a smaller database of 15 supercell events, some of these events were based on observations rather than radar data. In addition, some of the cases were based on the identification of a WER or BWER only and did not contain either a hook echo or mesocyclone, as was required in the classification criteria used in the present research as well as other studies around the world (e.g., Bunkers et al., 2006a; Doswell III and Burgess, 1993; Klimowski et al., 2003; Moller et al., 1994).

Right-movers were found to have a much lower occurrence than left-movers, which was anticipated for the region as it falls within the Southern Hemisphere, where the winds generally back with height (Dyson et al., 2015 and discussed in section 3.2), favouring left-moving supercells (Klemp and Wilhelmson, 1978; Weisman and Klemp, 1984). It is not uncommon for left- and right-movers to occur within the same environment, although usually left-movers (right-movers) are favoured when the vertical wind shear backs (veers) with height (Klemp and Wilhelmson, 1978; Weisman and Klemp, 1984). All right-mover events in this research occurred on a day where either 1 or 2 left-movers were also identified. In addition, only on one day did 2 right-mover events occur (on all other days only 1 event occurred). According to Klemp and Wilhelmson (1978), in a unidirectionally sheared

environment both left- and right-moving supercells have an equal chance of survival. These 5 case days would need to be compared with the vertical windshear to confirm if this was the case (not within the scope of this research).

6.1.1 Shortfalls of the supercell database

This supercell database is by no means an exhaustive list of all events, as the radar data availability (section 3.3.1), limitations of the radar (e.g., resolution, height of the radar beam and scan strategy (section 3.3.2)), and location of the features relative to the radar may have played a large role in the ability to identify all case studies. In addition, the subjectivity in the method used to identify supercells may also have had an impact. The aim of this research was not to identify all the events, given all these limitations, but to rather identify as many cases as possible.

Data availability, especially during the first 5 seasons, played a significant role in the identification of events. The impact of availability on supercell identification was significant where entire seasons were missing, i.e., 2012-2013 for both radars and 2011-2012 and 2014-2015 for the Ermelo radar (section 3.3.1), during which period either very few or no events were identified. The impact is unknown on those days where radar data was not available for a shorter period (e.g., a day, a few days, or part of a day). A more comprehensive investigation would need to be undertaken to determine if thunderstorms occurred during these shorter periods, and then to determine if the environment was conducive for supercell development.

Distance from the radar was also likely a major limiting factor, with most events identified within the 100 km range from each radar (section 4.1) and all within 150 km. It was highlighted by Burgess and Lemon (1990) and Donaldson (1970), that a 200 km maximum range should be sufficient to identify supercells, given an antenna beamwidth of 1° (section 3.3.2.2). However, this may not be the case for the Irene and Ermelo radar (both containing an antenna beamwidth of approximately 1°). Resolution was one of the biggest limitations when identifying events beyond the 100 km range, as small-scale features became more difficult to identify with distance (see a comparison of a hook echo viewed by both radars in section 3.3.2.2). The height of the radar beam increasing with distance, also possibly contributed to supercell identification (3.3.2.3), although the impact was low. The hook echo, a low-level feature, may be missed at certain distances if the height of the lowest radar beam extends above the feature, however, the mesocyclone (anticyclone) should still be detected as it is usually located in the mid-levels (Bunkers et al., 2006a).

The distance that the mesocyclone (anticyclone) is located from the radar as well as other flow patterns surrounding it, may also have made the identification of this feature more challenging. The changes observed are described in detail by Brown and Wood (2007) and briefly highlighted in section 2.3.3. The Nyquist velocity also played a role in the mesocyclone (cyclone) identification, as velocity folding easily occurs with low Nyquist velocities. The Nyquist velocity varied significantly throughout the dataset (section 3.3.2.1) but was particularly low prior to 6 November 2010 for both radars and from November 2013 for the Ermelo radar. Although data was not useable to identify the mesocyclone(anticyclone) prior to 6 November 2010, data for the Ermelo radar after November 2013 was mostly usable and several events with a mesocyclone were still identified. However, some events were likely undetected especially where reflectivity features were not well defined.

The subjectivity in the methodology used to identify supercells may also have resulted in the non-detection of the less classic events. Due to the number of days that needed to be investigated for each radar, reflectivity data was usually consulted first. If a thunderstorm did not show any signs of severity (example high reflectivity), longevity, deviation, an inflow notch, some suggestion of a hook echo, high reflectivity gradient on the inflow side, or a WER/BWER then it was not investigated further on the Doppler velocity field. This may have resulted in the less classic cases not being detected especially in areas beyond the 100 km range, which were additionally impacted by resolution and height of the radar beam. Since the Doppler velocity field was not analysed for each thunderstorm, cases that only had a mesocyclone (anticyclone) on the Doppler velocity field may have been missed. An attempt was made to ensure confidence in identifying as many events as possible, however, some cases may still have been omitted. The author's knowledge or experience may also have contributed to this, therefore an expert in the USA was consulted on some of the more difficult cases. A more objective method may need to be identified to expand on this database and ensure all events are captured.

The database of right-moving supercells was very likely unrepresentative of all events that occurred within the 10-year period. The fact that no exclusive right-moving supercell day was identified was more likely due to the shortfalls within the methodology used. The focus was more towards the easier to identify left-moving supercells (section 3.5). In addition, as was noted by the author, the hook echo on these right-moving supercells were not as well defined, thus without a clear mesoanticyclone, it was difficult to confirm several other potential cases (section 3.5). A more focused study to specifically identify right-moving supercells within this region would need to be carried out to ensure all cases are captured.

6.2 Temporal distribution characteristics of supercells

Similar to findings made by Antonescu et al. (2010) for supercells in Romania and by Christodoulou and Sioutas (2017) over Greece, supercells over Gauteng and Mpumalanga were found to occur more often in isolation rather than with mass outbreaks, with only 15 days containing 3 or more supercells, of which only 3 days contained 6 or 7 events. It is possible that supercells occurred over the neighbouring provinces (not within the radar coverage area considered in this dissertation) on the given event days thus this observation is only applicable over Gauteng and Mpumalanga. Further research is required to provide a definitive answer as to the isolated nature of supercells over South Africa.

Forecasters are often aware of severe thunderstorms occurring over more than just 1 day, and as was shown by Simpson and Dyson (2018), a number of severe weather reports were found to occur over 2 consecutive days over the Highveld of Gauteng and Mpumalanga (not only in 2016 but during previous years as well). However, in this research it was found that supercells rarely developed over more than 1 day. A similar observation was made by Christodoulou and Sioutas (2017) for supercells over Greece, where only on two occasions did supercells develop on 2 consecutive days. Further studies would need to be conducted to investigate this in more detail and to determine the relationship between supercell occurrence and severe weather reports within this region.

6.2.1 Seasonal characteristics

An average of approximately 13 events and 7 event days were found to occur per season, although the average was slightly higher at approximately 15 events and 9 event days for the last 5 seasons, where data availability was high for both radars. This average number of event and event days was much lower than that found in the USA, where, in Oklahoma for a 10-year period, an average of 94 supercells and 28 supercell event days was found to occur per year (Hocker and Basara, 2008). However, as discussed in section 6.1 Oklahoma had a larger study area and considered all seasons. No comparison on the frequency of events per season in other regions such as Greece and Romania (Antonescu et al., 2010; Christodoulou and Sioutas, 2017) can be drawn as these statistics were not provided.

The interannual variability of warm season supercells were analysed but no clear temporal trend was established. However, there was a decline observed in the number of events that were identified on the Irene radar (predominantly covering Gauteng) in the last 5 seasons. The most active supercell season, and the peak for the Irene radar, occurred in 2013-2014. This season contained the

single most active event day with 7 supercell events occurring on 28 November 2013. According to Pienaar et al. (2015), the 2013 season was a particularly severe hail season with hailstorms resulting in significant damage. November 2013 in particular saw numerous hailstorms, including 2 supercell event days over Gauteng (11 and 28 November 2013), that resulted in a loss to insurance companies amounting to over 2 billion South African Rands (Dyson et al., 2021).

Supercell event days peaked during 2018-2019, which was also the peak for supercell events in the last 5 seasons. According to Chikoore and Jury (2021), the summer season of December to February 2018-2019, was one of the 10 driest summer seasons for the eastern parts of South Africa between 1979 and 2019. However, this dry spell during December to February did not seem to deter the development of supercells, with 8 out of the 12 supercell event days occurring during these months. In addition, 20 December 2018 experienced 3 moderate-lived events occurred on a single day (no other day experienced more than 1).

The 2015-2016 season was also a noteworthy period, as supercell event activity was also high. The 16th of November 2015 was a significant event day during this season, as it contained the longest-lived event and had a total of 6 supercell events that occurred on this day. There were numerous reports of severe weather (large hail, damaging winds and flooding) across Gauteng on this day, resulting in injuries as well as damage to property and infrastructure (SAWS, 2015). Blamey et al. (2018) and Chikoore and Jury (2021) identified the 2015-2016 summer as one of the driest summer seasons for this region since 1950.

The least active supercell season in the last 5 seasons was 2016-2017, despite a very active severe thunderstorm season over the Highveld during November 2016, as highlighted by Simpson and Dyson (2018). Despite the identification of 4 supercell event days in November, only 2 days corresponded to reports of severe weather out of a total of 17 days documented by Simpson and Dyson (2018). Supercells are known to have a low frequency compared to other severe thunderstorms (Burgess and Lemon, 1990; Doswell III, 2001; Moller et al., 1994). A future study to establish the frequency of supercells resulting in severe weather over Gauteng and Mpumalanga, and comparing it to other severe thunderstorms would need to be conducted to understand their overall contribution better.

Another observation made during the early 2016-2017 season (September to November) was that drought conditions from the previous season were still prevailing over the region, with a number of heat waves reported in October 2016 (Simpson and Dyson, 2018). All supercell events identified in

the present research, occurred between September and November in 2016-2017. Thus, as noted with the 2018-2019 season, the dry conditions did not deter the development of supercells. Further studies investigating the connection between supercell development and rainfall variability is required.

6.2.2 Monthly characteristics

Supercell activity was found to be the highest during spring and early summer, decreasing during the later summer months. The supercell event days peaked by the second half of October (although event days were the same for October and November). Supercell events peaked during the second half of November and all mass outbreaks, with either 6 or 7 events on a single day, were found to occur in November. This offset in the peak, between the event and event days, was also found to occur in Oklahoma (USA), although during the spring season the peak in supercell events occurred first followed by the event days 3 to 4 weeks later (Hocker and Basara, 2008). In addition, Hocker and Basara (2008) also found mass outbreaks to be more likely within certain months, including April which falls within the spring season in Oklahoma.

The peak in the supercell activity identified in this research corresponded with the peak in severe thunderstorms observed over the interior of South Africa (Admirat et al., 1985; Carte and Held, 1978; Goliger and Lunt, 1997; Held and Carte, 1979). Hailstorms were also found to peak in November over the Highveld of South Africa (Admirat et al., 1985; Carte and Held, 1978; Dyson et al., 2021; Olivier, 1990), decreasing as the summer season progressed. In addition, Blamey et al. (2017) also found that the interior of South Africa had a higher potential for severe convective environments during the early summer months, with a peak occurring in November.

The peak in supercell activity also corresponds to research globally on severe thunderstorms and supercell thunderstorms. Tornadoes were found to be most active during the late spring into the early summer months over Poland (Taszarek and Brooks, 2015), while Finland observed a slightly later peak during the later summer months (Rauhala et al., 2012). Lukach et al. (2017), found that hail days (based on radar derived parameters) peaked during the summer months over Belgium, but severe hail days peaked during late spring. Supercell activity over the USA also showed to increase during early spring and into the early summer months peaking during the late spring season (Hocker and Basara, 2008). However, in Greece and Romania the peak was found to occur slightly later during the early and mid-summer season (Antonescu et al., 2010; Christodoulou and Sioutas, 2017).

Over the area where supercells were identified in this research, the atmosphere is conditionally unstable with high values of vertical wind shear (speed and direction) during the spring and early

summer months (Blamey et al., 2017; Dyson et al., 2015). This environment is conducive for not only severe thunderstorms to develop but in particular supercell thunderstorms (Moller et al., 1994; Ray, 1990). The combination of weather systems, discussed in section 3.2, result in a north-easterly to north-westerly flow in the lower levels and westerly to south-westerly flow in the upper levels from September to December in this region. Dyson et al. (2015), describes weather systems during this period to have more extra-tropical characteristics. Although wind shear values peak during the spring season, the peak in instability only occurs in December over the Highveld (Blamey et al., 2017; Dyson et al., 2015). According to Johns and Doswell III (1992) and Moller et al. (1994) supercells can occur in environments with low instabilities as long as the vertical shear is strong. Vertical wind shear was found to be the most important parameter with regards to supercell development (Johns and Doswell III, 1992; Moller et al., 1994).

During the later summer months (January and February), where a large decrease in supercell events was observed, changes to the synoptic conditions saw the south-eastward migration of the surface high east of the country, westward migration of the trough and a southward migration of the upper high (section 3.2). Thus, winds are weaker aloft, and in particular over Gauteng, the ideal anticlockwise (backing) shift in wind direction with height no longer occurred. Dyson et al. (2015) describes the circulation patterns during late summer to be more tropical in nature with high convective instability and a good influx of moisture. A more detailed study looking at the environment that occurred during the supercell event days identified in the present research is required.

A shift in supercell activity was found to occur over Gauteng and Mpumalanga as the season progressed (section 4.3 and 5.7). Activity was found to start over the southern Highveld in September, spreading northwards throughout spring, with higher activity in the west (over Gauteng) by November. Over Gauteng (Irene radar), the peak in supercell events was still found to occur during the second half of November, however, the peak in event days occurred during the second half of October and first half of November. A shift in this higher activity, towards the south-east of Mpumalanga, occurred in December, where it continued (although with fewer events) into January and February, with activity decreasing significantly in the west (over Gauteng) during late summer. Over Mpumalanga (Ermelo radar), the peak in supercell activity (events and event days) was found to occur during the second half of December, although a secondary peak was observed during the second half of October. This suggests that the supercell season over Gauteng and Mpumalanga are different with the former occurring earlier and the latter later in the season.

This initial northward and then south-eastward shift in activity, observed in this research, corresponds to the seasonal shift in the number of potentially severe convective days identified by Blamey et al. (2017) but does not correspond to the westward shift of hailstorms identified by Dyson et al. (2021) and Olivier (1990). Blamey et al. (2017), observed a higher area of total severe environment days over the south-eastern parts of Mpumalanga from November, which remained in this region (although decreasing in number) until February. The monthly distribution of supercells in general corresponded well to the monthly potential severe convective environments determined by Blamey et al. (2017).

The change in supercell activity as the season progresses can be explained by the change in the atmospheric conditions observed throughout the season. As previously discussed, earlier in the season vertical wind shear values are more favourable, with very similar conditions for both Gauteng and Mpumalanga during September to November (Figure 3-2). However, this does not explain the higher activity over Gauteng compared to Mpumalanga in November. Moisture advection and instability (not investigated) may explain this lower activity over Mpumalanga during this month, rather than wind shear conditions. However, from December onwards as activity decreased over Gauteng but increased over the south-eastern parts of Mpumalanga, the vertical mean wind profile was found to differ over the two regions (Figure 3-2). Over Gauteng winds lighten significantly by December, while remaining stronger over Mpumalanga, and from January directional shearing is less favourable over Gauteng, but the anticlockwise shift with height is maintained over Mpumalanga. A more detailed study looking at all factors such as wind shear, moisture and instability is required to better understand this seasonal distribution of supercells observed.

6.3 Characteristics of left-moving supercells

Most of the left-moving supercells identified in this research, were found to develop during the day between 11:00 and 17:00 UTC peaking at 13:00 UTC, while supercell demise predominantly occurred between 12:00 and 18:00 UTC with a peak at 14:00 UTC. This is very much in line with research done on supercells in the USA (Bunkers et al., 2006a; Hocker and Basara, 2008), Romania (Antonescu et al., 2010) and Switzerland (Feldmann et al., 2021), corresponding to the maximum diurnal heating.

The initiation and demise times also corresponded to thunderstorm and severe thunderstorm activity over South Africa. Thunderstorm activity over the north-eastern Free State, peaked between 12:00 and 14:00 UTC (Steyn and Bruintjes, 1990) while hailstorm activity over the north-eastern parts

of the country was greatest between 10:00 and 18:00 UTC, peaking between 15:00 and 16:00 UTC (Admirat et al., 1985; Olivier, 1990). The peak in hailstorm activity did not correspond to the peak in supercell initiation, but rather the peak in supercell demise. Hailstones can still be fairly large during the collapse stage of a supercell (Burgess and Lemon, 1990; Lemon, 1977).

In addition, the diurnal distribution identified in this research, also corresponded to other climatological studies on severe thunderstorms around the world, such as tornado activity in Poland and Finland, as well as hail day frequency in Belgium (Lukach et al., 2017; Rauhala et al., 2012; Taszarek and Brooks, 2015). Both studies, examining tornado activity (although not all supercell related events), showed very low to no activity overnight and during the morning hours, as was observed in the research presented in this dissertation. This was also found to be the case for hail frequency over the north-eastern parts of South Africa (Olivier, 1990).

Left-moving supercells were predominantly found to be short-lived (lasting ≤ 2hours), with an average lifespan of 1 hour 12 minutes, which agrees with the average lifespan observed within the USA of 1 to 2 hours (Bunkers et al., 2006a; Hocker and Basara, 2008). Similar to findings in Romania and Oklahoma (USA), made by Antonescu et al. (2010) and Hocker and Basara (2008) respectively, most supercells in this research were also found to last between 30 minutes and 1 hour 30 minutes, with a decrease in number of events as the lifespan increased. The average lifespan of thunderstorms over the Highveld of Gauteng and north-eastern Free State was found to be less than 30 minutes (Mader et al., 1986; Steyn and Bruintjes, 1990), thus the supercells identified in the research lived on average at least 30 minutes longer. It is important to note that the supercell lifespan does not correspond to the thunderstorm lifespan, which may be much longer. An investigation into the thunderstorm lifespan is required to better understand the longevity of the entire thunderstorm that was associated with supercell features at some point in its lifetime. This could include examining when supercell features developed after the thunderstorm developed and how long after supercell features dissipated, the thunderstorm decayed. Reasons for demise (e.g., it experiences a merger with other thunderstorms or developed into a bow echo) may also need to be investigated to understand the impact on the average lifetime observed in this research.

In this research only 12% of the events considered were moderate-lived (lasting between 2 and 4 hours) and no long-lived events (lasting ≥ 4 hours) were identified, with the longest-lived event lasting 3 hours. This is in contrast to other regions such as in the USA, Romania and Greece (Antonescu et al., 2010; Bunkers et al., 2006a; Christodoulou and Sioutas, 2017; Hocker and Basara, 2008) where some events lasted between 5 and 7 hours. Bunkers et al. (2006a), found some regions in the USA also

had a low frequency of long-lived supercells. They noted that although longevity in this area may have been impacted by mountainous terrain, limited moisture in the lower levels or lacked strong deep-layer shear, limited radar coverage may also have been a contributing factor. The lack of long-lived events, in the research presented in this dissertation, may be due to radar limitations (sections 3.3.2, 4.1 and 6.1.1), rather than other meteorological or topographical characteristics. Only 4 moderate-lived events extended beyond the 100 km range, with the possibly that they may have lived longer (possibly long-lived). A more comprehensive study needs to be conducted to ascertain if the lack of long-lived supercell events was due to limitations in the data collection process or due to meteorological or topographical characteristics in the region. This could be extended to include the moderate-lived events as well as they too had a low frequency.

The spatial distribution of left-moving supercell activity (initiation, track, and demise) was found to be greater in places over the southern parts of Gauteng and Mpumalanga, as well as over the north-western parts of Gauteng north of the Magaliesberg mountain range. Hotspots in activity over Gauteng included the south-western parts between the two ridges in the area as well as on the eastern Highveld. Over Mpumalanga hotspots occurred predominantly to the south and south-east of Ermelo. Supercell demise was found to have a north-eastward shift in location from the supercell initiation, which corresponded to the predominantly south-west to north-east track observed for the left-moving supercells.

Not all supercell initiation, demise or track locations were influenced by topography. A much stronger link was identified by other studies such as in the USA (Bunkers et al., 2006a; Hocker and Basara, 2008), Greece (Christodoulou and Sioutas, 2017) and Switzerland (Feldmann et al., 2021). Activity was high over the Highveld, which covers most of Gauteng and Mpumalanga, but higher activity was also noted in lower lying areas (e.g., north-western Gauteng and south-eastern Mpumalanga). In addition, some areas on the Highveld also experienced low activity (e.g., areas of western Mpumalanga). Some possible topographical influences were noted (discussed in more detail in section 5.1 and 5.6), especially near the boundaries of the Highveld as well as between various ridges and the Magaliesberg mountain range in Gauteng. However, in other areas where hotspots in activity were observed, such as the area south of the Ermelo radar, no obvious topographical features were found, but small-scale features cannot be excluded. A statistical and more comprehensive study needs to be conducted to determine the relationship between topography and supercell initiation, track, and demise especially where hotspots in activity were found to occur.

Markowski and Dotzek (2011) investigated the relationship between orography and supercells using numerical simulations. They concluded that the direction of the ground relative wind was an important component, which was suggested by Taszarek and Brooks (2015) to also be a possible cause for enhanced tornado occurrences in areas were topographical influences were identified. The flow direction was also found to be a factor (amongst other such as flow speed and height of the freezing level) in precipitation growth and decay along the Swiss Alps, with precipitation growth found to occur on the upwind slopes and decay on the downwind slopes (Foresti et al., 2018). Markowski and Dotzek (2011) found that supercells weakened (low- and mid-level updraft strength and vertical vorticity) on the lee of the slope (relative to the surface wind) or where topography dropped into a valley due to the convective inhibition increasing and relative humidity decreasing. Strengthening of a supercell on the windward side or where terrain moved out of a valley (due to an increase in CAPE and humidity and a decrease in convective inhibition) was found to occur, although it depended on the direction of the supercell movement relative to the surface wind, height of the topography etc. Storm relative helicity was also found to vary and impact the effects of weakening and strengthening although to a lesser extent compared to the thermodynamic fields. Feldmann et al. (2021) found that most supercells that moved upslope (e.g., along the main Alpine ridge) did not intensify, resulting in the decay of such storms and in general there was a decrease in activity as elevation increased. Prociv (2012), examined the relationship of terrain over the southern Appalachian Mountains (USA) on supercells and found that where supercells encountered a downslope area vorticity stretching and thus strengthening of the low-level rotation could occur. In general, she found that lower elevations and shallow slopes enhanced the rotational strength.

As discussed in section 5.1, several thunderstorms in this research, were shown to develop supercell features (i.e., initiation location) along Ridge 1 (Ridge 2) (Figure 5-2 (a)) over the south-western parts of Gauteng and then moved towards the north and north-east, and then decaying along Ridge 2 (Magaliesberg mountain range). A detailed study is required to fully understand the impact of the terrain over this region, given the east to west orientation of the terrain, south-west to north-east track of supercells observed in the area and mean northerly to north-easterly low-level winds during the spring and summer season. Similarly, areas along the Highveld, where supercell features showed to dissipate soon after moving off the highveld or even onto the Highveld would also need to be investigated in more detail.

An area of lower to almost no supercell activity was found to occur over the western parts of Mpumalanga. No obvious topographical features were noted in this region to explain the low activity in supercells. Considering this region falls within the 100 km radius of the Ermelo radar, radar

limitations are not necessarily the cause either. Further detailed investigations are required to understand the reason for this lower activity area.

The spatial distribution of left-moving supercells corresponds fairly well to the reports of over 200 tornadoes in the same region determined by Goliger and Lunt (1997), especially over the highly populated area of Gauteng. A higher number of tornado reports occurred over the south-western parts of Gauteng between the two ridges in the area, with other active areas including the eastern Highveld and north-western parts of Gauteng, all of which correspond to the supercell hotspots and moderate activity identified within this dissertation (section 5.1 and 5.6). Over Mpumalanga tornadoes, although with a low frequency, were reported in the south-east, where a higher frequency of supercells occurred, while very few were reported in the south where supercell frequency was high. The lack of tornado reports in this region may be unrepresentative, as it falls within a low populated area (Goliger and Lunt, 1997).

The comparison between the supercell distribution and hail distribution (e.g., Dyson et al., 2021; Olivier, 1990) also showed some similarities. High hail day frequency was identified over the Highveld (southern and central parts) of Gauteng and the southern parts of Mpumalanga, where hotspots in supercell activity were also observed in this dissertation. However, the frequency of supercells was low over the south-western parts of Mpumalanga, despite a high hail day frequency in the area, while the supercell hotspot in the south-east did not correspond to a high hail day frequency in the area (values were lower than those in the west).

The spatial distribution of supercells identified in this research, corresponded well with the total and mean number of potentially severe convective environments determined by Blamey et al. (2017), particularly from October onwards (Blamey et al. did not identify many severe convective days for this region in September). This included the eastern Highveld of Gauteng and south-eastern parts of Mpumalanga. However, there is disparity between the results from Blamey et al. (2017) and the supercells identified in this research over south-western Gauteng, where the highest supercell activity was observed for the province. As discussed previously, this region appeared to be significantly influenced by topography. Further, more detailed studies are required to fully understand the relationship between the environment, supercell initiation, track distribution, and demise, especially where areas of favoured activity are found to occur.

Left-moving supercells were found to have a mean track from the south-west to north-east, with very few events travelling from the north-west or south-east. These supercells travelled between

11 and 173 km, although most events travelled less than 60 km, with an average of 49 km. Left-moving supercell speeds ranged between 18 and 84 kmh^{-1} with the average at 41 kmh^{-1}. The fastest 3 left-moving supercell thunderstorms were also found to have a short lifespan of less than 42 minutes, however, other fast-moving events had a longer lifespan or travelled longer distances. Only the study conducted by Christodoulou and Sioutas (2017) for supercells over Greece, included the track speed and distance, while others (e.g., Antonescu et al., 2010; Bunkers et al., 2006a; Hocker and Basara, 2008) did not include this information. The mean supercell speed determined by Christodoulou and Sioutas (2017) was 31.2 kmh^{-1} which was lower than the average speed identified in this research, while their average distance was much greater, at 91.8 km. However, statistics included the entire lifespan of the thunderstorm and not only during the period supercell characteristics were found to occur, as was done in the results presented in this dissertation.

The average distance determined in this dissertation was much further than the average displacement of thunderstorms identified over the Highveld of Gauteng by Mader et al. (1986) (between 1977 and 1984), which was 8 km. In addition, the average speed was greater than the average speed of thunderstorms over the area which was found to be between 27 kmh^{-1} and 30.6 kmh^{-1} for thunderstorms over the Highveld (Mader et al., 1986; Steyn and Bruintjes, 1990). According to Mader et al. (1986) only 20% of the storms considered exceeded a speed of 40 kmh^{-1}.

The supercell's mean south-westerly track direction identified in this research corresponded to the mean track direction of thunderstorms identified over Gauteng (Mader et al., 1986), although as was highlighted by Steyn and Bruintjes (1990) their study included a bias towards the more severe thunderstorm days. Over the north-eastern parts of the Free State thunderstorms exhibited a more west to east track (which included all thunderstorm days over a convective season) (Steyn and Bruintjes, 1990), which corresponds more to the westerly mean environmental wind direction (0 to 6 km) over Gauteng and Mpumalanga (section 3.2).

The mean direction determined in this research corresponds to the mean track directions of supercells found in the USA, Greece and Romania (Antonescu et al., 2010; Bunkers et al., 2006a; Christodoulou and Sioutas, 2017; Hocker and Basara, 2008), although in these regions the north-west to south-east track was also fairly common during certain times within the season. Hocker and Basara (2008) made mention of the synoptic weather patterns as the probable cause for the supercell movement observed over Oklahoma (USA), which also explains the similar track directions observed in this research, since all areas fall within the westerly winds. Left-moving supercells are known to

travel to the left of the mean environmental winds (Browning, 1964; Burgess and Lemon, 1990; Moller et al., 1994). The mean monthly vertical wind profiles over Irene and Ermelo, discussed in section 3.2, shows that winds back with height specifically during the spring and early summer season. The mean environmental wind direction (0 to 6 km) across the warm season was westerly for both areas surrounding Irene and Ermelo (Table 3-1). Thus, the south-west to north-east movement of supercells determined in this study corresponds to a deviation to the left of the mean environmental winds.

A shift in the track direction was observed as the season progressed. In September the mean track (direction from which they travelled from) was west south-westerly, shifting to south-westerly in November, then to southerly in January, and back to south south-westerly in February. Hocker and Basara (2008) also noted a shift in the direction throughout the year for supercells over Oklahoma (USA). The change in track direction identified in the research presented in this dissertation, corresponds to the shift in the mean environmental winds as the season progressed, with a shift from a westerly direction early in the season to a south-westerly over Ermelo and southerly over Irene in (Table 3-1). This was due to the changes in the synoptic conditions, with the upper high shifting southwards, the surface trough shifting east and then west again, while the surface high to the east shifts west and then to the south-east (section 3.2). One observation that the mean environmental winds did not explain was the shift in the track back to south south-westerly in February, with winds only showing a more southerly direction between January and February.

It is important to consider the spatial distribution of the supercells as the season progresses (previously discussed), since activity was the greatest over Gauteng in November and then over south-eastern Mpumalanga in December, January, and February. Thus, the contribution of the mean track direction later in the season was predominantly from those supercells that occurred over Mpumalanga. However, the few supercells that did occur over Gauteng during the latter part of the season, also exhibited this shift in track direction.

6.4 Characteristics of right-moving supercells

Of the 6 right-movers identified, the initiation times occurred between 12:00 and 18:00 UTC and demise times occurred between 13:00 and 19:00 UTC. These times fall within the most active period for the initiation and demise of left-moving supercells. All right-movers were found to be short-lived with an average lifespan of 49 minutes, an average displacement of approximately 47 km and average speed of 61 kmh^{-1}. The longest-lived event was 1 hour 35 minutes, the longest tracked event was approximately 74 km and the fastest moving event travelled with an average speed of 98 kmh^{-1}.

The average lifespan and track distance of the right-movers was lower than those of the left-movers, although not by much but the observed maximums were found to be significantly lower than those of the left-movers. In contrast to this, the average speeds of the right-movers were significantly higher, and contained the fastest moving event for the entire database. When comparing the right-mover events to the left-moving events that occurred on the same day, in some cases the right-movers lasted longer or tracked a longer distance or both. In almost all cases (except 31 December 2019), the right-mover was found to travel at a much faster speed compared to the left-movers on the same day.

Right-movers were found to track from the north-west to south-east with an average of 300°. This differs from the south-west to north-east track observed by the left-moving supercells. Considering the mean environmental winds (0 to 6 km) were found to be westerly (Table 3-1), this track direction was found to agree with literature (e.g., Browning, 1964; Burgess and Lemon, 1990; Moller et al., 1994), whereby right-movers tend to move to the right of the mean environmental winds.

Although some of the statistics were provided and compared to the left-moving supercells, the sample size of the right-movers was very small and thus it is not representative of these types of supercells in the region. As previously mentioned, not all right-moving supercells were necessarily identified (section 3.5 and 6.1) and further studies are required to ensure as many right-moving supercells, as possible, are identified in this region. This may allow for a better sample size to analyse the characteristics of these supercells. None of the studies on supercell characteristics conducted in the USA, Romania or Greece (Antonescu et al., 2010; Bunkers et al., 2006a; Christodoulou and Sioutas, 2017; Hocker and Basara, 2008), separated the left- and right-moving supercell characteristics, and most did not mention if both right- and left-moving supercells were considered in their study.

6.5 Summary

The results of the analysis provided in chapter 4 and 5 were discussed in this chapter, thus answering the 5 research problems posed at the start of this dissertation. This chapter looked at the supercell database and discussed some of the shortfalls in identifying events. It then provided a discussion on the temporal distribution characteristics, the characteristics specific to left-moving supercells and those specific to right-moving supercells. These characteristics were compared to studies of severe thunderstorms in South Africa as well as supercell and other severe thunderstorms around the world. They were also compared to the topography and mean circulation patterns over

South Africa during the warm season, to establish possible explanations for some of the characteristics observed.

Chapter 7: Conclusions and Recommendations

This is the final chapter and starts with the summary and conclusions (section 7.1), where each objective set out at the start of this dissertation is addressed. Following this is a short summary of the limitations and challenges encountered (section 7.2), following by the contributions this research has made to science (section 7.3) and the last section provides the recommendations for future research (section 7.4).

7.1 Summary and Conclusions

The aim of the research set out in this dissertation was to investigate the characteristics of warm season supercell thunderstorms over the Gauteng and Mpumalanga provinces of South Africa, using all available radar data between 2010 and 2020. Characteristics of the warm season supercells were identified by carrying out the 5 objectives set out at the start of this dissertation. It is important to keep in mind that due to the short period of radar data available in this research no long-term climatological conclusions can be drawn and thus the supercell characteristics identified in this research only represent a short-term climatology. In addition, due to various limitations and challenges encountered during the identification of events (summarised in section 7.2), not all events could be identified. Therefore, the characteristics identified in this research, were specific to the database established. However, the results agree with literature and some can be explained by the mean circulation patterns.

The first objective was to create a database of as many supercells as possible during the warm seasons of 2010 to 2020. This was achieved by analysing all available radar data, from the Irene and Ermelo radar, for September to February over the 10-year period. For a thunderstorm to be classified as a supercell it had to contain a hook echo and a WER or BWER on the reflectivity field but if no clear hook echo was present, it had to contain a mesocyclone or mesoanticyclone on the Doppler velocity field. These features had to persist for at least 30 minutes (5 radar scans). This definition was in line with literature and discussed in detail in section 2.3. A database containing 121 supercell events and 67 event days was created, of which 115 were left-moving events and 6 were right-moving events. As anticipated for the region, left-moving supercell frequency was much greater than that for right-moving supercells.

Distance had a significant impact on the identification of events that occurred beyond 100 km from the radar. As was highlighted by Burgess and Lemon (1990) and Donaldson (1970), a radar with an antenna beamwidth of 1° (which is used by both the Irene and Ermelo radar) should be sufficient

to identify supercells up to a 200 km range. More research is required to understand why so few supercells were identified beyond the 100 km range, given the setup of these radars, likely impacting all S-band radars within the SAWS radar network, as they have similar specifications. Forecasters thus need to be aware when using radar data to identify supercells, that identification beyond 100 km will become more challenging and if no other radar data is available, events may likely be missed.

The second objective was achieved by analysing the temporal characteristic of all available supercells identified in the database. On average almost 2 supercell events were found to occur on a given supercell event day. In addition, for the area of Gauteng and Mpumalanga, event days occurred more often in isolation rather than over consecutive days and mass outbreaks were infrequent. Supercells were predominantly found to develop and decay during the afternoon, corresponding to diurnal maximum temperatures, with the peak initiation and demise at around 13:00 and 14:00 UTC respectively. Very few events developed or decayed overnight or during the morning hours. These temporal distributions were found to correspond well to severe thunderstorms and supercell thunderstorms in other regions around the world as well as thunderstorms and severe thunderstorms in South Africa, as was discussed in section 6.2.

No clear temporal trend in the seasonal distribution of the warm season supercells was identified, however, a declining trend was observed over Gauteng in the last 5 seasons. On average approximately 13 events and 7 event days occurred per season. The monthly distribution revealed a more active spring and early summer season with the peak occurring during October and November. There was a shift in the season observed between Gauteng and Mpumalanga. Over Gauteng supercells were found to develop earlier in the season, peaking in October and November. Over Mpumalanga the onset of higher supercell activity only occurred from mid-October, peaking in December, with higher activity during the late summer season, compared to Gauteng. The monthly distribution, was found to correspond well with studies on supercells in other regions around the world and with research on severe thunderstorms in South Africa. This was discussed in section 6.2.

The third objective was to analyse the spatial initiation and demise characteristics. This was achieved by plotting and analysing the initiation and demise locations using QGIS. Due to the low number of points for the given study area, the analysis on the initiation and demise locations was not investigated further with statistical techniques. Hotspots in the initiation of supercells included the southern Gauteng and southern central and south-eastern parts of Mpumalanga, while hotspots in the demise included south-western and north-eastern Gauteng and areas just south and south-east of the Ermelo radar. Over south-western Gauteng and in areas where initiation and demise occurred

near the edge of the Highveld, it appears as if topography had an impact on the life cycle, although further research is required to be able to draw any definitive conclusions.

The fourth objective was achieved by analysing the lifespan of each supercell event and classifying the event as either a short-lived (lasting ≤ 2 hours), moderate-lived (lasting > 2 hours but < 4 hours) or long-lived (lasting ≥ 4 hours). Only 12% of the left-moving supercells were moderate-lived, while the remainder were all short-lived (no long-lived events occurred). On average left-moving supercells lasted 1 hour 12 minutes with most lasting between 30 minutes and 1 hour 30 minutes. All right-moving events were short-lived and lasted on average 49 minutes. The average lifespan and general trend were found to correspond to research in other regions around the world which was discussed in detail in section 6.3. However, one of the most noticeable differences was that no long-lived events were identified within the radar coverage area of this research, compared to all other regions where similar studies were conducted (e.g., Admirat et al., 1985; Bunkers et al., 2006a; Christodoulou and Sioutas, 2017; Hocker and Basara, 2008).

The fifth objective was to analyse the track characteristics. The track information for each event was obtained using a hybrid approach. The TITAN algorithm (which forms part of the LROSE software) was predominantly used to obtain the centroid position of each supercell for the relevant time steps, but where automatic tracking was not optimal, manual positions were obtained. The track distance was calculated in QGIS and the bearing between the initiation and demise location was calculated to obtain the track direction. The average speed was calculated using the track distance and the lifespan. In addition, a KDE analysis using GIS was performed on the left-moving supercell tracks to obtain the spatial distribution. Left-moving supercells travelled on average approximately 49 km with an average speed of 41 kmh^{-1} and right-movers travelled on average 22 km with a speed of 61 kmh^{-1}. The mean track direction for left-movers was from south-west to north-east, while right-movers had a mean track direction from the north-west to south-east. As expected, the left-moving events deviated to the left and right-movers to the right of the mean environmental winds. A shift in the track direction for left-moving supercells was also observed as the season progressed, which is likely due to the change in the mean environmental winds. The track direction was from the west south-west earlier in the season and then south to north by the mid to late summer season and then from the south south-west by the end of the warm season. The track direction characteristics and seasonal changes were also found to correspond well to supercells in other regions, discussed in section 6.3.

The spatial distribution of left-moving supercells showed to have areas of highest activity over parts of the southern Gauteng and southern central and south-eastern Mpumalanga. Areas of

moderate activity were also observed over north-western Gauteng, areas along the Highveld over eastern Gauteng as well as areas west of the Ermelo radar. Topography appeared to play a role in the distribution of events over south-western Gauteng and along the Highveld over eastern Gauteng, as well as in the lower lying areas over south-eastern Mpumalanga. However, as previously mentioned a more detailed analysis is required to confirm this, as well as for areas with no obvious relationship (topography or otherwise). An area of low to no activity was observed in places over western Mpumalanga but no explanation to why this occurred could be provided in this research.

The spatial distribution also saw a shift as the season progressed. Activity starting over the southern Highveld early in the season, spreading northwards by October and then decreasing in the west and increasing in the south-east in December. This seasonal shift was found to correspond to the seasonal shift in the number of potentially severe convective days discussed in more detail in section 6.2.2.

7.2 Limitations and challenges

Several limitations and challenges were encountered during the research presented in this dissertation. Most of these limitations had an impact on the database and was discussed in detail in chapter 3 as well as in section 6.1.1. Below is a short summary of the limitations and challenges encountered:

- Radar data availability was one of the major limitations for supercell event identification. For both radars the 2012-2013 season was predominantly not available and no supercells were identified. Therefore, although data was available from 2010, supercells were only identified during 9 warm seasons. In general, the Ermelo radar was impacted the most, where low availability resulted in either no or very few events being identified during 3 seasons prior to 2015-2016.
- Distance from the radar was also a significant limiting factor for supercell identification. All events were found to occur within 150 km of the radar with the majority occurring within 100 km. Resolution was likely the main cause, however the height of the radar beam as well as the impact distance has on the shape of the doppler velocity features may also have played a role.
- The Nyquist velocity may also have played a role in the identification of the mesocyclone (anticyclone) as velocity folding may easily occur, in the areas of the rotating updraft, if this is set too low.

- Difficulties in identifying the mesocyclone (anticyclone) on the Doppler velocity field, due to motion of the storm, circulation patterns in and around the updraft as well as the orientation and distance of the feature to the radar may have resulted in the non-identification of the less classic supercell events.
- Although the method used in this research to identify supercells follows a similar approach used by various other studies, the method was still subjective. Not all thunderstorms were analysed on the Doppler velocity field, and unless a thunderstorm exhibited certain characteristics (e.g., high reflectivity, deviation, contained an inflow notch etc.) it was not necessarily investigated in detail. This may have led to the identification of the predominantly more classic supercells rather than all events.
- Since the left-moving supercells were more common in this region and were easier to identify as a result, the focus tended more towards the identification of these events. Thus, it is likely that not all right-moving supercells were identified. It was also noted that the right-moving supercells lacked the classic hook echo in most cases thus the mesoanticyclone became an important component in their identification. Since the Doppler velocity was not always consulted and due to some of the limitations of the Doppler velocity field, events may have been missed.

7.3 Contributions to science

The radar derived supercell thunderstorm database created in this research is the first for South Africa. There has been a lack of research on supercells in South Africa up until now, which in part may be due the fact that no database previously existed. Therefore, this database is a contribution to science as it provides many opportunities for future research in the field of severe thunderstorms and supercell thunderstorms in South Africa.

Given that so little research has been undertaken on supercell thunderstorms in South Africa, the results presented in this dissertation have thus provided the first short-term characteristics of supercells over the Gauteng and Mpumalanga provinces. This knowledge will be able to assist forecasters in forecasting, nowcasting and warning for these thunderstorms in the region. Knowledge about the time of day and months these events are more likely to occur may provide awareness during these periods. Understanding their track direction and which areas are more prone to their development, demise, and track and how the spatial distribution changes throughout the season, may again provide awareness when analysing the radar data for supercell identification. The lifespan and

track distance may also be useful during decision making and warning given the average time supercells tend to last and average distance they tend to travel.

Although some of the characteristics of supercells discussed in this dissertation could be explained by the mean synoptic conditions and environment, a lot more research is required to fully understand these observed characteristics. The research in this dissertation has thus provided the foundation on which numerous other studies can be based, to understand why these characteristics occur and to develop improved forecasting techniques.

7.4 Recommendations for future research

Up until now very little research has been conducted on supercells in South Africa, therefore the opportunities for future research within this field are numerous, more so now that a relatively large database is available. The following list provides some of the recommendations identified because of the work done in this dissertation:

1. With most events occurring within 100 km from each radar, using other available radar data from surrounding areas (e.g., Polokwane, Ottosdal, Bloemfontein, Bethlehem (although was not operational for several years) and Durban) may help to expand on the current database and improve the detection of events that occurred outside of the 100 to 150 km range. In general, all available data from the SAWS radar network needs to be analysed to expand this database thereby including most of South Africa. This would also allow for more definite conclusions on some of the characteristics such as the frequency of mass outbreak events, events occurring on consecutive days, etc.
2. Although availability was addressed in this research, details on their impact on supercell identification was not investigated. This may include determining if thunderstorms occurred during the time of no data availability and if so, was the environment conducive to supercell development. This could be an area for future research thereby improving the confidence in the database produced in the research presented in this dissertation.
3. Considering so few right-moving supercell events were identified, which may have been due to the methodology used in this research, a study to specifically identify as many right-moving supercells within this study area or South Africa, needs to be conducted.
4. An alternative more objective method to identify supercell thunderstorms within this region may need to be developed to capture the less classic events. The use of an

automatic mesocyclone detection algorithm may need to be investigated, which could be adapted for the region using the database created in this dissertation.

5. Alternative methods of supercell identification (such as satellite data, visual observations etc.) may need to be investigated to supplement this database, where availability and coverage impacts the identification of events.
6. Supercells are known to produce damaging severe weather, however, the frequency at which supercells produce this compared to other severe thunderstorms, and the frequency of the type of severe weather they may produce is unknown. This is another area for further research.
7. Investigating the environment and synoptic weather systems that result in supercell thunderstorms over Gauteng and Mpumalanga is another very important study that needs to be conducted. This can be achieved using the database provided in this research. The focus would not only be to identify the type of weather systems or environment required but also to understand why certain characteristics occur (e.g., the higher activity observed over Gauteng in November compared to Mpumalanga, the observed seasonal changes in the distribution, the general distribution patterns observed etc.).
8. A more comprehensive study to investigate the lack of long-lived and/or low frequency of moderate-lived supercell events over Gauteng and Mpumalanga needs to be conducted. This needs to include an investigation to ensure radar limitations were not the cause and then examine the environment and topography to determine the influence they may have had. The study done by Bunkers et al. (2006b) may be useful in this recommended study as it investigates the environmental conditions and forecasting application for long-lived supercells.
9. A comprehensive and statistical study is required to determine the topographical influence on supercell initiation, track, and demise. Some interesting areas to focus on would include the south-western parts of Gauteng, areas along the highveld and then the low-lying areas north of the Magaliesberg mountain and south-eastern parts of Mpumalanga. The research done by Markowski and Dotzek (2011) and Prociv (2012) investigating the relationship between topography and supercells may be useful in this potential study.
10. The area of very low activity that was identified over the north-western parts of the Ermelo radar needs to be investigated further, to understand why this occurred. Neither the topography nor the radar limitations provide an explanation for this low activity area but these along with other factors would need to be investigated in more detail.

11. Studies addressing the possible link between supercell development and rainfall variability needs to be conducted. It was noted that supercell frequency was still high during periods where drought conditions were prevailing over the region.
12. All lifespan, track, initiation, and demise characteristics analysed in this dissertation were based on the supercell and did not include the pre and post thunderstorm characteristics. These characteristics were considered by other studies (e.g., Bunkers et al., 2006a; Hocker and Basara, 2008) and included the time it took for supercell features to develop, how long the thunderstorm lasted after supercell features dissipated. Thus, this would be another area for future research.
13. Other studies examining supercell characteristics (Bunkers et al., 2006a; Christodoulou and Sioutas, 2017) such as the reasons for supercell demise (e.g., it experiences a merger with other thunderstorms or developed into a bow echo), if supercells occurred in isolation or not and the convective mode. This would be another area for further studies along with the analysis of other radar-derived characteristics such as maximum radar reflectivity, velocity, storm tops, etc. This may further enhance the knowledge on supercells within the region.
14. The KDE analysis, conducted in this research, to identify the spatial distribution of the left-moving supercells, only considered the vector path (track) based on the centroid position of the thunderstorm and not the entire area that may have resulted in damaging weather conditions at the surface. Hocker and Basara (2008) created a conservative 5 km buffer (10 km diameter) around their supercell vector paths to try and account for the swath of possible influence at the surface (swath). A similar study could be carried out, however, the database identified in this research could be used to determine an appropriate buffer size by measuring and obtaining an average echo size for supercells in the region and then to apply this buffer before conducting the KDE analysis.

REFERENCES

ADLERMAN, E. J., DROEGEMEIER, K. K. & DAVIES-JONES, R. 1999. A numerical simulation of cyclic mesocyclogenesis. *Journal of the atmospheric sciences, 56*(13), pp. 2045-2069.

ADMIRAT, P., GOYER, G. G., WOJTIW, L., CARTE, E. A., ROOS, D. & LOZOWKI, E. P. 1985. A comparative study of hailstorms in Switzerland, Canada and South Africa. *Journal of Climatology, 5*(1), pp. 35-51. doi:10.1002/joc.3370050104

ALLEN, J. 2012. Supercell storms: Melbourne's white Christmas 2011. *Bull. Aust. Meteor. Oceanogr. Soc, 25*, pp. 47-51.

ANTONESCU, B., CARBUNARU, D., SASU, M., BURCEA, S. & BELL, A. 2010. A Climatology of supercells in Romania. Proceedings of the 6th European Conference on Radar in Meteorology and Hydrology: Advances in Radar Technology (ERAD2010), 6-10 September 2010. Sibiu, Romania,Available: http://erad2010.com/pdf/oral/wednesday/mesoscale/05_ERAD2010_0007.pdf.

BECK, J. R., SCHROEDER, J. L. & WURMAN, J. M. 2006. High-resolution dual-Doppler analyses of the 29 May 2001 Kress, Texas, cyclic supercell. *Monthly weather review, 134*(11), pp. 3125-3148.

BECKER, E. H. 2014. *Application of a quantitative precipitation estimation algorithm for the s-band radar at Irene, South Africa.* Msc Dissertation, Available: https://researchspace.ukzn.ac.za/handle/10413/12795.

BLAMEY, R., KOLUSU, S., MAHLALELA, P., TODD, M. & REASON, C. 2018. The role of regional circulation features in regulating El Niño climate impacts over southern Africa: A comparison of the 2015/2016 drought with previous events. *International Journal of Climatology, 38*(11), pp. 4276-4295.

BLAMEY, R. C., MIDDLETON, C., LENNARD, C. & REASON, C. J. C. 2017. A climatology of potential severe convective environments across South Africa. *Climate Dynamics, 49*(5), pp. 2161-2178. doi:10.1007/s00382-016-3434-7

BLUESTEIN, H. B. & WEISMAN, M. L. 2000. The Interaction of Numerically Simulated Supercells Initiated along Lines. *Monthly Weather Review, 128*(9), pp. 3128-3149. doi:10.1175/1520-0493(2000)128<3128:TIONSS>2.0.CO;2

BLUESTEIN, H. B. & WOODALL, G. R. 1990. Doppler-Radar Analysis of a Low-Precipitation Severe Storm. *Monthly Weather Review, 118*(8), pp. 1640-1665. doi:10.1175/1520-0493(1990)118<1640:DRAOAL>2.0.CO;2

BROOKS, H. E. 2009. Proximity soundings for severe convection for Europe and the United States from reanalysis data. *Atmospheric Research, 93*(1-3), pp. 546-553.

BROOKS, H. E., LEE, J. W. & CRAVEN, J. P. 2003. The spatial distribution of severe thunderstorm and tornado environments from global reanalysis data. *Atmospheric Research, 67*, pp. 73-94.

BROWN, R. A. & WOOD, V. T. 2007. A Guide for Interpreting Doppler Velocity Patterns: Northern Hemisphere Edition. *NOAA/National Severe Storms Laboratory*.

BROWN, R. A., WOOD, V. T. & SIRMANS, D. 2002. Improved tornado detection using simulated and actual WSR-88D data with enhanced resolution. *Journal of Atmospheric and Oceanic Technology, 19*(11), pp. 1759-1771.

BROWNING, K. A. 1964. Airflow and Precipitation Trajectories Within Severe Local Storms Which Travel to the Right of the Winds. *Journal of the Atmospheric Sciences, 21*(6), pp. 634-639. doi:10.1175/1520-0469(1964)021<0634:AAPTWS>2.0.CO;2

BUNKERS, M. J., HJELMFELT, M. R. & SMITH, P. L. 2006a. An Observational Examination of Long-Lived Supercells. Part I: Characteristics, Evolution, and Demise. *Weather and Forecasting, 21*(5), pp. 673-688. doi:10.1175/WAF949.1

BUNKERS, M. J., JOHNSON, J. S., CZEPYHA, L. J., GRZYWACZ, J. M., KLIMOWSKI, B. A. & HJELMFELT, M. R. 2006b. An observational examination of long-lived supercells. Part II: Environmental conditions and forecasting. *Weather and forecasting, 21*(5), pp. 689-714.

BUNKERS, M. J., KLIMOWSKI, B. A., ZEITLER, J. W., THOMPSON, R. L. & WEISMAN, M. L. 2000. Predicting Supercell Motion Using a New Hodograph Technique. *Weather and forecasting, 15*(1), pp. 61-79. doi:10.1175/1520-0434(2000)0152.0.CO;2

BURGESS, D. W. & DAVIES-JONES, R. P. 1979. Unusual Tornadic Storms in Eastern Oklahoma on 5 December 1975. *Monthly Weather Review, 107*(4), pp. 451-457. doi:10.1175/1520-0493(1979)107<0451:UTSIEO>2.0.CO;2

BURGESS, D. W. & LEMON, L. R. 1990. Severe Thunderstorm Detection by Radar. *In:* ATLAS, D. (ed.) *Radar in Meteorology: Battan Memorial and 40th Anniversary Radar Meteorology Conference.* Boston, MA: American Meteorological Society.

BURKE, P. C. & SCHULTZ, D. M. 2004. A 4-Yr Climatology of Cold-Season Bow Echoes over the Continental United States. *Weather and Forecasting, 19*(6), pp. 1061-1074. doi:10.1175/811.1

CARTE, A. E. 1979. Sustained Storms on the Transvaal Highveld. *South African Geographical Journal, 61*(1), pp. 39-56. doi:10.1080/03736245.1979.10559604

CARTE, A. E. 1981. Morphology of Persistent Storms in the Transvaal on 16/17 October 1978. *Beitrage zur Physik der Atmosphäre, 54*(1), pp. 86-100.

CARTE, A. E. & HELD, G. 1978. Variability of Hailstorms on the South African Plateau. *Journal of Applied Meteorology, 17*(3), pp. 365-373. doi:10.1175/1520-0450(1978)017<0365:VOHOTS>2.0.CO;2

CHIKOORE, H. & JURY, M. R. 2021. South African drought, deconstructed. *Weather and Climate Extremes*, pp. 100334.

CHRISTODOULOU, M. & SIOUTAS, M. 2017. Radar Climatology of Supercell Thunderstorms in Northern and Central Greece. *Perspectives on Atmospheric Sciences.* Springer.

DAVIES-JONES, R. 1984. Streamwise vorticity: The origin of updraft rotation in supercell storms. *Journal of Atmospheric Sciences, 41*(20), pp. 2991-3006.

DAVIES-JONES, R. P. 2006. Tornadogenesis in supercell storms what we know and what we don't know. Proceeding of the Symposium on the challenges of Severe Convective Storms, 28 January - 2 February 2006. Atlanta USA: American Meteorological Society,Available: https://ams.confex.com/ams/Annual2006/techprogram/paper_104563.htm.

DE CONING, E., ADAM, E. & BENITZ, B. F. 2000. A severe weather event on 29 December 1997: Synoptic and mesoscale perspectives. *Water SA, 26*(2), pp. 137-146.

DIXON, M. & JAVORNIK, B. 2016. *Lidar Radar Open Software Environment (LROSE) Core Software* [Online]. UCAR/NCAR - Earth Observing Laboratory. Available: https://github.com/ncar/lrose-core [Accessed 8 August 2021].

DIXON, M. & SEED, A. 2014. Developments in echo tracking-enhancing TITAN. Proceedings of the 8th European Conference on Radar in Meteorology and Hydrology (ERAD2014), 1-5 September 2014 Garmisch-Partenkirchen, Germany.

DIXON, M. & WIENER, G. 1993. TITAN: Thunderstorm Identification, Tracking, Analysis, and Nowcasting—A Radar-based Methodology. *Journal of Atmospheric and Oceanic Technology, 10*, pp. 785-797. doi:10.1175/1520-0426(1993)010<0785:TTITAA>2.0.CO;2

DONALDSON, R. J. 1970. Vortex Signature Recognition by a Doppler Radar. *Journal of Applied Meteorology (1962-1982), 9*(4), pp. 661-670.

DOSWELL III, C. A. 2001. Severe Convective Storms - An Overview. *Severe Convective Storms.* 1 ed. Boston, MA: American Meteorological Society.

DOSWELL III, C. A. & BURGESS, D. W. 1993. Tornadoes and tornadic storms: A review of conceptual models. *Geophysical Monograph-American Geophysical Union, 79*, pp. 161-172. doi:10.1029/GM079p0161

DOSWELL III, C. A. & SCHULTZ, D. M. 2006. On the Use of Indices and Parameters in Forecasting Severe Storms. *E-Journal of Severe Storms Meteorology, 1*(3).

DOVIAK, R. J. & ZRNIC, D. S. 1993. *Doppler Radar and Weather Observations,* San Diego, California, Academic Press, Inc.

DROEGEMEIER, K. K., LAZARUS, S. M. & DAVIES-JONES, R. 1993. The Influence of Helicity on Numerically Simulated Convective Storms. *Monthly Weather Review, 121*(7), pp. 2005-2029. doi:10.1175/1520-0493(1993)121<2005:TIOHON>2.0.CO;2

DYSON, L. L., HEERDEN, J. V. & SUMNER, P. D. 2015. A baseline climatology of sounding-derived parameters associated with heavy rainfall over Gauteng, South Africa. *International Journal of Climatology, 35*(1), pp. 114-127. doi:10.1002/joc.3967

DYSON, L. L., PIENAAR, N., SMIT, A. & KIJKO, A. 2021. An ERA-Interim HAILCAST hail climatology for southern Africa. *International Journal of Climatology, 41*(1), pp. 262-277.

FALK, K. W. 1997. Techniques for Issuing Severe Thunderstorm and Tornado warnings with the WSR-88D Doppler Radar. NOAA.

FELDMANN, M., GERMANN, U., GABELLA, M. & BERNE, A. 2021. A characterisation of Alpine mesocyclone occurrence. *Weather and Climate Dynamics, 2*(4), pp. 1225-1244.

FORESTI, L., SIDERIS, I. V., PANZIERA, L., NERINI, D. & GERMANN, U. 2018. A 10-year radar-based analysis of orographic precipitation growth and decay patterns over the Swiss Alpine region. *Quarterly Journal of the Royal Meteorological Society, 144*(716), pp. 2277-2301.

FRENCH, M. M., BLUESTEIN, H. B., DOWELL, D. C., WICKER, L. J., KRAMAR, M. R. & PAZMANY, A. L. 2008. High-resolution, mobile Doppler radar observations of cyclic mesocyclogenesis in a supercell. *Monthly Weather Review, 136*(12), pp. 4997-5016.

GIJBEN, M. 2012. The lightning climatology of South Africa. *South African Journal of Science, 108*(3-4), pp. 44-53.

GIJBEN, M. 2016. *A lightning threat index for South Africa using numerical weather prediction data.* Msc Dissertation, University of PretoriaAvailable: https://repository.up.ac.za/handle/2263/57242.

GILL, T. 2009. *Initial steps in the development of a comprehensive lightning climatology of South Africa.* Master of Science Dissertation, Available: http://wiredspace.wits.ac.za/handle/10539/7077.

GOLIGER, A. & LUNT, B. G. 1997. *Inkanyamba: tornadoes in South Africa,* South Africa, CSIR, Building Technology :Weather Bureau.

GOLIGER, A. M. & RETIEF, J. V. 2007. Severe wind phenomena in Southern Africa and the related damage. *Journal of Wind Engineering and Industrial Aerodynamics, 95*(9), pp. 1065-1078. doi:10.1016/j.jweia.2007.01.029

GRANT, L. D. & VAN DEN HEEVER, S. C. 2014. Microphysical and Dynamical Characteristics of Low-Precipitation and Classic Supercells. *Journal of the Atmospheric Sciences, 71*(7), pp. 2604-2624. doi:10.1175/JAS-D-13-0261.1

HELD, G. & CARTE, A. E. 1979. Hailstorms in the Transvaal During January 1975. *South African Geographical Journal, 61*(2), pp. 128-142. doi:10.1080/03736245.1979.10559613

HELD, G., GOMES, A. & NACCARATO, K. 2010. The structure and behaviour of supercell storms in the State of São Paulo, Brazil. Proceedings of the 6th European Conference on Radar in Meteorology and Hydrology, (ERAD2010), 6-10 September 2010 Sibiu, Romania.

HOCKER, J. E. & BASARA, J. B. 2008. A Geographic Information Systems–Based Analysis of Supercells across Oklahoma from 1994 to 2003. *Journal of Applied Meteorology and Climatology, 47*(5), pp. 1518-1538. doi:10.1175/2007JAMC1673.1

HOLLEMAN, I. & BEEKHUIS, H. 2003. Analysis and Correction of Dual PRF Velocity Data. *Journal of Atmospheric and Oceanic Technology, 20*(4), pp. 443-453. doi:10.1175/1520-0426(2003)20<443:AACODP>2.0.CO;2

HOUZE, R. A. 1993. *Cloud dynamics,* San Diego, Academic Press.

JOE, P. & MAY, P. T. 2003. Correction of Dual PRF Velocity Errors for Operational Doppler Weather Radars. *Journal of Atmospheric and Oceanic Technology, 20*(4), pp. 429-442. doi:10.1175/1520-0426(2003)20<429:CODPVE>2.0.CO;2

JOHNS, R. H. & DOSWELL III, C. A. 1992. Severe Local Storms Forecasting. *Weather and Forecasting, 7*(4), pp. 588-612. doi:10.1175/1520-0434(1992)007<0588:SLSF>2.0.CO;2

KANAMITSU, M., EBISUZAKI, W., WOOLLEN, J., YANG, S.-K., HNILO, J., FIORINO, M. & POTTER, G. 2002. Ncep–doe amip-ii reanalysis (r-2). *Bulletin of the American Meteorological Society, 83*(11), pp. 1631-1644.

KLEMP, J. B. 1987. Dynamics of Tornadic Thunderstorms. *Annual Review of Fluid Mechanics, 19*(1), pp. 369-402. doi:10.1146/annurev.fl.19.010187.002101

KLEMP, J. B. & WILHELMSON, R. B. 1978. The Simulation of Three-Dimensional Convective Storm Dynamics. *Journal of the Atmospheric Sciences, 35*(6), pp. 1070-1096. doi:10.1175/1520-0469(1978)035<1070:TSOTDC>2.0.CO;2

KLIMOWSKI, B. A., BUNKERS, M. J., HJELMFELT, M. R. & COVERT, J. N. 2003. Severe Convective Windstorms over the Northern High Plains of the United States. *Weather & Forecasting, 18*(3), pp. 502. doi:10.1175/1520-0434(2003)18<502:SCWOTN>2.0.CO;2

KRUGER, A., RAE, K. & MCBRIDE, C. 2018. *Summary of 2017 Climate and Significant Weather Events* [Online]. Available: http://www.weathersa.co.za/Documents/Corporate/Newsletter_May.pdf [Accessed 28 January 2020].

LEKOLOANE, L. E., BOPAPE, M.-J. M., RAMBUWANI, T. G., NDARANA, T., LANDMAN, S., MOFOKENG, P., GIJBEN, M. & MOHALE, N. 2021. A dynamic and thermodynamic analysis of the 11 December 2017 tornadic supercell in the Highveld of South Africa. *Weather and Climate Dynamics, 2*(2), pp. 373-393.

LEMON, L. R. 1977. New Severe Thunderstorm Radar Identification Techniques and Warning Criteria: A preliminary report. Kansas City, Missouri: U.S. Department of Commerce, National Oceanic and Atmospheric Administration, National Weather Service.

LEMON, L. R., BURGESS, D. W. & BROWN, R. A. 1978. Tornadic Storm Airflow and Morphology Derived from Single-Doppler Radar Measurements. *Monthly Weather Review, 106*(1), pp. 48-61. doi:10.1175/1520-0493(1978)106<0048:TSAAMD>2.0.CO;2

LEMON, L. R. & DOSWELL III, C. A. 1979. Severe Thunderstorm Evolution and Mesocyclone Structure as Related to Tornadogenesis. *Monthly Weather Review, 107*(9), pp. 1184-1197. doi:10.1175/1520-0493(1979)107<1184:STEAMS>2.0.CO;2

LUKACH, M., FORESTI, L., GIOT, O. & DELOBBE, L. 2017. Estimating the occurrence and severity of hail based on 10 years of observations from weather radar in Belgium. *Meteorological Applications, 24*(2), pp. 250-259.

MADER, G. N., NEISHLOS, H., SAUNDERS, M. M. & CARTE, A. E. 1986. Some characteristics of storms on the transvaal highveld. *Journal of Climatology, 6*(2), pp. 173-182. doi:10.1002/joc.3370060206

MARKOWSKI, P. M. 2002. Hook Echoes and Rear-Flank Downdrafts: A Review. *Monthly Weather Review, 130*(4), pp. 852-876. doi:10.1175/1520-0493(2002)130<0852:HEARFD>2.0.CO;2

MARKOWSKI, P. M. & DOTZEK, N. 2011. A numerical study of the effects of orography on supercells. *Atmospheric research, 100*(4), pp. 457-478.

MILRAD, S. 2017. *Synoptic Analysis and Forecasting: An Introductory Toolkit,* Saint Louis, USA, Elsevier.

MITTERMAIER, M. P. & TERBLANCHE, D. E. 1997. Converting weather radar data to Cartesian space : A new approach using DISPLACE averaging. *Converting weather radar data to Cartesian space : A new approach using DISPLACE averaging, 23*(1), pp. 45-50.

MODIKA, J. 2020. *Taaiboschspruit Farm (Panbult) Tornado: Mpumalanga* [Online]. Pretoria: South African Weather Service. Available: https://www.weathersa.co.za/Documents/Corporate/Medrel%206%20Jan%202020.pdf [Accessed 6 January 2020].

MOLLER, A. R., DOSWELL III, C. A., FOSTER, M. P. & WOODALL, G. R. 1994. The Operational Recognition of Supercell Thunderstorm Environments and Storm Structures. *Weather and Forecasting, 9*(3), pp. 327-347. doi:10.1175/1520-0434(1994)009<0327:TOROST>2.0.CO;2

MOLLER, A. R., DOSWELL III, C. A. & PRZBYLINSKI, R. 1990. High-precipitation supercells: A conceptual model and documentation. Preprints 16th Conference on Severe Local Storms, 22-26 October 1990 Alberta, Canada. Kananaskis Park, Alberta, Canada: American Meteorological Society,Available: http://www.flame.org/~cdoswell/publications/Moller_etal_16thSLS.pdf.

NELSON, S. P. 1987. The Hybrid Multicellular–Supercellular Storm—an Efficient Hail Producer. Part II. General Characteristics and Implications for Hail Growth. *Journal of the Atmospheric Sciences, 44*(15), pp. 2060-2073. doi:10.1175/1520-0469(1987)044<2060:THMSEH>2.0.CO;2

NELSON, S. P. & KNIGHT, N. C. 1987. The Hybrid Multicellular–Supercellular Storm—an Efficient Hail Producer. Part I: An Archetypal Example. *Journal of the Atmospheric Sciences, 44*(15), pp. 2042-2059. doi:10.1175/1520-0469(1987)044<2042:THMSEH>2.0.CO;2

OLIVIER, J. 1990. *Hail in the Transvaal: Some Geographical and climatological aspects.* PhD Thesis, Rand Afrikaans University.

PIENAAR, N., DYSON, L. & KLOPPER, E. 2015. Atmospheric anomalies during the 2012/13 extreme hail seasons over Gauteng. Proceeding of the 31st Annual Conference of Conference of South African Society for Atmosperic Science, 21-22 September 2015 Hennops River Valley, South Africa. Hennops River Valley, South Africa: SASAS,Available: https://www.researchgate.net/publication/324223684_Atmospheric_anomalies_during_the_201213_extreme_hail_seasons_over_Gauteng.

POWELL, C. L. 2013. Characteristics of hailstorms over the Highveld of South Africa. Proceedings of the 29th Annual Conference of South African Society for Atmospheric Sciences, 26 - 27 September 2013 Durban, South Africa. SASAS,Available: http://sasas.ukzn.ac.za/Libraries/DOWNLOAD/SASAS_2013_Peer_Reviewed_Conference_Proceedings_3.sflb.ashx.

POWELL, C. L. & BURGER, R. P. 2014. The severe Gauteng hailstorms of 28 November 2013. 30th Conference of South African Society for Atmospheric Sciences, 1 - 2 October 2014 Potchefstroom, South Africa. SASAS,Available: http://dspace.nwu.ac.za/handle/10394/16144?show=full.

PROCIV, K. A. 2012. *Terrain and landcover effects of the southern Appalachian Mountains on the low-level rotational wind fields of supercell thunderstorms.* MSc Dissertation, Virginia Tech.

RAE, K. J. 2014. *A modified Supercell Composite Parameter for supercell thunderstorms over the Gauteng Province, South Africa.* Msc Dissertation, University of PretoriaAvailable: https://repository.up.ac.za/bitstream/2263/45918/1/Rae_Modified_2015.pdf.

RASMUSSEN, E. N. & WILHELMSON, R. B. 1983. Relationships between storm characteristics and 1200 GMT hodographs, low-level shear, and stability. Proceeding of the 13th Conference on Severe Local Storms, 1983. Tulsa, Oklahoma: American Meteorological Society,Available: https://ci.nii.ac.jp/naid/10020789185.

RAUBER, R. M. & NESBITT, S. W. 2018. *Radar Meteorology: A First Course,* Hoboken, NJ, John Wiley & Sons.

RAUHALA, J., BROOKS, H. E. & SCHULTZ, D. M. 2012. Tornado climatology of Finland. *Monthly weather review, 140*(5), pp. 1446-1456.

RAY, P. 1990. Convective Dynamics. *In:* ATLAS, D. (ed.) *Radar in Meteorology: Battan Memorial and 40th Anniversary Radar Meteorology Conference.* Boston, MA: American Meteorological Society.

RINEHART, R. E. 2010. *Radar for Meteorologists,* Nevada Missouri, Rinehart Publications.

SAWS 2011. Climate Summary of South Africa: October 2011. *22*(10).

SAWS 2013. Climate Summary of South Africa: November 2013. *24*(11).

SAWS 2015. Climate Summary of South Africa: November 2015. *26*(11).

SAWS 2017. Climate Summary of South Africa: December 2017. *28*(12).

SCHULZE, R. E. & MAHARAJ, M. 2007. Rainfall Seasonality. *In:* SCHULZE, R. E. (ed.) *South African Atlas of Climatology and Agrohydrology: WRC Report 1489/1/06* Pretoria, South Africa: Water Research Commission.

SEBEGO, E. & RAE, K. 2017. *Severe thunderstorms Wreak havoc in Gauteng on 9 October 2017; further warnings for KwaZulu Natal and Eastern Cape on 10 October 2017* [Online]. Pretoria: South African Weather Service. Available: https://www.weathersa.co.za/Documents/Corporate/Medrel%2010a%20October%202017.pdf [Accessed 28 January 2020].

SELEXES-GEMATRONIK 2014. Software Manual Rainbow®5 user guide, release 5.40.0. Neuss, Germany: Selex ES GmbH.

SIMPSON, L.-A. & DYSON, L. L. 2018. Severe weather over the Highveld of South Africa during November 2016. *Water SA, 44*(1), pp. 75-85.

STEYN, R. T. & BRUINTJES, P. C. L. A. 1990. Convective cloud characteristics for the Bethlehem area. *Water SA, 16*(2), pp. 115-118.

STUMPF, G. J., WITT, A., MITCHELL, E. D., SPENCER, P. L., JOHNSON, J. T., EILTS, M. D., THOMAS, K. W. & BURGESS, D. W. 1998. The National Severe Storms Laboratory Mesocyclone Detection Algorithm for the WSR-88D. *Weather and Forecasting, 13*(2), pp. 304-326. doi:10.1175/1520-0434(1998)013<0304:TNSSLM>2.0.CO;2

TALJAARD, J. J. 1994. *Atmospheric circulation systems, synoptic climatology and weather phenomena of South Africa. Part 1 Controls of the Weather and Climate of South Africa,* Pretoria, South African Weather Bureau.

TASZAREK, M., ALLEN, J. T., MARCHIO, M. & BROOKS, H. E. 2021. Global climatology and trends in convective environments from ERA5 and rawinsonde data. *npj Climate and Atmospheric Science, 4*(1), pp. 1-11.

TASZAREK, M. & BROOKS, H. E. 2015. Tornado climatology of Poland. *Monthly Weather Review, 143*(3), pp. 702-717.

U. S. Geological Survey. 2000. *EROS Archive - Digital Elevation - Shuttle Radar Topography Mission (SRTM) Non-Void Filled* [Online]. Available: https://doi.org/10.5066/F7K072R7 [Accessed 18 March 2021].

VASILOFF, S. V., BRANDES, E. A., DAVIES-JONES, R. P. & RAY, P. S. 1986. An Investigation of the Transition from Multicell to Supercell Storms. *Journal of Climate and Applied Meteorology, 25*(7), pp. 1022-1036. doi:10.1175/1520-0450(1986)025<1022:AIOTTF>2.0.CO;2

WALDVOGEL, A., FEDERER, B. & GRIMM, P. 1979. Criteria for the detection of hail cells. *Journal of Applied Meteorology and Climatology, 18*(12), pp. 1521-1525. doi:https://doi.org/10.1175/1520-0450(1979)018<1521:CFTDOH>2.0.CO;2

WEISMAN, M. L. & KLEMP, J. B. 1982. The Dependence of Numerically Simulated Convective Storms on Vertical Wind Shear and Buoyancy. *Monthly Weather Review, 110*(6), pp. 504-520. doi:10.1175/1520-0493(1982)110<0504:TDONSC>2.0.CO;2

WEISMAN, M. L. & KLEMP, J. B. 1984. The Structure and Classification of Numerically Simulated Convective Storms in Directionally Varying Wind Shears. *Monthly Weather Review, 112*(12), pp. 2479-2498. doi:10.1175/1520-0493(1984)112<2479:TSACON>2.0.CO;2

WEISMAN, M. L. & KLEMP, J. B. 1986. Characteristics of Isolated Convective Storms. *In:* RAY, P. S. (ed.) *Mesoscale Meteorology and Forecasting.* Boston, MA: American Meteorological Society.

WEISMAN, M. L. & ROTUNNO, R. 2000. The Use of Vertical Wind Shear versus Helicity in Interpreting Supercell Dynamics. *Journal of the Atmospheric Sciences, 57*(9), pp. 1452-1472. doi:10.1175/1520-0469(2000)057<1452:TUOVWS>2.0.CO;2

WILHELMSON, R. B. & KLEMP, J. B. 1978. A Numerical Study of Storm Splitting that Leads to Long-Lived Storms. *Journal of the Atmospheric Sciences, 35*(10), pp. 1974-1986. doi:10.1175/1520-0469(1978)035<1974:ANSOSS>2.0.CO;2

WMO. 2018. *Guide to Instruments and Methods of Observation. In Volume III - Observing Systems* [Online]. Geneva, Switzerland: World Metoerological Organization (WMO). Available: https://library.wmo.int/doc_num.php?explnum_id=9872 [Accessed 15 October 2021].

Appendix 1

Specification and changes of the **Irene radar** setup from September 2010 until the end of February 2020. Information was obtained directly from the metadata. Exact date of some of the changes is unknown due to missing data or changes occurring prior to the warm season.

Initial setup	**Values**			
Latitude	25.911816°S			
Longitude	28.210766°E			
height	1560 m AMSL			
Wavelength	10.452 cm			
Frequency	2.87 GHz			
Scan time	325 s			
Beamwidth	0.93°			
Elevation angles	**0.5, 1.3, 2.1, 3.1, 4.2, 5.5, 6.9, 8.5, 10.3, 12.4, 14.7, 17.4, 20.4, 23.8, 27.6, 32**			
Angle step	1°			
Antenna speed	24°/s			
range bin size	0.5 km			
Pulse width	1.67 µs			
Range averaging	1			
Time sampling	20			
Start & stop range	0 – 300 km			
Staggering ration	None			
Low and High PRF	500 Hz			
Nyquist Velocity	± 13.065 ms^{-1}			
21 October 2010	**Values**	**Values**	**Values**	**Values**
Scan time	355 s			
Elevation angles	**0.5, 1.3, 2.3, 3.4, 4.7**	**6.2**	**7.9, 9.9**	**12.2, 16.8, 17.8, 21.3, 30**
Angle step	1°	1°	1°	1°
Antenna speed	12°/s	18°/s	18°/s	24°/s
Range bin size	0.25 km	0.25 km	0.25 km	0.25 km
Pulse width	0.83 µs	0.83 µs	0.83 µs	0.83 µs
Range averaging	1	1	1	1
Time sampling	41	27	41	49
Start & stop range	0 – 300 km	0 – 300 km	0 – 200 km	0 – 120 km
Staggering ration	None	3/2	None	None
Low and High PRF	500 Hz	500 Hz	750 Hz	1200 Hz
Nyquist Velocity	± 13.065 ms^{-1}	± 13.065 ms^{-1}	± 19.5975 ms^{-1}	± 31.356 ms^{-1}

6 November 2010	Values	Values	Values	Values
Scan time	359 s			
Elevation angles	**0.5, 1.3, 2.3, 3.4, 4.7**	**6.2, 7.9, 9.9**	**12.2, 16.8**	**22, 30**
Angle step	0.8°	1°	1°	1°
Antenna speed	10°/s	18°/s	30°/s	24°/s
range bin size	0.5 km	0.5 km	0.5 km	0.5 km
Pulse width	1.67 µs	1.67 µs	1.67 µs	1.67 µs
Range averaging	2	2	2	2
Time sampling	34	33	39	49
Start & stop range	0 – 300km	0 – 200 km	0 – 120 km	0 – 120 km
Staggering ration	4/3	3/2	None	None
Low and High PRF	375 – 500 Hz	500 – 750 Hz	1200 Hz	1200 Hz
Nyquist Velocity	± 39.195 ms^{-1}	± 39.195 ms^{-1}	± 31.356 ms^{-1}	± 39.356 ms^{-1}

≈ September 2011	Values	Values	Values	Values	Values
Scan time	354 s				
Elevation angles	**0.5, 1.3, 2.3, 3.4, 4.7**	**6.2, 7.9**	**9.9**	**12.2, 16.8**	**22, 30**
Angle step	1°	1°	1°	1°	1°
Antenna speed	10°/s	18°/s	24°/s	24°/s	30°/s
range bin size	0.5 km	0.5 km	0.5 km	0.5 km	0.5 km
Pulse width	1.67 µs	1.67 µs	1.67 µs	1.67 µs	1.67 µs
Range averaging	2	4	4	4	4
Time sampling	44	36	27	44	35
Start & stop range	0 – 300km	0 – 200 km	0 – 120 km	0 – 120 km	0 – 120 km
Staggering ration	5/4	5/4	5/4	5/4	5/4
Low and High PRF	400 – 500 Hz	600 – 750 Hz	600 – 750 Hz	960 – 1200 Hz	960 – 1200 Hz
Nyquist Velocity	± 52.26 ms^{-1}	± 78.39 ms^{-1}	± 78.39 ms^{-1}	± 125.424 ms^{-1}	± 125.424 ms^{-1}

≈ 14 January 2013	Values	Values	Values	Values	Values
Scan time	357 s				
Elevation angles	**0.5, 1.3, 2.3, 3.4, 4.7, 6.2**	**7.9, 9.9**	**12.2**	**16.8**	**22, 30**
Angle step	1°	1°	1°	1°	1°
Antenna speed	10°/s	24°/s	28°/s	28°/s	32°/s
range bin size	0.5 km	0.5 km	0.5 km	0.5 km	0.5 km
Pulse width	1.67 µs	1.67 µs	1.67 µs	1.67 µs	1.67 µs
Range averaging	4	4	4	4	4
Time sampling	66	41	35	42	37
Start & stop range	0 – 200km	0 – 150 km	0 – 150 km	0 – 120 km	0 – 100 km
Staggering ration	5/4	None	None	None	None
Low and High PRF	600 – 750 Hz	1000 Hz	1000 Hz	1200 Hz	1200 Hz
Nyquist Velocity	± 78.39 ms^{-1}	± 26.13 ms^{-1}	± 26.13 ms^{-1}	± 31.356 ms^{-1}	± 31.356 ms^{-1}

≈ September 2013	Values	Values	Values	Values	Values	Values	Values	Values
Scan time	326 s							
Elevation angles	**0.5, 1.3, 2.3, 3.4, 4.7**	**6.2**	**7.9**	**9.9**	**12.2**	**16.8**	**22**	**30**
Angle step	1°	1°	1°	1°	1°	1°	1°	1°
Antenna speed	10°/s	24°/s	25°/s	32°/s	32°/s	34°/s	34°/s	34°/s
range bin size	0.5 km	0.5 km	0.5 km	0.5 km	0.5 km	0.5 km	0.5 km	0.5 km
Pulse width	1.67 µs	1.67 µs	1.67 µs	1.67 µs	1.67 µs	1.67 µs	1.67 µs	1.67 µs
Range averaging	1	1	1	1	1	1	1	1
Time sampling	66	35	39	37	37	35	35	35
Start & stop range	0 – 200km	0 – 175 km	0 – 150 km	0 – 125 km	0 – 100 km	0 – 75 km	0 – 60 km	0 – 50 km
Staggering ration	5/4	None	None	None	None	None	None	None
Low and High PRF	600 – 750 Hz	857 Hz	1000 Hz	1200 Hz	1200 Hz	1200 Hz	1200 Hz	1200 Hz
Nyquist Velocity	± 78.39 ms^{-1}	± 22.3934 ms^{-1}	± 26.4075 ms^{-1}	± 31.356 ms^{-1}	± 31.356 ms^{-1}	± 31.356 ms^{-1}	± 31.356 ms^{-1}	± 31.356 ms^{-1}

≈ 15 November 2013	Values	Values	Values	Values	Values	Values
Scan time	322 s					
Elevation angles	**0.5**	**1.3**	**2.3, 3.4, 4.7, 6.2**	**7.9, 9.9, 12.2**	**16.8**	**22, 30**
Angle step	1°	1°	1°	1°	1°	1°
Antenna speed	10°/s	11°/s	12°/s	28°/s	32°/s	32°/s
range bin size	0.5 km	0.5 km	0.5 km	0.5 km	0.5 km	0.5 km
Pulse width	1.67 µs	1.67 µs	1.67 µs	1.67 µs	1.67 µs	1.67 µs
Range averaging	4	4	4	4	4	4
Time sampling	59	54	49	35	37	37
Start & stop range	0 – 200 km	0 – 200 km	0 – 200 km	0 – 150 km	0 – 120 km	0 – 100 km
Staggering ration	3/2	3/2	3/2	None	None	None
Low and High PRF	500 – 750 Hz	500 – 750 Hz	500 – 750 Hz	1000 Hz	1200 Hz	1200 Hz
Nyquist Velocity	± 39.195 ms^{-1}	± 39.195 ms^{-1}	± 39.195 ms^{-1}	± 26.13 ms^{-1}	± 31.356 ms^{-1}	± 31.356 ms^{-1}

≈ 9 December 2014	Values	Values	Values	Values	Values
Scan time	326 s				
Elevation angles	**0.5, 1.3**	**2.3, 3.4, 4.7, 6.2**	**7.9, 9.9, 12.2**	**16.8**	**22, 30**
Angle step	1°	1°	1°	1°	1°
Antenna speed	10°/s	12°/s	28°/s	32°/s	32°/s
range bin size	0.5 km	0.5 km	0.5 km	0.5 km	0.5 km
Pulse width	1.67 µs	1.67 µs	1.67 µs	1.67 µs	1.67 µs
Range averaging	4	4	4	4	4
Time sampling	59	49	35	37	37
Start & stop range	0 – 200km	2 – 200km	0 – 150 km	1 – 120 km	0 – 100 km
Staggering ration	3/2	3/2	None	None	None
Low and High PRF	500 – 750 Hz	500 – 750 Hz	1000 Hz	1200 Hz	1200 Hz
Nyquist Velocity	± 40.035 ms^{-1}	± 40.035 ms^{-1}	± 26.69 ms^{-1}	± 32.028 ms^{-1}	± 32.028 ms^{-1}

≈ September 2017	Values	Values	Values	Values	Values
Scan time	326 s				
Elevation angles	**0.5, 1.3, 2.3**	**3.4, 4.7, 6.2**	**7.9, 9.9, 12.2**	**16.8**	**22, 30**
Angle step	1°	1°	1°	1°	1°
Antenna speed	10°/s	12°/s	28°/s	32°/s	32°/s
range bin size	0.5 km	0.5 km	0.5 km	0.5 km	0.5 km
Pulse width	1.67 µs	1.67 µs	1.67 µs	1.67 µs	1.67 µs
Range averaging	4	4	4	4	4
Time sampling	59	49	35	37	37
Start & stop range	0 – 200km	1 – 200km	0 – 150 km	0 – 120 km	0 – 100 km
Staggering ration	3/2	3/2	None	None	None
Low and High PRF	500 – 750 Hz	500 – 750 Hz	1000 Hz	1200 Hz	1200 Hz
Nyquist Velocity	± 39.6112 ms^{-1}	± 39.6112 ms^{-1}	± 26.4075 ms^{-1}	± 31.689 ms^{-1}	± 31.689 ms^{-1}
≈ September 2018	**Values**	**Values**	**Values**	**Values**	**Values**
Scan time	326 s				
Elevation angles	**0.5, 1.3**	**2.3, 3.4, 4.7, 6.2**	**7.9, 9.9, 12.2**	**16.8**	**22, 30**
Angle step	1°	1°	1°	1°	1°
Antenna speed	10°/s	12°/s	28°/s	32°/s	32°/s
range bin size	0.5 km	0.5 km	0.5 km	0.5 km	0.5 km
Pulse width	1.67 µs	1.67 µs	1.67 µs	1.67 µs	1.67 µs
Range averaging	4	4	4	4	4
Time sampling	31	25	36	38	38
Start & stop range	0 – 200km	1 – 200km	0 – 149 km	0 – 120 km	0 – 100 km
Staggering ration	3/2	3/2	None	None	None
Low and High PRF	500 – 750 Hz	500 – 750 Hz	1000 Hz	1200 Hz	1200 Hz
Nyquist Velocity	± 39.6112 ms^{-1}	± 39.6112 ms^{-1}	± 26.4075 ms^{-1}	± 31.689 ms^{-1}	± 31.689 ms^{-1}

Specification and changes of the **Ermelo radar** setup from September 2010 until the end of February 2020. Information was obtained directly from the metadata. Exact date of some of the changes is unknown due to missing data or changes occurring prior to the warm season.

Initial setup	**Values**			
Latitude	26.497955°S			
Longitude	29.984056°E			
height	1785 m AMSL			
Wavelength	10.563 cm			
Frequency	2.84 GHz			
Scan time	325 s			
Beamwidth	0.94°			
Elevation angles	**0.5, 1.3, 2.3, 3.3, 4.6, 5.9, 7.5, 9.2, 11.2, 13.5, 16.1, 19, 22.3, 26, 30.2, 35**			
Angle step	1°			
Antenna speed	24°/s			
range bin size	1 km			
Pulse width	3.33 µs			
Range averaging	2			
Time sampling	20			
Start & stop range	0 – 300 km			
Staggering ration	None			
Low and High PRF	500 Hz			
Nyquist Velocity	± 13.2037 ms^{-1}			
06-Nov-10	**Values**	**Values**	**Values**	**Values**
Scan time	359 s			
Elevation angles	**0.5, 1.3, 2.3, 3.4, 4.7**	**6.2, 7.9, 9.9**	**12.2, 16.8**	**22, 30**
Angle step	0.8°	1°	1°	1°
Antenna speed	10°/s	18°/s	30°/s	24°/s
range bin size	0.5 km	0.5 km	0.5 km	0.5 km
Pulse width	1.67 µs	1.67 µs	1.67 µs	1.67 µs
Range averaging	2	2	2	2
Time sampling	34	33	39	49
Start & stop range	0 – 300km	0 – 200 km	0 – 120 km	0 – 120 km
Staggering ration	4/3	3/2	None	None
Low and High PRF	375 – 500 Hz	500 – 750 Hz	1200 Hz	1200 Hz
Nyquist Velocity	± 39.6112 ms^{-1}	± 39.6112 ms^{-1}	± 31.689 ms^{-1}	± 31.689 ms^{-1}

10-Nov-10	**Values**	**Values**	**Values**
Scan time	353 s		
Elevation angles	**0.5, 1.3, 2.3, 3.4, 4.7**	**6.2, 7.9, 9.9**	**12.2, 16.8, 22, 30**
Angle step	1°	1°	1°
Antenna speed	10°/s	18°/s	30°/s
range bin size	0.5 km	0.5 km	0.5 km
Pulse width	1.67 µs	1.67 µs	1.67 µs
Range averaging	2	2	2
Time sampling	42	33	39
Start & stop range	0 - 300km	0 - 200 km	0 - 120 km
Staggering ration	4/3	3/2	None
Low and High PRF	375 - 500 Hz	500 - 750 Hz	1200 Hz
Nyquist Velocity	± 39.6112 ms^{-1}	± 39.6112 ms^{-1}	± 31.689 ms^{-1}

≈ October 2013	**Values**	**Values**	**Values**	**Values**	**Values**
Scan time	357 s				
Elevation angles	**0.5, 1.3, 2.3, 3.4, 4.7, 6.2**	**7.9, 9.9**	**12.2**	**16.8**	**22, 30**
Angle step	1°	1°	1°	1°	1°
Antenna speed	10°/s	24°/s	28°/s	28°/s	32°/s
range bin size	0.5 km	0.5 km	0.5 km	0.5 km	0.5 km
Pulse width	1.67 µs	1.67 µs	1.67 µs	1.67 µs	1.67 µs
Range averaging	2	2	2	2	2
Time sampling	65-66	41	35	42	36-37
Start & stop range	0 - 200km	0 - 150 km	0 - 150 km	0 - 120 km	0 - 100 km
Staggering ration	5/4	None	None	None	None
Low and High PRF	600 - 700 Hz	1000 Hz	1000 Hz	1200 Hz	1200 Hz
Nyquist Velocity	± 37.5 ms^{-1}	± 12.5 ms^{-1}	± 12.5 ms^{-1}	± 15 ms^{-1}	± 15 ms^{-1}
≈ 15 November 2013	**Values**	**Values**	**Values**	**Values**	**Values**
Scan time	356 s				
Elevation angles	**0.5, 1.3, 2.3, 3.4, 4.7, 6.2**	**7.9, 9.9**	**12.2**	**16.8**	**22, 30**
Angle step	1°	1°	1°	1°	1°
Antenna speed	10°/s	24°/s	28°/s	32°/s	32°/s
range bin size	0.5 km	0.5 km	0.5 km	0.5 km	0.5 km
Pulse width	1.67 µs	1.67 µs	1.67 µs	1.67 µs	1.67 µs
Range averaging	4	4	4	4	4
Time sampling	58-59	40-41	35	37	36-37
Start & stop range	0 - 200km	0 - 150 km	0 - 150 km	0 - 120 km	0 - 100 km
Staggering ration	3/2	None	None	None	None
Low and High PRF	500 - 750 Hz	1000 Hz	1000 Hz	1200 Hz	1200 Hz
Nyquist Velocity	± 18.75 ms^{-1}	± 12.5 ms^{-1}	± 12.5 ms^{-1}	± 15 ms^{-1}	± 15 ms^{-1}

≈ September 2015	Values	Values	Values	Values	Values
Wavelength	10 cm				
Frequency	3.0 GHz				
Scan time	326 s				
Beamwidth	1°				
Elevation angles	**0.5, 1.3**	**2.3, 3.4, 4.7, 6.2**	**7.9, 9.9, 12.2**	**16.8**	**22, 30**
Angle step	1°	1°	1°	1°	1°
Antenna speed	10°/s	12°/s	28°/s	32°/s	32°/s
range bin size	0.5 km	0.5 km	0.5 km	0.5 km	0.5 km
Pulse width	1.67 µs	1.67 µs	1.67 µs	1.67 µs	1.67 µs
Range averaging	1	1	1	1	1
Time sampling	59	49	35	37	37
Start & stop range	0 - 200km	0 - 200km	0 - 150 km	0 - 120 km	0 - 100 km
Staggering ration	3/2	3/2	None	None	None
Low and High PRF	500 - 750 Hz	500 - 750 Hz	1000 Hz	1200 Hz	1200 Hz
Nyquist Velocity	± 18.75 ms^{-1}	± 18.75 ms^{-1}	± 12.5 ms^{-1}	± 15 ms^{-1}	± 15 ms^{-1}
≈ September 2019	**Values**	**Values**	**Values**	**Values**	**Values**
Wavelength	10.601 cm				
Frequency	2.82 GHz				
Scan time	326 s				
Beamwidth	0.93°				
Elevation angles	**0.5, 1.3**	**2.3, 3.4, 4.7, 6.2**	**7.9, 9.9, 12.2**	**16.8**	**22, 30**
Angle step	1°	1°	1°	1°	1°
Antenna speed	10°/s	12°/s	28°/s	32°/s	32°/s
range bin size	0.5 km	0.5 km	0.5 km	0.5 km	0.5 km
Pulse width	1.67 µs	1.67 µs	1.67 µs	1.67 µs	1.67 µs
Range averaging	1	1	1	1	1
Time sampling	31	25	35	38	37
Start & stop range	0 - 200km	0 - 200km	0 - 149 km	0 - 120 km	0 - 100 km
Staggering ration	3/2	3/2	None	None	None
Low and High PRF	500 - 750 Hz	500 - 750 Hz	1000 Hz	1200 Hz	1200 Hz
Nyquist Velocity	± 18.75 ms^{-1}	± 18.75 ms^{-1}	± 12.5 ms^{-1}	± 15 ms^{-1}	± 15 ms^{-1}

Appendix 2

The supercell database of all supercells identified during the warm seasons (September to February) of 2010-2011 until 2019-2020 (seasons have been colour coded). Due to missing data not 2011-2012 season is available.

Name	Date	Left-mover (LM) or right-mover (RM)	Start time (UTC)	End time (UTC)	start and end available	Total duration	Life Span	Radar used to analyse supercell	Distance in km (calculated from QGIS)	Speed in km/h (calculated from distance/ duration)	Start location Latitude	Start location Longitude	End location Latitude	End location Longitude
SC14101001	14-Oct-10	LM	22:01:27	22:39:22	Yes	00:37:55	short-lived	FAEO	52.982	83.84	-26.8683	29.8583	-27.0156	30.3632
SC24101001	24-Oct-10	LM	11:59:18	13:53:16	Yes	01:53:58	short-lived	FAIR	92.069	48.47	-25.3332	28.5783	-24.9836	29.3916
SC24101002	24-Oct-10	LM	12:41:16	14:05:17	Yes	01:24:01	short-lived	FAIR	81.005	57.85	-25.8346	28.0526	-25.9349	28.8449
SC28101001	28-Oct-10	LM	02:59:17	03:53:17	Yes	00:54:00	short-lived	FAIR	56.179	62.42	-25.1588	28.3112	-25.1781	28.8636
SC05111001	05-Nov-10	LM	11:02:44	12:02:18	Yes	00:59:34	short-lived	FAEO	64.074	64.54	-26.5582	29.7123	-26.4622	30.3374
SC05111002	05-Nov-10	LM	11:47:15	12:29:16	Yes	00:42:01	short-lived	FAIR	25.454	36.35	-26.3736	27.9543	-26.3960	28.2030
SC05111003	05-Nov-10	LM	12:11:15	12:47:23	Yes	00:36:08	short-lived	FAIR	33.863	56.23	-26.2682	27.9493	-26.3190	28.2790
SC05111004	05-Nov-10	LM	12:13:06	13:01:52	Yes	00:48:46	short-lived	FAEO	42.863	52.74	-26.2691	29.5202	-26.1402	29.9084
SC05111005	05-Nov-10	LM	12:59:23	14:35:22	Yes	01:35:59	short-lived	FAIR	113.32	70.84	-26.8610	27.3250	-26.7377	28.4387
SC05111006	05-Nov-10	LM	15:11:23	15:59:25	Yes	00:48:02	short-lived	FAIR	44.587	55.70	-26.4288	28.4095	-26.3210	28.8374
SC07121001	07-Dec-10	LM	15:53:19	17:17:20	Yes	01:24:01	short-lived	FAEO	47.739	34.09	-26.9143	29.8896	-26.5480	30.0788
SC14121001	14-Dec-10	LM	14:04:55	16:15:55	Yes	02:11:00	moderate-lived	FAEO	38.616	17.69	-26.9335	29.9352	-26.6055	29.9208
SC02101101	02-Oct-11	LM	14:29:18	15:35:19	Yes	01:06:01	short-lived	FAIR	60.761	55.22	-25.5782	27.4830	-25.5871	28.0866
SC02101102	02-Oct-11	LM	14:41:15	16:17:19	Yes	01:36:04	short-lived	FAIR	74.248	46.37	-26.3705	27.6933	-26.4467	28.4225
SC02101103	02-Oct-11	LM	16:29:20	17:41:15	Yes	01:11:55	short-lived	FAIR	69.173	57.71	-25.7359	27.9711	-25.6573	28.6510
SC19101101	19-Oct-11	LM	11:05:16	12:11:18	Yes	01:06:02	short-lived	FAIR	68.179	61.95	-25.8631	28.5909	-26.0358	29.2366
SC19101102	19-Oct-11	RM	14:11:18	14:47:19	Yes	00:36:01	short-lived	FAIR	56.178	93.59	-25.6971	27.3308	-26.0923	27.6677

Name	Date	Left-mover (LM) or right-mover (RM)	Start time (UTC)	End time (UTC)	start and end available	Total duration	Life Span	Radar used to analyse supercell	Distance in km (calculated from QGIS)	Speed in km/h (calculated from distance/ duration)	Start location Latitude	Start location Longitude	End location Latitude	End location Longitude
SC19101103	19-Oct-11	RM	14:23:20	14:59:20	Yes	00:36:00	short-lived	FAIR	58.784	97.97	-25.9437	27.7037	-26.3197	28.1091
SC22111101	22-Nov-11	LM	13:11:19	13:47:20	Yes	00:36:01	short-lived	FAIR	12.606	21.00	-26.3698	28.4898	-26.3381	28.6097
SC22111102	22-Nov-11	LM	14:29:19	15:11:17	Yes	00:41:58	short-lived	FAIR	15.719	22.47	-26.3385	28.3813	-26.2785	28.5039
SC22111103	22-Nov-11	LM	14:53:19	16:17:17	Yes	01:23:58	short-lived	FAIR	33.305	23.80	-25.5210	27.3898	-25.3511	27.6278
SC19101301	19-Oct-13	LM	11:59:55	12:29:56	Yes	00:30:01	short-lived	FAIR	19.263	38.50	-27.0887	28.4538	-27.0107	28.6256
SC19101302	19-Oct-13	LM	12:29:56	13:47:55	Yes	01:17:59	short-lived	FAIR	58.183	44.77	-26.9127	28.9233	-26.5424	29.3185
SC19101303	19-Oct-13	LM	13:41:54	15:05:54	Yes	01:24:00	short-lived	FAIR	68.168	48.69	-26.1480	28.2473	-25.7540	28.7403
SC30101301	30-Oct-13	LM	15:11:53	17:29:54	End unknown[1]	02:18:01*	moderate-lived	FAIR	98.281*	42.73*	-26.7438	28.4581	-26.3460	29.2933
SC11111301	11-Nov-13	LM	15:29:52	16:29:53	Yes	01:00:01	short-lived	FAIR	23.812	23.81	-25.8237	28.9105	-25.6317	28.8227
SC11111302	11-Nov-13	LM	15:47:51	17:35:52	Yes	01:48:01	short-lived	FAIR	59.319	32.95	-26.2937	28.2577	-25.7836	28.4068
SC27111301	27-Nov-13	LM	15:05:27	16:47:34	Both unknown[2]	01:42:07*	short-lived	FAEO	54.611*	32.09*	-27.0335	29.7101	-26.5752	29.8947
SC28111301	28-Nov-13	LM	11:28:53	12:16:53	Yes	00:48:00	short-lived	FAIR	28.481	35.60	-26.8159	27.9216	-26.6488	28.1272
SC28111301.2	28-Nov-13	LM	12:52:53	13:52:53	Yes	01:00:00	short-lived	FAIR	42.899	42.90	-26.4550	28.1663	-26.1353	28.3601
SC28111302	28-Nov-13	LM	12:10:52	13:22:52	Yes	01:12:00	short-lived	FAIR	58.551	48.79	-26.6546	27.4525	-26.2500	27.8077
SC28111303	28-Nov-13	LM	13:28:52	14:04:53	Yes	00:36:01	short-lived	FAIR	28.497	47.47	-26.4033	27.5847	-26.1970	27.7472
SC28111304	28-Nov-13	LM	13:40:52	16:28:55	Yes	02:48:03	moderate-lived	FAIR	144.698	51.66	-26.1796	27.7879	-25.0450	28.3670
SC28111305	28-Nov-13	LM	14:40:52	15:10:53	Yes	00:30:01	short-lived	FAIR	20.615	41.21	-25.7423	28.3959	-25.6251	28.5525
SC28111306	28-Nov-13	LM	16:58:56	17:34:49	Yes	00:35:53	short-lived	FAIR	30.608	51.18	-26.4216	27.5140	-26.2154	27.7114
SC18121301	18-Dec-13	LM	13:17:23	14:17:24	Yes	01:00:01	short-lived	FAEO	34.683	34.67	-26.5510	29.4083	-26.2875	29.5939
SC11011401	11-Jan-14	LM	13:29:22	14:35:23	Yes	01:06:01	short-lived	FAEO	20.566	18.69	-26.6298	30.2618	-26.4728	30.3009
SC13011401	13-Jan-14	LM	12:23:22	13:17:23	Yes	00:54:01	short-lived	FAEO	46.895	52.09	-27.0345	30.3677	-26.6386	30.5152
SC13011402	13-Jan-14	LM	14:11:23	14:47:21	Yes	00:35:58	short-lived	FAEO	26.022	43.41	-26.2589	30.5620	-26.0520	30.6428
SC26021401	26-Feb-14	LM	13:46:49	14:28:50	Yes	00:42:01	short-lived	FAIR	21.449	30.63	-26.0882	28.0499	-25.9149	28.1036

Name	Date	Left-mover (LM) or right-mover (RM)	Start time (UTC)	End time (UTC)	start and end available	Total duration	Life Span	Radar used to analyse supercell	Distance in km (calculated from QGIS)	Speed in km/h (calculated from distance/ duration)	Start location Latitude	Start location Longitude	End location Latitude	End location Longitude
SC20091401	20-Sep-14	RM	15:58:55	17:34:54	Yes	01:35:59	short-lived	FAIR	74.313	46.45	-25.8453	27.6388	-26.2089	28.2226
SC20091402	20-Sep-14	LM	17:16:53	19:16:50	Yes	01:59:57	short-lived	FAIR	37.258	18.64	-26.3877	27.4230	-26.1159	27.6009
SC29091401	29-Sep-14	LM	20:52:50	22:58:49	Yes	02:05:59	moderate-lived	FAIR	139.074	66.23	-26.1090	27.4418	-26.3290	28.7971
SC29091401.2	29-Sep-14	LM	23:28:50	23:58:49	Yes	00:29:59	short-lived	FAIR	35.557	71.15	-26.3770	29.1268	-26.4167	29.4795
SC10101401	10-Oct-14	LM	14:10:50	14:46:49	Yes	00:35:59	short-lived	FAIR	20.666	34.46	-25.8615	27.4593	-25.8601	27.6625
SC01111401	01-Nov-14	LM	16:04:49	18:22:50	Yes	02:18:01	moderate-lived	FAIR	90.423	39.31	-26.9110	27.8403	-26.7280	28.7105
SC24111401	24-Nov-14	LM	15:16:53	16:28:53	Yes	01:12:00	short-lived	FAIR	65.962	54.97	-26.2488	26.8836	-25.7790	27.2613
SC16101501	16-Oct-15	LM	11:38:55	12:50:56	Yes	01:12:01	short-lived	FAIR	42.824	35.68	-25.1447	28.5599	-24.9248	28.8886
SC23101501	23-Oct-15	LM	15:34:53	16:34:53	Yes	01:00:00	short-lived	FAEO	26.878	26.88	-26.5693	30.2012	-26.3439	30.1417
SC24101501	24-Oct-15	LM	12:22:55	13:52:51	Yes	01:29:56	short-lived	FAEO	53.25	35.53	-27.0787	30.3747	-26.6321	30.5367
SC24101502	24-Oct-15	LM	13:04:51	13:46:52	Yes	00:42:01	short-lived	FAEO	14.151	20.21	-26.3694	30.5595	-26.2524	30.5900
SC24101503	24-Oct-15	LM	14:46:53	16:40:53	Yes	01:54:00	short-lived	FAEO	51.321	27.01	-26.2038	30.1512	-25.7759	30.2336
SC16111501	16-Nov-15	LM	09:58:55	11:04:53	Yes	01:05:58	short-lived	FAIR	33.429	30.41	-25.9700	28.9620	-25.8729	29.2609
SC16111502	16-Nov-15	LM	10:46:53	11:16:55	Yes	00:30:02	short-lived	FAIR	10.87	21.72	-25.5409	28.1100	-25.4674	28.1718
SC16111502.2	16-Nov-15	LM	11:58:55	13:10:55	Yes	01:12:00	short-lived	FAIR	38.02	31.68	-25.3565	28.2235	-25.0912	28.4571
SC16111503	16-Nov-15	LM	11:58:55	14:58:55	Yes	03:00:00	moderate-lived	FAIR	115.359	38.45	-26.6189	28.1064	-25.8504	28.8403
SC16111504	16-Nov-15	LM	12:34:56	14:28:54	Yes	01:53:58	short-lived	FAIR	70.81	37.28	-25.6092	27.6401	-25.0988	28.0433
SC16111505	16-Nov-15	LM	13:28:55	14:22:56	Yes	00:54:01	short-lived	FAIR	23.76	26.39	-26.2669	27.9451	-26.1855	28.1515
SC09011601	09-Jan-16	LM	13:22:54	15:28:53	Yes	02:05:59	moderate-lived	FAIR	62.152	29.60	-26.2578	27.7618	-25.7294	27.8961
SC04021601	04-Feb-16	LM	12:40:51	13:40:52	Yes	01:00:01	short-lived	FAEO	48.407	48.39	-27.1629	29.5530	-26.8181	29.8488
SC04021602	04-Feb-16	LM	15:46:52	16:22:53	Start unknown[3]	00:36:01*	short-lived	FAEO	31.703*	52.81*	-26.7534	29.4387	-26.5090	29.6020
SC04021603	04-Feb-16	LM	15:46:52	17:04:53	Start unknown[4]	01:12:00*	short-lived	FAEO	62.061*	51.72*	-26.0705	29.6657	-25.5733	29.9381
SC21021601	21-Feb-16	LM	12:58:53	14:04:53	Yes	01:06:00	short-lived	FAEO	52.705	47.91	-27.0884	29.8956	-26.8099	30.3129

Name	Date	Left-mover (LM) or right-mover (RM)	Start time (UTC)	End time (UTC)	start and end available	Total duration	Life Span	Radar used to analyse supercell	Distance in km (calculated from QGIS)	Speed in km/h (calculated from distance/ duration)	Start location Latitude	Start location Longitude	End location Latitude	End location Longitude
SC13091601	13-Sep-16	LM	13:34:54	14:10:55	Yes	00:36:01	short-lived	FAEO	23.793	39.64	-26.9998	29.3715	-26.9115	29.5667
SC30091601	30-Sep-16	LM	14:04:50	15:16:49	Yes	01:11:59	short-lived	FAEO	57.716	48.11	-26.9706	30.8610	-26.6618	31.3080
SC26101601	26-Oct-16	LM	13:46:56	14:52:55	Yes	01:05:59	short-lived	FAEO	40.399	36.74	-25.9003	30.1286	-25.5424	30.1193
SC26101602	26-Oct-16	RM	16:04:56	16:58:49	Yes	00:53:53	short-lived	FAEO	34.96	38.93	-26.6918	29.9308	-26.7447	30.2626
SC26101603	26-Oct-16	LM	16:46:50	17:46:50	Yes	01:00:00	short-lived	FAEO	28.317	28.32	-26.4782	29.8156	-26.2261	29.8436
SC10111601	10-Nov-16	LM	12:34:55	14:04:54	Yes	01:29:59	short-lived	FAEO	34.107	22.74	-26.2574	30.4400	-25.9647	30.5249
SC10111602	10-Nov-16	LM	13:22:53	14:34:54	Yes	01:12:01	short-lived	FAIR	45.686	38.06	-26.7077	27.4043	-26.4116	27.7109
SC15111601	15-Nov-16	LM	14:28:56	15:04:55	Yes	00:35:59	short-lived	FAIR	10.825	18.05	-26.6022	28.3935	-26.5352	28.3166
SC17111601	17-Nov-16	LM	16:04:57	17:22:51	Yes	01:17:54	short-lived	FAIR	49.112	37.83	-26.0570	28.9042	-25.6602	29.1181
SC20111601	20-Nov-16	LM	15:52:53	17:22:55	Yes	01:30:02	short-lived	FAIR	51.158	34.09	-26.1949	27.6658	-25.7558	27.7625
SC09101701	09-Oct-17	LM	13:04:53	13:34:52	Yes	00:29:59	short-lived	FAIR	39	78.04	-26.1023	27.4401	-26.1539	27.8231
SC09111701	09-Nov-17	LM	18:04:49	19:40:50	Yes	01:36:01	short-lived	FAEO	71.613	44.75	-26.9042	29.1662	-26.5564	29.7554
SC11121701	11-Dec-17	LM	14:40:54	16:28:54	Yes	01:48:00	short-lived	FAIR	88.126	48.96	-27.0296	27.9642	-26.6418	28.7226
SC18121701	18-Dec-17	LM	15:46:51	16:34:51	Yes	00:48:00	short-lived	FAEO	28.817	36.02	-27.2335	30.6839	-27.0920	30.9186
SC18121702	18-Dec-17	LM	16:10:50	17:34:52	Yes	01:24:02	short-lived	FAEO	36.011	25.71	-27.1352	30.4156	-26.9561	30.6927
SC24121701	24-Dec-17	LM	17:04:57	17:40:58	Yes	00:36:01	short-lived	FAIR	16.409	27.34	-26.2428	28.3112	-26.1415	28.4278
SC24121701.2	24-Dec-17	LM	17:52:57	18:58:51	Yes	01:05:54	short-lived	FAIR	28.677	26.11	-26.0610	28.4285	-25.8213	28.5240
SC29121701	29-Dec-17	LM	13:10:48	14:34:49	Yes	01:24:01	short-lived	FAEO	35.333	25.23	-26.7716	30.3954	-26.4937	30.5493
SC30121701	30-Dec-17	LM	14:28:55	15:10:55	Yes	00:42:00	short-lived	FAIR	33.71	48.16	-26.3834	27.7500	-26.1485	27.9633
SC30121702	30-Dec-17	LM	16:40:55	17:16:55	Yes	00:36:00	short-lived	FAIR	41.587	69.31	-26.0409	28.1105	-25.8185	28.4326
SC30121703	30-Dec-17	LM	17:04:56	17:40:55	Yes	00:35:59	short-lived	FAIR	27.642	46.09	-25.5676	28.4802	-25.3821	28.6531
SC25011801	25-Jan-18	LM	17:28:51	18:04:52	Yes	00:36:01	short-lived	FAEO	17.234	28.71	-26.8817	29.9159	-26.7332	29.8821
SC13101801	13-Oct-18	LM	09:04:56	09:52:50	Yes	00:47:54	short-lived	FAIR	25.989	32.55	-26.6836	27.6571	-26.6233	27.8995
SC13101802	13-Oct-18	LM	12:40:52	14:22:52	Yes	01:42:00	short-lived	FAIR	60.367	35.51	-25.9307	27.5622	-25.7681	28.1237

Name	Date	Left-mover (LM) or right-mover (RM)	Start time (UTC)	End time (UTC)	start and end available	Total duration	Life Span	Radar used to analyse supercell	Distance in km (calculated from QGIS)	Speed in km/h (calculated from distance/ duration)	Start location Latitude	Start location Longitude	End location Latitude	End location Longitude
SC31101801	31-Oct-18	LM	11:28:51	12:40:50	Yes	01:11:59	short-lived	FAIR	39.564	32.98	-25.2789	28.7473	-25.2711	29.1340
SC01111801	01-Nov-18	LM	11:16:50	12:22:55	Yes	01:06:05	short-lived	FAIR	54.663	49.63	-25.5883	27.6955	-25.5637	28.2378
SC01111801.2	01-Nov-18	LM	12:40:49	13:46:51	Yes	01:06:02	short-lived	FAIR	50.359	45.76	-25.5681	28.3668	-25.4915	28.8575
SC01111802	01-Nov-18	LM	12:22:55	14:52:52	Yes	02:29:57	moderate-lived	FAIR	172.899	69.18	-25.3964	27.5157	-24.8424	29.1096
SC24111801	24-Nov-18	LM	11:58:46	12:28:59	Yes	00:30:13	short-lived	FAEO	18.109	35.96	-27.3252	30.9492	-27.1969	31.0550
SC24111802	24-Nov-18	LM	16:58:50	17:40:50	Yes	00:42:00	short-lived	FAEO	16.331	23.33	-26.3549	30.2907	-26.2121	30.2629
SC04121801	04-Dec-18	LM	13:28:51	14:34:50	Yes	01:05:59	short-lived	FAEO	35.006	31.83	-26.4320	31.0209	-26.1883	31.2334
SC13121801	13-Dec-18	LM	13:22:53	14:40:55	Yes	01:18:02	short-lived	FAEO	42.936	33.01	-27.1123	29.9075	-26.8195	30.1801
SC14121801	14-Dec-18	LM	14:28:54	15:04:54	Yes	00:36:00	short-lived	FAEO	16.432	27.39	-26.7309	29.8954	-26.6117	29.9252
SC20121801	20-Dec-18	LM	10:46:49	12:52:52	Yes	02:06:03	moderate-lived	FAEO	59.482	28.31	-26.4179	29.6286	-26.0196	30.0037
SC20121802	20-Dec-18	LM	10:52:49	13:16:53	Yes	02:24:04	moderate-lived	FAEO	86.144	35.88	-26.8830	29.3237	-26.2556	29.7792
SC20121803	20-Dec-18	LM	12:22:53	14:34:53	Yes	02:12:00	moderate-lived	FAEO	76.636	34.83	-25.8957	30.0339	-25.2888	30.3548
SC22121801	22-Dec-18	LM	16:16:53	17:28:53	Yes	01:12:00	short-lived	FAEO	66.915	55.76	-27.3992	30.5797	-26.8252	30.4880
SC24121801	24-Dec-18	LM	14:16:52	15:04:50	Yes	00:47:58	short-lived	FAEO	31.913	39.92	-27.0119	30.4595	-26.7534	30.5034
SC19011901	19-Jan-19	LM	14:16:55	16:22:56	Yes	02:06:01	moderate-lived	FAIR	102.469	48.79	-26.5489	28.9654	-25.6848	29.1820
SC24011901	24-Jan-19	LM	15:52:54	18:40:46	Yes	02:47:52	moderate-lived	FAEO	113.59	40.60	-27.5921	29.3578	-26.6192	29.5193
SC01101901	01-Oct-19	LM	17:34:51	19:16:52	Yes	01:42:01	short-lived	FAIR	43.006	25.29	-25.4999	28.1066	-25.1604	28.2956
SC01101902	01-Oct-19	LM	17:34:51	18:40:52	Yes	01:06:01	short-lived	FAIR	22.092	20.08	-25.4656	27.8984	-25.2886	27.9670
SC22101901	22-Oct-19	LM	12:40:46	13:40:47	Yes	01:00:01	short-lived	FAEO	60.275	60.26	-26.7570	29.3359	-26.5313	29.8504
SC26101901	26-Oct-19	LM	11:58:55	12:58:54	Yes	00:59:59	short-lived	FAEO	60.691	60.71	-27.1889	29.5330	-27.0387	30.1135
SC26101902	26-Oct-19	LM	13:58:57	16:16:47	Yes	02:17:50	moderate-lived	FAEO	130.508	56.81	-26.7721	29.6670	-26.1638	30.7670
SC09111901	09-Nov-19	RM	13:22:52	13:58:51	Yes	00:35:59	short-lived	FAEO	33.186	55.34	-27.2649	29.9682	-27.3108	30.2969
SC09111902	09-Nov-19	LM	13:16:52	14:28:52	Yes	01:12:00	short-lived	FAEO	36.197	30.16	-26.7831	30.0837	-26.5119	30.2597
SC09111903	09-Nov-19	LM	17:58:56	18:52:50	Yes	00:53:54	short-lived	FAIR	34.088	37.95	-25.9886	28.2199	-25.8929	28.5348

Name	Date	Left-mover (LM) or right-mover (RM)	Start time (UTC)	End time (UTC)	start and end available	Total duration	Life Span	Radar used to analyse supercell	Distance in km (calculated from QGIS)	Speed in km/h (calculated from distance/ duration)	Start location Latitude	Start location Longitude	End location Latitude	End location Longitude
SC10111901	10-Nov-19	LM	19:10:53	20:34:54	Yes	01:24:01	short-lived	FAEO	71.24	50.88	-27.3349	29.8498	-26.9426	30.4106
SC18111901	18-Nov-19	LM	09:52:59	10:22:48	Yes	00:29:49	short-lived	FAEO	23.827	47.95	-26.9224	29.7399	-26.8735	29.9726
SC18111902	18-Nov-19	LM	10:22:48	11:16:48	Yes	00:54:00	short-lived	FAEO	46.594	51.77	-26.5914	29.9102	-26.4456	30.3338
SC03121901	03-Dec-19	LM	19:53:01	20:58:52	Yes	01:05:51	short-lived	FAEO	32.249	29.38	-26.3532	29.8123	-26.3075	30.1202
SC31121901	31-Dec-19	RM	11:58:47	12:34:59	Yes	00:36:12	short-lived	FAEO	21.724	36.01	-26.2194	29.5848	-26.3072	29.7756
SC31121902	31-Dec-19	LM	12:28:59	13:16:59	Yes	00:48:00	short-lived	FAEO	36.98	46.22	-27.0487	29.8015	-26.7523	29.9687
SC31121903	31-Dec-19	LM	14:47:00	16:29:01	Yes	01:42:01	short-lived	FAEO	54.541	32.08	-26.3460	30.1217	-25.8679	30.1085
SC03012001	03-Jan-20	LM	15:40:48	16:34:50	Yes	00:54:02	short-lived	FAEO	25.145	27.92	-27.0356	30.4616	-26.8148	30.4607
SC21012001	21-Jan-20	LM	13:52:43	14:34:55	Yes	00:42:12	short-lived	FAEO	22.324	31.74	-26.8861	30.1385	-26.6923	30.1531
SC21012002	21-Jan-20	LM	14:22:43	15:28:44	Yes	01:06:01	short-lived	FAEO	37.457	34.04	-26.6194	30.1858	-26.3002	30.2522

[1] Data not available for the remainder of the day

[2] Start time - 66 minutes since last available scan, end time - 18 minutes until the next scan

[3] Start time – 18 minutes since last available scan

[4] Start time – 18 minutes since last available scan

* Data may be inaccurate due to unknown start and/or end time/location. This value is based on the last known initiation and/or demise time/location. This information was not included in various statistics presented in this dissertation.